Micromechanics of Deformation and Abrasive Wear of Fiber-Filled Elastomers

by

Ethan M. Parsons

Submitted to the Department of Mechanical Engineering
in partial fulfillment of the requirements for the degree of

Master of Science in Mechanical Engineering

at the

MASSACHUSETTS INSTITUTE OF TECHNOLOGY

February 2000

Author .....
Department of Mechanical Engineering
January 13, 2000

Certified by .....
Mary C. Boyce
Professor of Mechanical Engineering
Thesis Supervisor

Accepted by .....
Ain A. Sonin
Chairman, Department Committee on Graduate Students

Micromechanics of Deformation and Abrasive Wear of Fiber-Filled Elastomers

by

Ethan M. Parsons

Submitted to the Department of Mechanical Engineering
on January 13, 2000, in partial fulfillment of the
requirements for the degree of
Master of Science in Mechanical Engineering

Abstract

The abrasive wear of unfilled and fiber-filled elastomers was studied both with experiments and with finite element simulations. Wear experiments with elastomer seals exhibited two distinct regimes: an initial, "break-in" period followed by an "aggressive wear" period. During the break-in period, few abrasive particles are able to penetrate the seal's contact band, and no substantial seal wear occurs. During the aggressive wear period, abrasive particles aggregate into distinct clusters which advance at a linear rate and abrasively wear the seal. Filled elastomer seals were shown to have break-in periods significantly longer than those of unfilled elastomer seals. The aggressive wear rates and mechanisms of filled and unfilled elastomer seals were determined to be virtually identical. Abrasion patterns typical of the abrasive wear of elastomers were observed. Micromechanical modeling of the abrasive wear of unfilled elastomers predicted the formation of the observed abrasion patterns. Modeling of fiber-filled elastomers indicated that fibers should have no effect on the aggressive wear process. Additional modeling of fiber-filled elastomers suggested several mechanisms by which the fibers might extend the break-in period of the seal. Seal wear experiments with well-defined slurries offered strong evidence that the fibers extend the break-in period of the seal by inhibiting particle ingestion and cluster formation. A seal lip surface geometry is proposed to simulate the effect of the fibers.

Thesis Supervisor: Mary C. Boyce
Title: Professor of Mechanical Engineering

Acknowledgments

First of all, I would like to thank Professor Boyce not only for all her advice and support but also for just plain putting up with me. I don't know how she does it. In her honor, I promise not to wear my hat in class in the future – well, at least not every day. I reserve the right to withdraw this pledge if the Sox win the Series this year.

I would like to acknowledge Caterpillar's generous contributions to this project. CAT freely and promptly provided data, material, equipment, and knowledge gained from countless years of experience. I would particularly like to thank Teresa Cushing, Kristy Johnson, Anthony Friend, Alan Dickey, Jerry Metz, and Tom White. I would also like to thank Professor Hart not only for making this project possible but also for lifting my spirits and boosting my ego every now and then.

I owe a humongous thank you to Hugo. Much of the data presented in this thesis could not have been obtained without his experimental and computational wizardry.

There is a long list of people whose contributions in one way or another have made it possible for me to complete this thesis: Rachel for being there for me in so many ways, Joanne for dinner, Brett for not making me drink his homebrew, Jenn for getting me here, Jess for the rides, Gabe for not telling everyone I still haven't gotten Megan and him a wedding present, Shakey for the hoops, Chi-town for the subs, Gu for late night philosophizing and occasionally valuable computational advice, Carlos for late night experimental help, Kid Rock for reminding me it's all good and it's all in fun, Nomar and Pedro for giving me a reason to come in every night this summer, NCC and MIT Cycling for giving me a reason to leave every night this summer, Jorge and Craig for sticking around, Dan for leaving, Mike for making my previous stint bearable, and Clarence, Patricia, Yioula, Jorgen, Mike, Prakash, Brian, Tom, Kevin, Harish, Steve, Jeremy, Rami, Mats, Una, and Ray for many things.

I would like to thank my parents for their support and encouragement. Thanks for giving me somewhere that I'm proud to be from and always able to go home to.

Finally, in case she ever asks, I need to thank my sister, Kate.

Contents

List of Figures

List of Tables

Chapter 1

Introduction

Filler particles have been added to elastomers to improve the materials' mechanical properties for many years. Historically, reinforcing ingredients such as carbon black, silica, and clay were used to increase tensile strength, modulus, and hardness [2]. In the past 20 years, the use of short fibers has increased considerably. Elastomers reinforced with short fibers have a combination of good strength and stiffness from the fibers and excellent flexibility and elasticity from the matrix. They are commonly used in applications such as V-belts, hoses, and seals [1]. The effect of fillers on the abrasive wear of elastomers, however, is not fully understood.

1.1 Filled Elastomers

An elastomer is a class of polymer that exhibits rubber-like elasticity. It has the ability to elastically deform by enormous amounts without permanently changing shape and may therefore be referred to casually as a "rubber." Filled elastomers are formed by incorporating solid particles into a liquid polymer phase which, upon curing, transforms into a solid matrix.

1.1.1 Effect of Fillers on Mechanical Properties

The addition of fillers to a rubber or elastomer can drastically change the material's mechanical properties. The modulus and strength properties of the composite depend on the extent to which the applied load is transferred to the fibers [1].

Geethamma et al [1] conducted experiments on natural rubber (NR) reinforced with coir, a hard lignocellulosic fiber, at a volume fraction of 24%. The coir had an average diameter of 100-400 μm and was chopped into 6, 10, and 14 mm lengths. Geethamma et al discovered that the fibers preferentially aligned in the direction of mold flow and that all properties were maximized in this, the longitudinal, direction. They found that the extent of load transference was a function of the fiber length and the degree of adhesion between the fiber and the matrix. Figure 1-1 (a) shows that the moduli of all the composites were at least 200% greater than that of the gum rubber. The composite with the 10 mm fibers had the highest modulus of the

Figure 1-1: Effect of Coir Fibers on the Mechanical Properties of Natural Rubber [1]

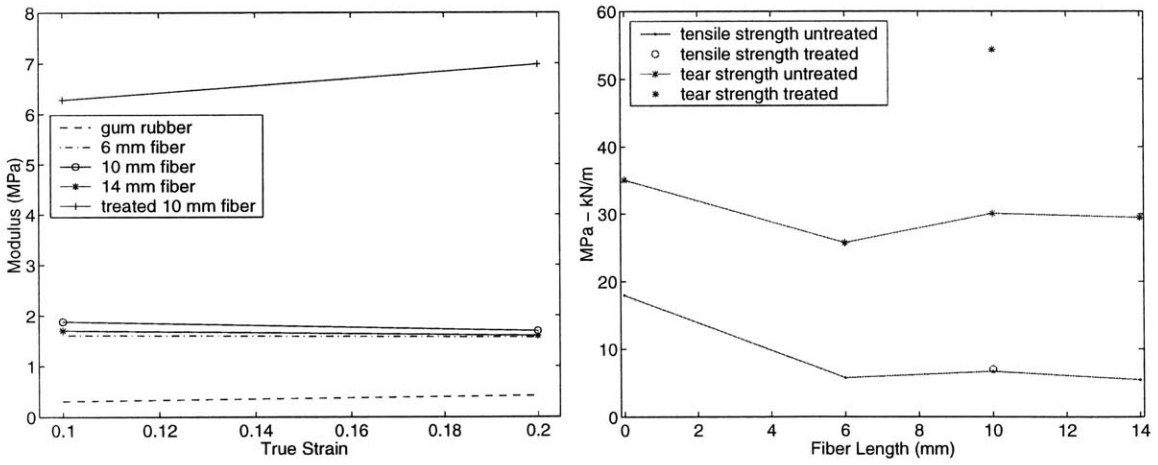

untreated fiber composites. The composite with 10 mm fibers treated with sodium hydroxide, an interfacial adhesion enhancer, exhibited a modulus several times greater than the moduli of all the composites with untreated fibers. Figure 1-1 (b) shows the fibers' influence on the tensile strength and tear strength. The gum rubber had a higher tensile strength than all the composite rubbers and a higher tear strength than

all the composites rubbers except the one filled with treated fibers. Good interface adhesion is necessary in order for the applied load to be transmitted efficiently from the matrix to the fibers.

Numerous investigators have reported similar results. Murty et al showed significant improvements in the modulus of natural rubber and styrene-butadiene rubber (SBR) with the addition of 6 mm long jute and 9 mm long glass fibers [3]. Moghe found that adding cellulose or high strength fibers to neoprene rubber increased the modulus but did not improve the strength [2]. Figure 1-2 (a) shows that the modulus

Figure 1-2: Effect of Cellulose and Aramid Fibers on the Mechanical Properties of Neoprene Rubber [2]

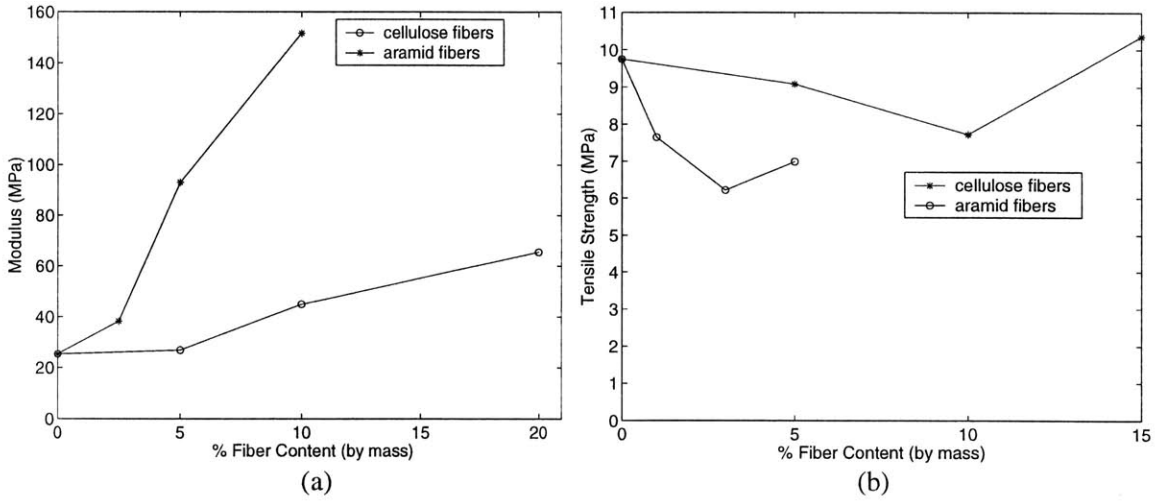

increased steadily with the filler fraction, but the tensile strength actually decreased in most cases. The fibers are typically several orders of magnitude stiffer than the matrix elastomer. At relatively low strains, the fibers bear a high proportion of the applied load, but, at large strains, the fibers debond from the matrix. The ultimate strength of the composite is therefore controlled by the properties of the matrix [2].

A number of different empirical relations, which show reasonable agreement with experimental data, have been proposed for the modulus of fiber-filled composites. Derringer [9], for example proposed an equation of the form

$$G = G_0 - 1 + \exp(aV^b),$$

where G is the Young's modulus of the composite, G_0 is the Young's modulus of the matrix, V is the volume fraction of the fiber, and a and b are constants. Figure 1-3 shows that the experimental results of Murty et al agree well with the Derringer equation.

Figure 1-3: Experimental Moduli of Jute and Glass Filled SBR and NR and Derringer Prediction [3]

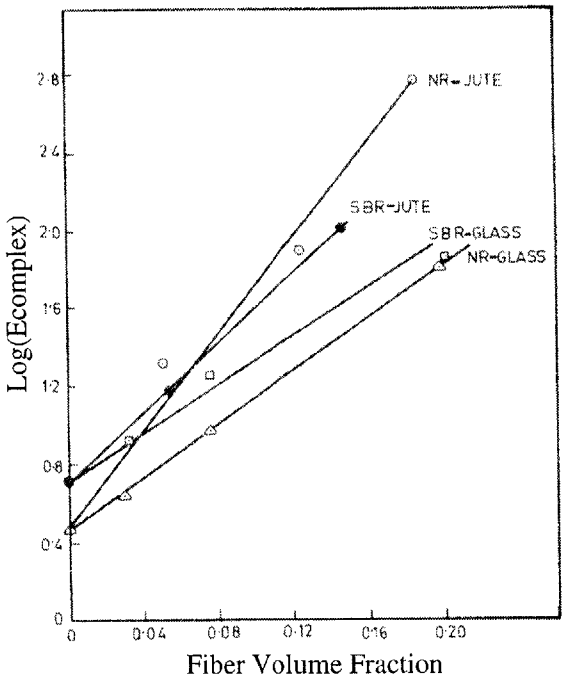

1.1.2 Effect of Fillers on Abrasive Wear

The abrasive wear behavior of elastomers is not so easily quantified and is not even phenomenologically understood. During abrasive wear, hard asperities dig and burrow into the elastomer surface resulting in large strains and high stress levels in the soft elastomeric material. Loss of material due to micro-tearing occurs and may eventually terminate the life of the elastomer. In fact, abrasive wear is often the major failure mode of elastomers [10]. The mechanisms of abrasive wear in elastomers will be discussed further in chapter 2.

Adding large ($\geq$1 μm) fibers to the elastomer further complicates the abrasive

wear mechanism. Material discontinuities and barriers to stress distribution, the fibers create high local stress concentrations. Abrasive wear can be considered fatigue fracture due to frictional, sliding forces [11]. Abnormally high local stresses due to the presence of fibers would seem to exacerbate the fatigue fracture process and increase the abrasive wear rate of the matrix material. On a microscale, in blister tests on polyurethane filled with 20 μm glass beads, Khan has shown that the particle-elastomer interface is the weak point in the elastomer where fracture is most likely to occur [12]. Furthermore, fiber pull-out can cause a large volume of material to be lost and leave a severely weakened surface. There is additional, contradictory evidence, however, that, on a continuum level, filler particles may prevent catastrophic failure by acting as obstacles to crack propagation [12]. Below, we briefly summarize two particularly relevant conflicting experimental results.

Fibers increase wear

Yang et al studied the effects of filler particles on the abrasive wear of elastomer composites [4]. Specifically, they looked at composites of silicone rubber filled with varying weight fractions and sizes of glass spheres (1-40 μm, 100-200 μm, and 700-1200 μm) and short glass rods (10 μm in diameter by 60 μm long). Discs of the materials were spun against a pair of abrasive wheels in a Taber Abrader setup, and weight loss was measured at regular timed intervals. Figure 1-4 shows the results for the short rods and the three sizes of spheres. In all cases, wear increased with the addition of the fillers, and the amount of material removed was proportional to the weight fraction of the filler.

From scanning electron microscopy (SEM) observations, Yang identifies three different wear mechanisms depending on the size of the filler particles relative to the size and spacing of the abrasive asperities (100-200 μm). For spheres smaller than the asperities, the increase in wear rate is attributed to the weakening effect of stress concentrations around the filler particles. Quantified in Figure 1-4 (b), this effect intensified with the composites of similar size short glass rods due to the enhancement of the stress concentration around the ends of the rods. With the medium size

Figure 1-4: Wear Rates of Silicone Rubber with Sphere and Rod Fillers [4]

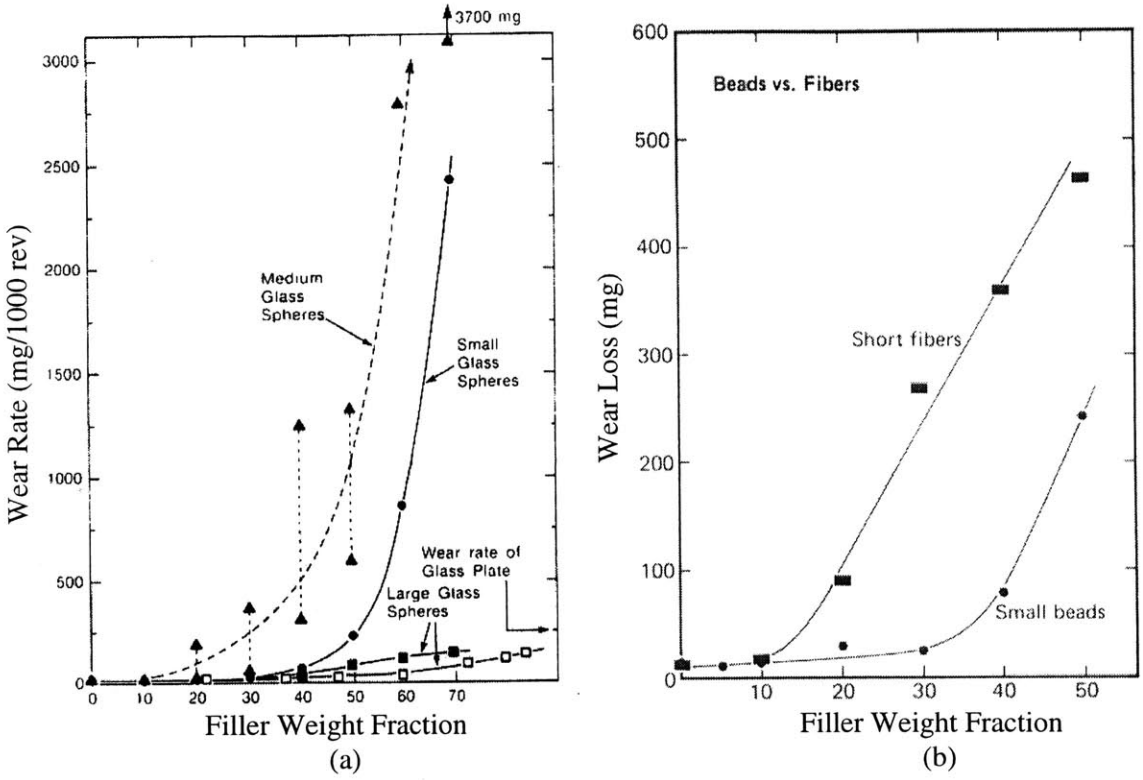

spheres, the increase in the wear rate is attributed to fiber pull-out. Pull-out occurred most frequently with the medium size spheres because the deformations in the elastomer caused by the abrasive asperities were similar in size to the filler particles. For spheres larger than the asperities, the increase in wear is attributed to the fibers, which bear a much higher proportion of the applied load than the surrounding soft matrix material, being less wear resistant than the rubber. As indicated in Figure 1-4 (a), of the sphere-filled materials, composites with the medium size spheres exhibited the worst wear resistance while composites with the large spheres showed the best wear resistance.

Fibers decrease wear

Wada and Uchiyama examined the wear properties of polyamide fiber-reinforced chloroprene rubber (SFRR) [13]. Specimens were pressed against a rotating cylin-

der wrapped with metal gauze or abrasive paper. Specimens with fibers oriented longitudinally (L), transversely (T), and normally (N) to the sliding direction were tested at various speeds and loads. With three different types of abrasive surfaces, all three filled materials exhibited wear a resistance superior to that of the unfilled chloroprene rubber. Of the filled materials, the N-direction SFRR showed the minimum wear rate while the T-direction SFRR showed the maximum wear rate.

In these experiments, the fibers were significantly larger than the surface roughnesses of the abrasive surfaces. The fibers measured 3 mm in length and 28 μm in diameter while the abrasive surfaces had average roughnesses of 2.1, 12.5, and 20 μm. Similar to Yang et al for the case of large sphere-reinforced silicone rubbers, Wada and Uchiyama postulate that the fibers act as load bearers. Much harder than the surrounding matrix material, the fibers support a high proportion of the normal force and, hence, reduce the frictional force on the matrix material. We speculate, therefore, that the polyamide fibers must be more wear resistant than the chloroprene rubber. The wear rates of the composites were determined by their susceptibility to fiber pull-out. SEM observations showed that the N-direction SFRR, with the fibers protected by the matrix material along their entire length, was the least susceptible to fiber pull-out and was therefore the most wear resistant.

1.2 Caterpillar Undercarriage Seal Application

1.2.1 Description

Caterpillar Inc. is the world's leading manufacturer of track-type tractors. Often referred to as "bulldozers," (see Figure 1-5), these earth-moving machines have engine sizes ranging from 70 to 770 horsepower. Their wheels translate power to the ground by turning a metal track which provides the tractor with an enormous amount of traction. The track is comprised of numerous links, each connected by the pin-joint assembly shown in Figure 1-6. The cogs of the tractor's wheel contact the cylindrical bushing which turns freely about the pin. End caps are bolted onto both ends of

Figure 1-5: Track-Type Tractors

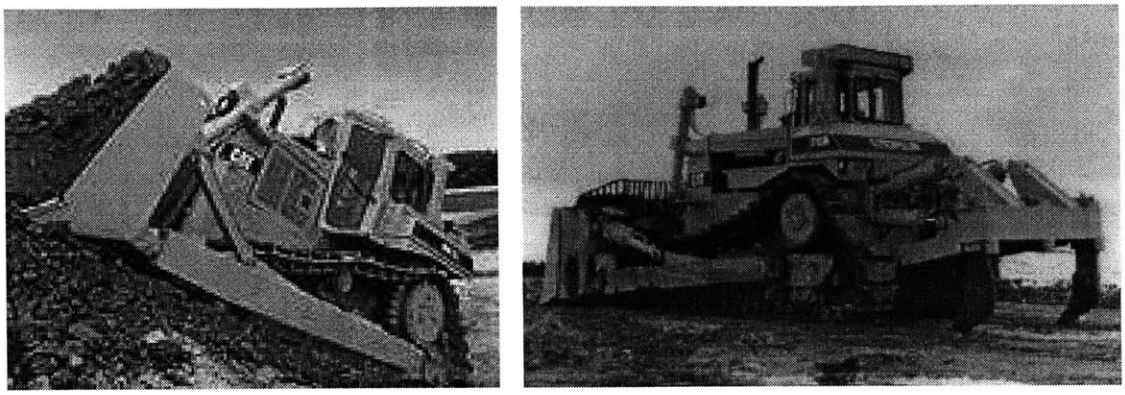

the pin. Prior to assembly, seals are pressed into the end caps in order to maintain lubricant between the pin and bushing and prevent contaminants from entering the joint. The seals and the flat ends of the bushing are in contact and in motion relative

Figure 1-6: Pin-Joint Assembly [5]

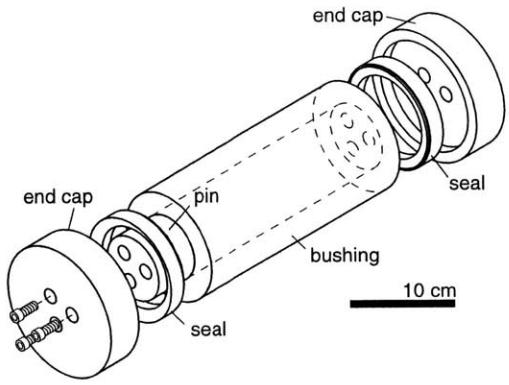

to one another. This type of seal, which contacts its bearing surface along a plane, is classified as a face seal.

Illustrated in Figure 1-7, the components of a track seal, are the load ring, the stiffener ring, and the seal lip. The seal lip is the part of the seal that contacts the bushing surface and provides the actual sealing mechanism. A soft elastomeric material, the lip deforms when loaded to provide a substantial contact band. The seal lip is bonded to the much harder glass fiber-filled polycarbonate stiffener ring

Figure 1-7: Track Seal [5]

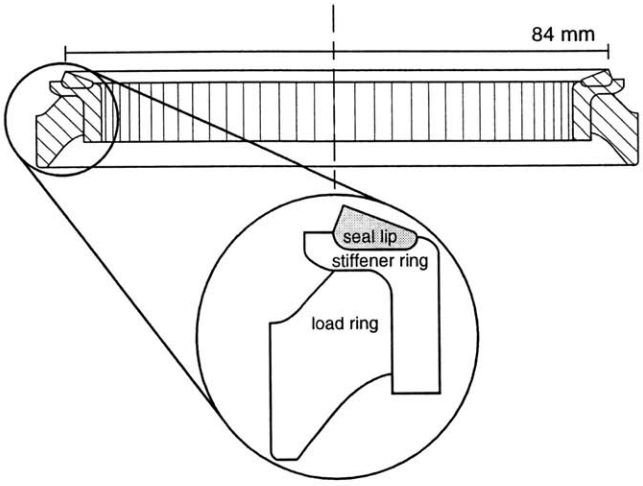

during manufacturing. The stiffener ring fits into the nitrile rubber load ring under sufficient compressive force that no relative rotational motion can occur. The load ring is pressed into the end cap and maintains the required contact pressure between the seal lip and the bushing surface.

The track seal's primary function is to maintain lubricant in the joint. Once the lubricant escapes, friction between the pin and bushing quickly destroys the joint. As the track moves, the seal and bushing are in constant oscillatory motion relative to one another. Depending on the operating conditions of the tractor, the track may be submerged in a variety of aggressive abrasive environments. The track seal eventually fails due to abrasive wear. Because of recent advances in bushing materials, in some environments, the seal is now the limiting factor in the life of the track. Replacing the seals is time consuming, costly, and inconvenient not only for the customer but also for the Caterpillar dealers that must perform the labor. Developing the most wear resistant seal lip material possible is therefore economically very desirable.

1.2.2 Seal Lip Material

Having realized that the abrasive wear life of the track seal is so crucial, Caterpillar has considered a number of different thermoplastic polyurethane (TPU) based composites.

Lacking primary crosslinking between chains, thermoplastic elastomers allow tight tolerance injection molding and the re-use of scrap material. These materials all met the basic requirements of the seal lip for compression set, thermal stability, oil resistance, and tensile properties. Several different polyurethanes and filler packages were tested. The filler packages included varying percentages by weight of glass and ceramic fibers.

1.2.3 Caterpillar Experimental Data

Caterpillar used two tests to evaluate the abrasive wear resistance of potential seal lip materials – the variable load wear test and the mudbox torsion test.

Variable Load Wear Tests

Flat annular disks were cut from 3 mm thick injection molded plaques of the material. The test samples were mounted on a spindle and rotated at 200 rpm against an abrasive wear plate with a surface roughness of 1.15 μm under a 200 lb load for 1000 minutes. The percent wear loss was calculated based on the change in thickness of the specimen. A Caterpillar developed polyurethane filled with 2% ceramic and 2% glass fibers by mass and five unfilled polyurethane samples were tested. The wear resistance of the filled elastomer was superior to that of all five unfilled elastomers.

In a similar test, the load was increased in increments of 100 lbs at 60 minute intervals. The interface temperature was measured every 50 seconds. Interface temperature was shown to accurately reflect the amount the sample had worn. Three different polyurethanes with and without a filler package of 2% glass and 2% ceramic fibers by mass were tested. In all three cases, the interface temperature was consistently lower for the composite material than for the unfilled polyurethane.

Mudbox Torsion Test

The mudbox torsion test was designed to duplicate the operating conditions that a seal experiences in the field. Track seals were injection molded from several filled and

unfilled polyurethanes. Pressed against the bushing with a force of 2000 to 2500 N, the seal oscillated relative to the stationary bushing with an amplitude of ±15 degrees at a frequency of one cycle per second. The entire assembly was immersed in a slurry of clay, sand, and water. After 3,250,000 cycles of operation, the percent lip wear was calculated based on the fraction of the seal lip that had been destroyed. The results for six materials previously tested with the variable load wear test and five new materials are summarized in Table 1.1. All filled samples again exhibited wear

Table 1.1: % Lip Wear in Mudbox Torsion Test

material	% glass	% ceramic	% lip wear
TPU #1	0	0	43
	2	2	32
TPU #2	0	0	57
	2	2	30
TPU #3	0	0	34
	2	2	22
	3	3	25
	6	6	32
	6	0	22
	0	6	29
	3	6	26

resistance superior to that of all unfilled samples. TPU #3 containing 2% glass/2% ceramic and 6% glass fillers showed the least lip wear at 22%. Increasing the filler fraction in TPU #3 above 6% proved detrimental to the elastomer's wear resistance.

1.3 Research Motivation

While the data in the literature is in disagreement on the effect fillers have on the wear resistance of elastomers, the Caterpillar experimental data conclusively shows the filled polyurethanes outperforming the unfilled polyurethanes. The question is what is it about the materials or the application that enables fibers to reduce wear in this particular case? The goal of this project was to identify, understand, and quantify the wear mechanism of fiber-filled elastomers in the presence of abrasive

environments. With this knowledge, one could maximize the wear resistance of these composites.

The advantage of a longer lasting track seal is self-evident – the components of the track pin-joint will be better protected, seal replacement will be required less frequently, and machine down-time will be reduced. The ultimate objective, however, was to learn something from this particular application that could be applied in a much broader sense. Fiber-filled elastomers are very commonly used in environments where abrasive wear is a concern. Examples include numerous other sealing applications, polishing, tires, tillage equipment [14], gravel processing plant conveyor belts, and drilling mud pumps [15] among others.

1.4 Thesis Outline

The objective of this thesis was to explore the role of fibers in the abrasive wear of fiber-filled elastomers. This was accomplished via a combination of finite element analysis and experiments.

The first step was to obtain repeatable experimental data for the materials under consideration. Chapter 2 therefore presents results from seal wear experiments with filled and unfilled elastomer seals operating in the presence of a standard abrasive slurry comprised of a range of particle sizes. It is observed that seal life can be divided into two periods – a "break-in" period before wear begins followed by an "aggressive wear" period during which wear occurs at a relatively rapid and constant rate. These experiments definitively establish that the fibers increase the life of the seal by delaying the initiation of wear but do not significantly affect the wear rate once the aggressive wear period begins. It is observed that the end of the break-in period is marked by the formation of critical size clusters of particles that grow steadily in size as the aggressive wear period progresses.

The results of surface analyses performed on both filled and unfilled elastomer seal lips are presented in chapter 3. They show that the filled elastomer seal lips have a significantly higher surface roughness than the unfilled elastomer seal lips.

Furthermore, the results indicate that fibers are present at or immediately below the surface of the elastomer.

Micromechanical modeling of the abrasive wear of unfilled elastomers is presented in chapter 4. A two-dimensional plane strain elastomer block is first compressed and then sheared over a circular rigid particle on a flat rigid surface. The resulting stress and strain distributions after compression and during shearing, both with and without friction, are analyzed. Similarities are noted between the simulation results and the elastomer deformation patterns observed by numerous investigators.

Chapter 5 describes the micromechanical modeling of the abrasive wear of filled elastomers. Simulations similar to those in chapter 4, but with fibers added to the elastomer blocks, are performed for comparison with the unfilled case. Compression simulations with 5, 15 and 30 μm diameter particles and fibers at normal, tangential, and longitudinal orientations show that, in most cases, the addition of fibers increases the maximum tensile stress in the elastomer. It is noted that this result agrees well with the experimental result that fibers do not affect the aggressive wear rate of the seal lip. Shearing simulations with two fibers oriented parallel to one another at the three different orientations indicate that the fibers impede particle motion between the elastomer and the rigid surface. It is postulated that this is a mechanism by which fibers deter particles from clustering.

Having shown that fibers exist near or at the surface of the seal lip in the analyses of chapter 3, in chapter 6, we investigate the effect that fibers near or at the surface of an elastomer block have on the contact stress distribution between the elastomer and the rigid surface. Sharp peaks exceeding the average contact stress value are observed below the fibers while, adjacent to the fibers, regions with a contact stress less than the average value are seen. It is theorized that the peaks at the fibers interfere with cluster formation while the regions of lower contact stress around the fibers may increase the lubrication of the seal/bushing interface.

Results of experiments conducted with abrasive slurries composed of particles in well defined size ranges and particle size analyses of the various slurries are presented in chapter 7. It is determined that wear is caused by particles less than 5 μm in

effective diameter. Furthermore, the fibers are shown to be ineffective against slurries with high concentrations of micron or sub-micron size particles. It is concluded that the fibers extend the break-in period of the seal by interfering with the clustering of particles similar in size to the fibers.

In chapter 8, several seal lip surface microtexture designs are proposed to simulate the effect of the fibers on the contact stress between the seal lip and the bushing surface. These seals are to be manufactured and tested. Achieving an an improvement in wear resistance similar to that observed with the smooth filled elastomer seal lip with a microtextured unfilled elastomer seal lip not only would further validate the theories developed in chapters 5 through 7 but also would be a significant advance in seal technology.

Chapter 9 offers some concluding thoughts and directions for future work on this topic.

Chapter 2

Track Seal Experiments

Track seal wear experiments were conducted in order to verify the Caterpillar results and, by using a visualization technique, to directly observe the wear process. Developed by Ayala [6], the experimental setup described below closely approximates the operating conditions of a seal in the field. Both filled and unfilled polyurethane seal lip materials were tested.

2.1 Experimental Setup

The overall setup of the experiment is illustrated in Figure 2-1. Figure 2-2 depicts

Figure 2-1: Experimental Setup Overview [5]

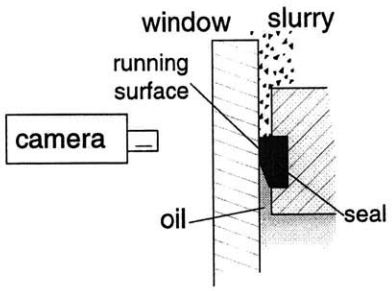

how the seal assembly is inserted into a mount on the test rig and a glass window is pressed against the seal lip to act as the seal's bearing surface. Ayala has shown that the wear rate of a seal running against glass is nearly four times that of a seal running

against a steel bearing surface such as the bushing in the pin-joint assembly. Ayala, however, also determined that the abrasion patterns and hence the wear mechanisms are the same [5]. Oil is poured into a cavity in the rig until it fills the volume within

Figure 2-2: Track Seal Experimental Test Rig [5]

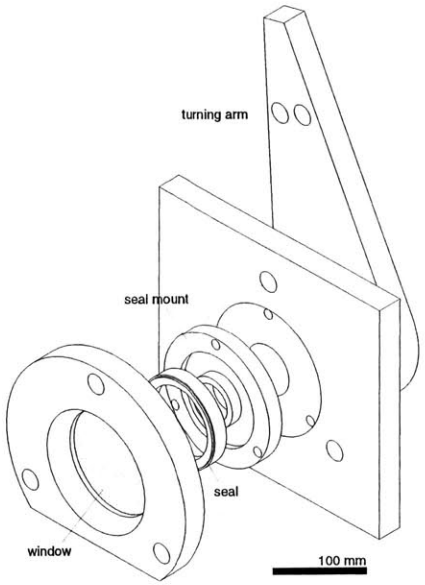

the seal. As in the actual pin-joint application, the seal prevents the oil from leaking. The seal mount and seal oscillate with an amplitude of ± 15 degrees at a frequency of 30 cycles per minute. This corresponds to a maximum distance traveled of 22.3 mm/cycle and a maximum sliding speed of 11.1 mm/second. An abrasive slurry is maintained on the outside edge of the seal.

The use of the glass window allows direct observation of the entire seal lip wear process. A CCD camera is focused on the outside edge of the seal lip. An electro-mechanical trigger instructs the camera, via a video capture board, to capture an image each time the seal stops at one extremity of its oscillation. A computer stores the images and records the cumulative number of cycles of operation. The images measure 520 pixels wide by 460 pixels tall and correspond to an area on the seal lip 2.05 mm wide by 1.81 mm tall. An example of a typical image is shown in Figure 2-3.

For this experiment, wear is defined as the extent of dirt penetration. Abrasive

Figure 2-3: CCD Image of Track Seal [6]

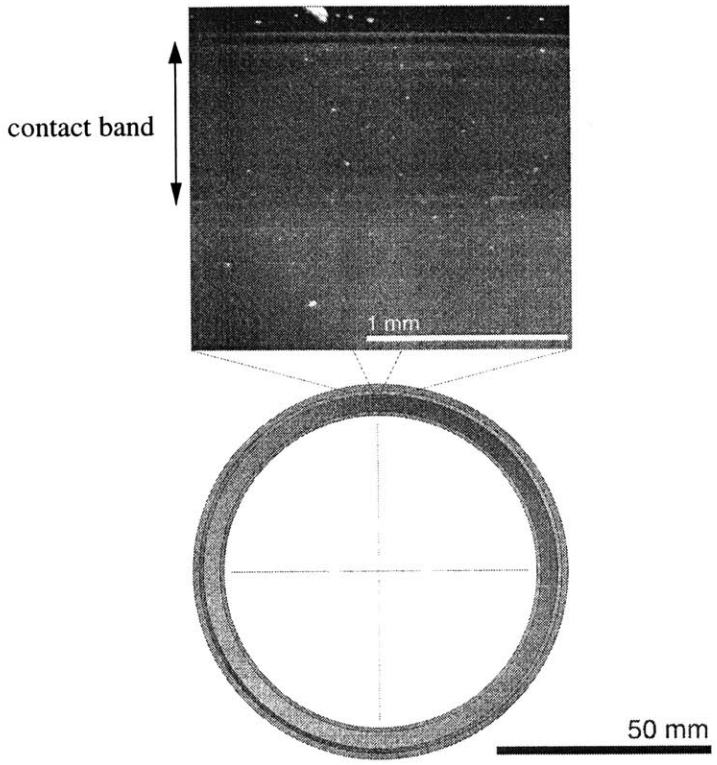

wear of the seal lip occurs as slurry particles enter the seal lip contact band. In a cyclic process, material removal from the seal lip allows more particles to enter which, in turn, cause additional wear. From the recorded images, the location of the inward tip of the dirt front is calculated at regular cycle increments. The extent of dirt penetration is expressed as a percentage of the total seal lip width and plotted as a function of the number of cycles of operation. This relationship is termed a "wear curve." The experiments were stopped when dirt had penetrated the entire width of the contact band and had begun to fall into the oil.

The abrasive slurry used was a standard mixture provided by Caterpillar. By weight, the slurry, also fondly known as "mud," was approximately 29.5% fireclay, 39.3% bank sand, 0.2% Cabosyl, 0.1% salt, and 30.9% water. The slurry was applied to the outside of the seal lip with a squeeze bottle at one minute and 15 second intervals. Frequent application of the slurry was crucial to maintaining a sufficient

layer of active, percolating debris immediately outside the seal lip. If one stops adding the slurry or allows the slurry right at the edge of the seal lip to dry out, wear ceases.

By the above definition, wear does not occur unless an abrasive slurry is present. An alternative definition of seal wear is lubricant leakage. The seal's ultimate purpose, after all, is to maintain oil in the joint. Once dirt penetrates the contact band and erodes enough seal lip material, oil loss will occur. The two definitions of wear are not equivalent but clearly related. It is important to note that material removal and oil leakage do not occur in the absence of an abrasive slurry. Wear, by any definition, occurs only when the seal is operating in an abrasive slurry.

2.2 Unfilled Elastomer Seals

The unfilled seal lip material is a commercially available polyurethane. The seal lip has an outside diameter of 84 mm and a width of 5 mm. The seals were compressed against the glass window with sufficient pressure to produce a 1 mm wide contact band. This was the largest contact band that could be obtained repeatedly with the experimental setup. From a finite element analysis using the Arruda-Boyce Eight Chain material model, the maximum contact pressure was calculated to be 7.9 MPa at the outer edge of the seal lip, and the total face load was calculated to be 1260 N.

Four identical tests were run under the preceding conditions. Displayed in Figure 2-4, the results indicate excellent agreement between the four tests. Debris almost immediately penetrates the contact band and advances at an essentially constant rate. Test 4 was stopped short of seal failure but shows the same trend as Tests 1-3.

The relevant data is summarized in Table 2.1. The break-in period is defined as the number of cycles of operation before the dirt front forms and begins to advance. The aggressive wear rate, expressed in units of mm/cycle, is the rate at which the dirt front advances once the break-in period has ended. The average break-in period was 550 cycles, and the average aggressive wear rate was 3.90×10^{-4} mm/cycle.

Figure 2-5 shows select images from a representative unfilled elastomer seal test. The number under each frame indicates the cumulative number of cycles of operation.

Figure 2-4: Seal Wear Data: Unfilled Elastomer Seals

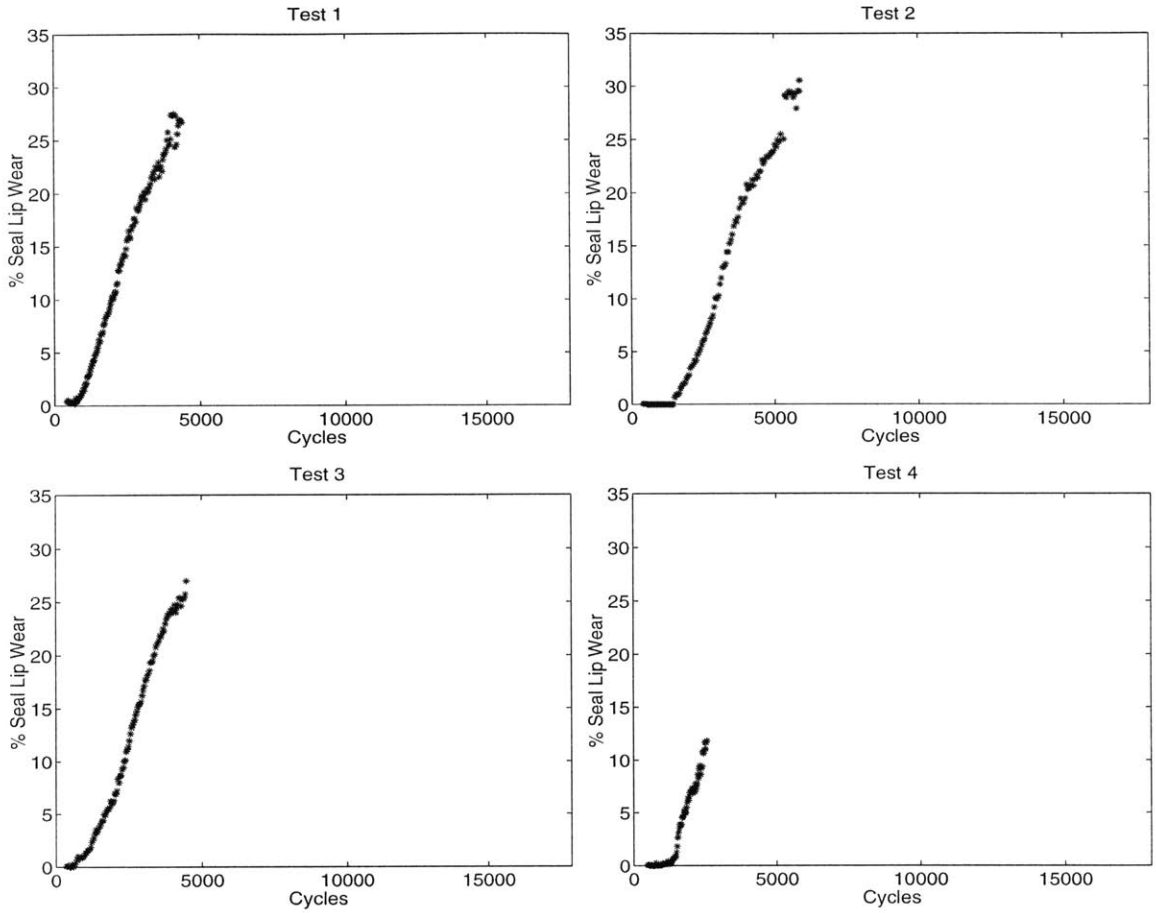

Table 2.1: Summary of Unfilled Elastomer Seal Wear Tests

	Break-In Period (cycles)	Aggressive Wear Rate (mm/cycle $\times 10^{-4}$)
Test 1	270	3.96
Test 2	1060	3.84
Test 3	310	4.12
Test 4	780	3.66
average	550	3.90

The slurry is first added at 386 cycles. Almost immediately, at 734 cycles, a visible layer of debris forms in the seal lip contact band. At 968 cycles, small clusters of particles on the order of 100 μm in size are visible. The clusters have a distinct tear shape and grow in size until they occupy the entire seal lip contact band. Particles begin to fall into the oil shortly after 4478 cycles.

Figure 2-5: Seal Wear Sequence: Unfilled Elastomer Seal (Test 3)

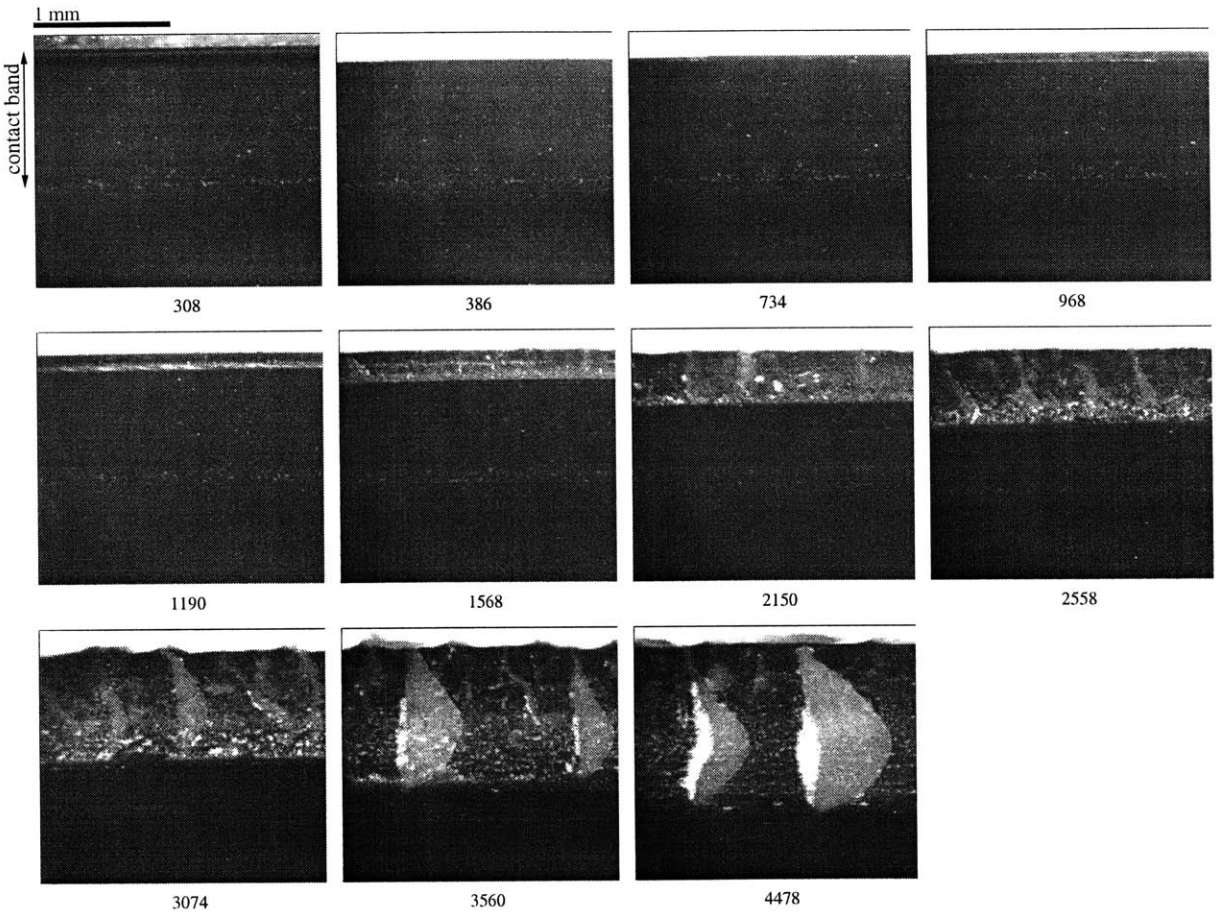

2.3 Filled Elastomer Seals

The filled elastomer seal lips are molded from the same polyurethane that is used in the unfilled elastomer seal lips. Cylindrical glass fibers, with a diameter of 16 μm and a length to diameter ratio of approximately 8, are added at a mass fraction of 4%.

Figure 2-6: Seal Wear Data: Filled Elastomer Seals

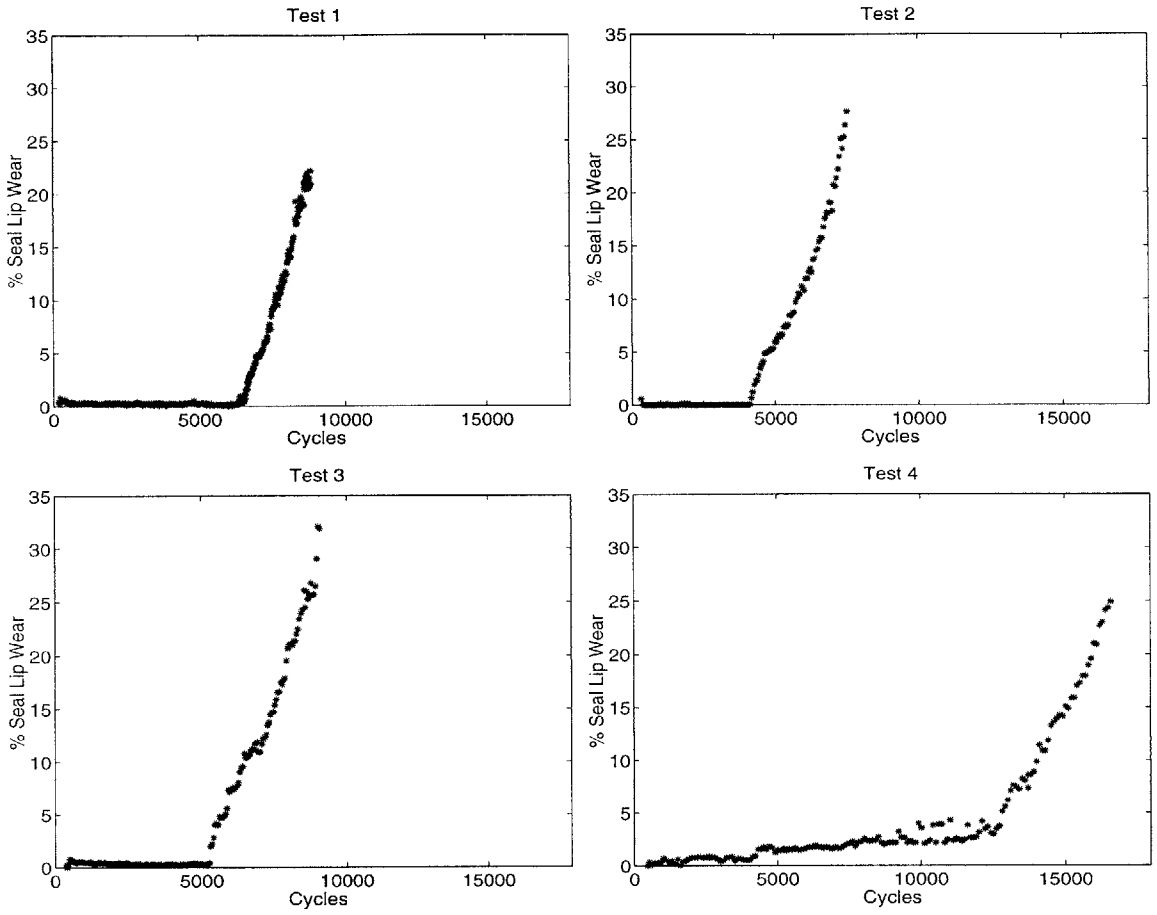

The dimensions of the filled and unfilled elastomer seals are identical. The seals were compressed against the glass window with sufficient force to produce a 1 mm wide contact band. From a finite element analysis using the Arruda-Boyce Eight Chain material model, the maximum contact pressure was calculated to be 9.0 MPa at the outer edge of the seal lip, and the total face load was calculated to be 1464 N.

Four identical tests were run. Displayed in Figure 2-6, the results indicate that the break-in periods of the filled elastomer seals are significantly longer than the break-in periods of the unfilled elastomer seals. Aggressive wear, however, occurs at the same nearly constant rate as in the unfilled elastomer seal tests.

The relevant data is summarized in Table 2.2. Excluding Test 4, which exhibited a much longer break-in period and slightly slower aggressive wear rate than Tests 1-3,

Table 2.2: Summary of Filled Elastomer Seal Wear Tests

	Break-In Period (cycles)	Aggressive Wear Rate (mm/cycle $\times 10^{-4}$)
Test 1	6110	4.28
Test 2	3790	3.91
Test 3	4800	3.75
Test 4	12,060	2.5
average excluding Test 4	4900	3.98

the average break-in period was 4900 cycles, and the average aggressive wear rate was 3.98 $\times 10^{-4}$ mm/cycle.

Figure 2-7 shows select images from a representative filled elastomer seal test. The slurry is added at 322 cycles. Close examination reveals a thin layer of debris present in the outermost portion of the seal lip contact band at 940 cycles. At roughly 4158 cycles, visible clusters of particles appear, and aggressive wear begins. The critical size clusters again appear to be on the order of 100 μm in size. From this point on, the filled elastomer seal test is identical to the unfilled elastomer seal test. The tear-shaped clusters grow in size until the seal fails at roughly 7500 cycles.

2.4 Wear Surface Observations

Scanning electron microscopy of tested seals is used to characterize the aggressive wear phenomenon. Figure 2-8 shows the contact band surfaces of experimentally worn filled and unfilled elastomer seal lips. The seals in Figure 2-8 were run to failure and have therefore experienced aggressive wear across the entire width of their contact bands. The physical appearance of the abraded polyurethane is very similar for both the filled and unfilled elastomer seal lips. We see many small ridges normal to the sliding direction where tearing and material removal has occurred. Figure 2-9 shows the same seals at a much higher magnification. The wear surfaces of both seal lip materials show features typical of the abrasive wear of elastomers. Abraded elastomer

Figure 2-7: Seal Wear Sequence: Filled Elastomer Seal (Test 2)

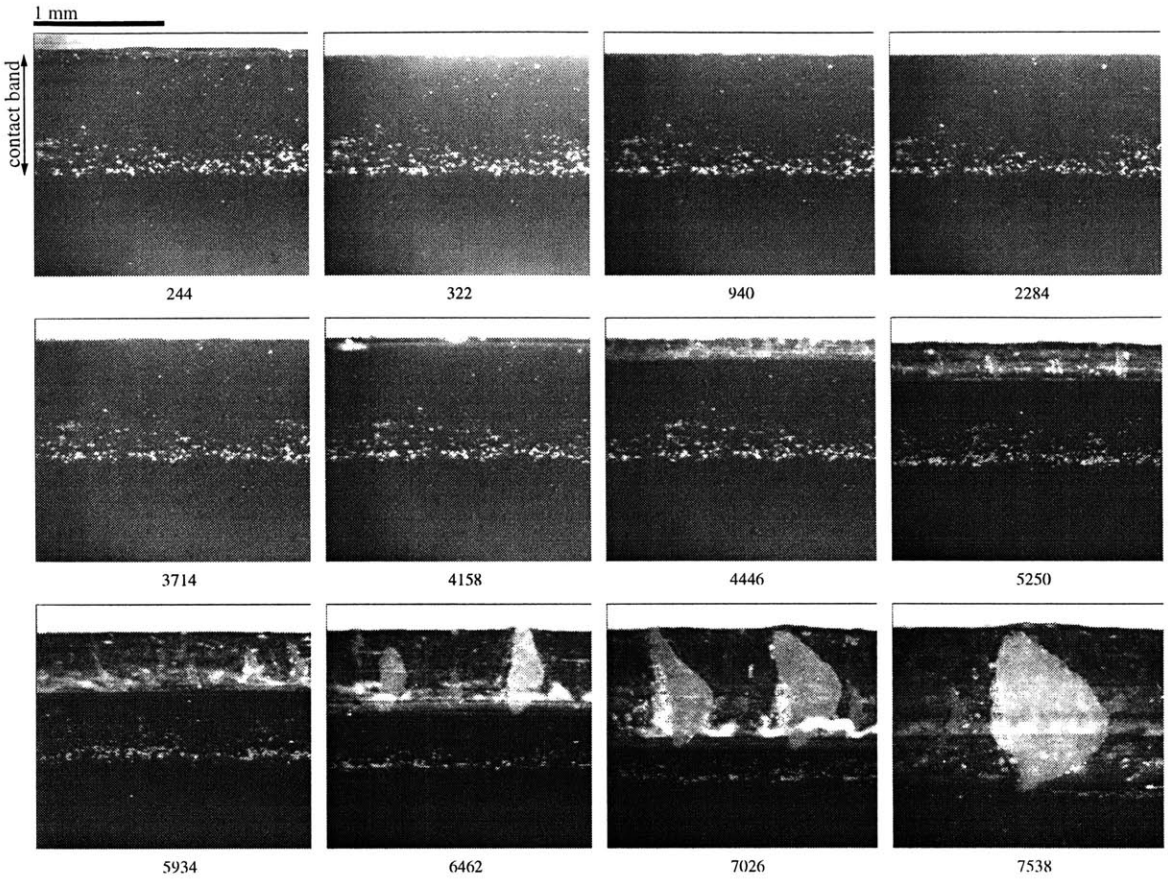

surfaces commonly exhibit periodic ridge formation in a direction perpendicular to the sliding direction [16].

Numerous investigators have shown that ridge patterns form during the abrasive wear of elastomers. Generally the size and, due to small ridges coalescing in the sliding direction, the spacing increases until a steady state condition is reached. Barquins reported ridge formation after repeatedly sliding a rigid, smooth hemispherical asperity unidirectionally across a specimen of silica-filled natural rubber [17]. In sharp tip abrader experiments on unfilled and silica-filled ethylene vinyl acetate rubber, Mukhopadhyayh et al observed ridge formation normal to the direction of rotation [18]. Fukahori and Yamazaki observed this characteristic wear pattern after repeated unidirectional slidings of unfilled and carbon black-filled natural rubber in contact with a razor blade type abrader [19]. Furthermore, Mok and Gorman performed ex-

Figure 2-8: SEM of Worn Seal Lip Contact Bands (1)

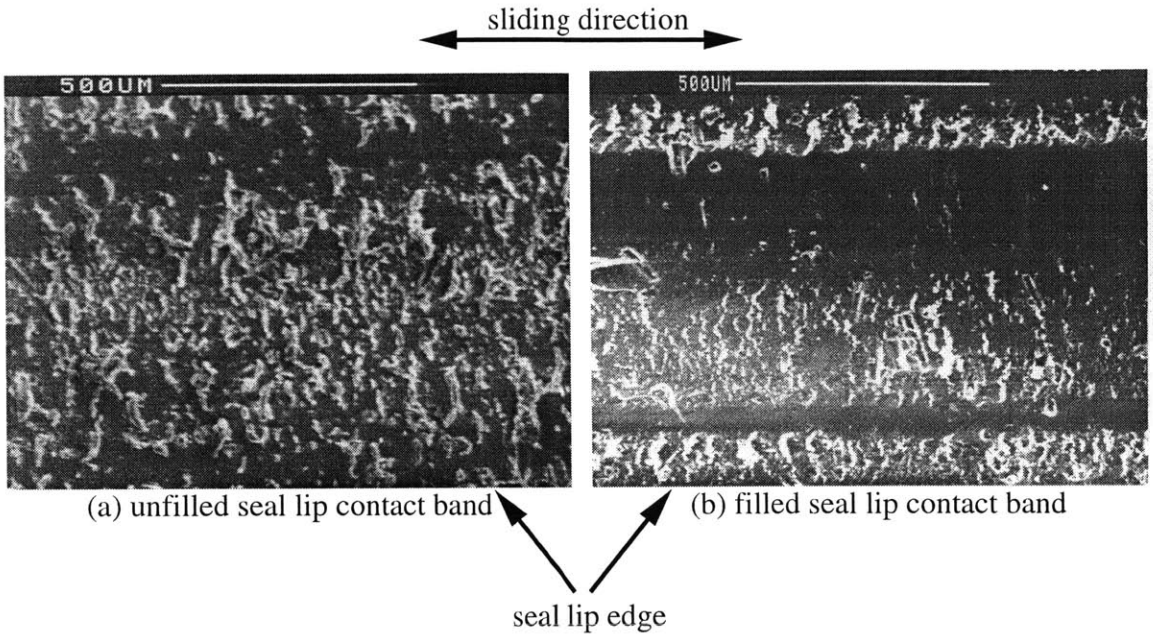

Figure 2-9: SEM of Worn Seal Lip Contact Bands (1): High Magnification

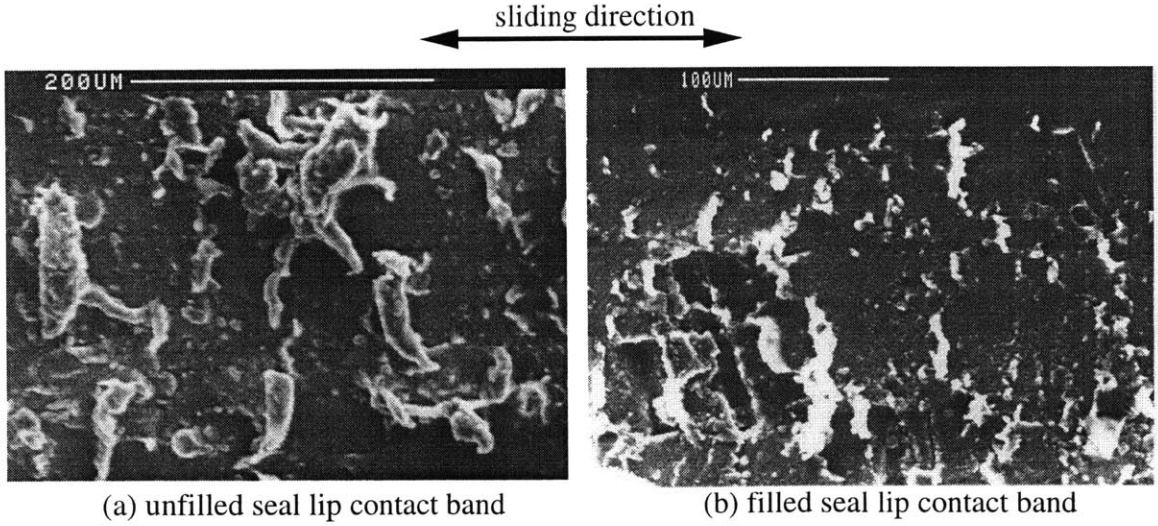

periments with nitrile rubber reciprocating on steel in the presence of drilling mud and abrasive sand. They observed that the ridge formation in wet three body abrasion was similar to that in dry abrasion [15].

Both Mukhopadhyay et al [18] and Fukahori and Yamazaki [20] reported that the ridge spacing and height decreased with increasing filler content. Mukhopadhyay et al also measured a decrease in abrasion loss by volume with increasing filler content. This result is in agreement with the common belief that abrasion severity increases with ridge height and spacing [16].

Numerous theories have been proposed to explain the ridge formation phenomenon. Schallamach was one of the first to study the nature of the contact between a hard slider and a soft rubber [21]. He observed an asymmetric contact area with material compressed in front of and stretched behind a moving slider. He discovered that sliding occurred when the tangential compressive stresses in front of the contact area became high enough for the rubber to buckle. Schallamach considers the high tensile strains near the trailing edge of the contact area the source of tensile failure and abrasion. Barquins attributes the ridges formed by a blunt type abrader to the sawing off of the crests of viscoelastic ridges that form in front of the slider [17]. Gent has proposed a general theory for elastomer abrasion where, due to microcracking events at voids inside the material, wear initiates with the detachment of small 1-5 μm particles [22]. Continued erosion of the pitted surface leads to the removal of pieces of rubber on the order of 100 μm in size. The tearing away of these larger particles constitutes the majority of the material removal and produces the ridge pattern. Fukahori and Yamazaki ascribe the ridge formation to the stick-slip motion of rubber in contact with sharp asperities [19]. Similar to what Schallamach reported, in Fukahori and Yamazaki's experiments, the hard slider stuck to the rubber surface compressing it until enough energy was stored in the rubber to cause a sudden break with a consequent very rapid slip. Fukahori and Yamazaki theorize that microcracks, initiated by microvibrations during the slip phase, propagate and link together during the stick phase to form the large ridges. They attribute the decrease in ridge size and spacing with the addition of carbon black to the increase in both the natural

frequency of the rubber and the stick-slip frequency. While Mukhopadhyayh et al do not speculate on the mechanism at work, they correlate the decrease in ridge size and spacing in the filled rubbers with an increase in fracture resistance [18]. It is well known that the addition of particulate fillers of 0.1 μm or less such as carbon black or silica substantially enhances the fracture energy and abrasion resistance of elastomers [11]. Hamed attributes the increase in fracture energy to the numerous interactions between broken or dangling polymer chains and the closely spaced, high specific area particles [11].

While the ridges on the surfaces of the worn seal lips may not be as beautiful and periodic as those produced under controlled conditions by investigators in the laboratory, they are certainly present. The ridges in Figures 2-8 and 2-9 are relatively uniform in size and spacing in the sliding direction. Furthermore, in agreement with the results in the literature, which granted are for fillers much smaller in size than the glass fibers, the ridges on the surface of the unfilled elastomer seal lip are marginally larger and further apart than the ridges on the filled elastomer seal lip. This indicates that more material may have been removed from the unfilled elastomer seal lip during the aggressive wear period. The approximate typical ridge spacing is 75 μm for the unfilled elastomer seal lip and less than 50 μm for the filled elastomer seal lip. The characteristic ridge spacing dimension is much smaller than the typical fiber spacing which we show in chapter 8 is typically on the order of 200 μm. We note that in Figure 2-9 (b) there are numerous ridges in the area between the cavities left by pulled-out fibers. It is therefore unlikely that the fibers significantly affect the ridge formation and aggressive wear mechanism.

The SEM pictures of worn seal lips in Figure 2-10 exhibit a slightly different abrasion pattern. Although the largest ridges are substantially bigger than those seen in the corresponding pictures in Figures 2-8 and 2-9, the ridges on the filled elastomer seal lip are still smaller and closer together than the ridges on the unfilled elastomer seal lip. The spacing of the largest ridges is approximately 150 μm for the unfilled elastomer seal lip and 100 μm for the filled elastomer seal lip. Moving perpendicular to the sliding direction towards the inside of the seal lip, however, the

Figure 2-10: SEM of Worn Seal Lip Contact Bands (2)

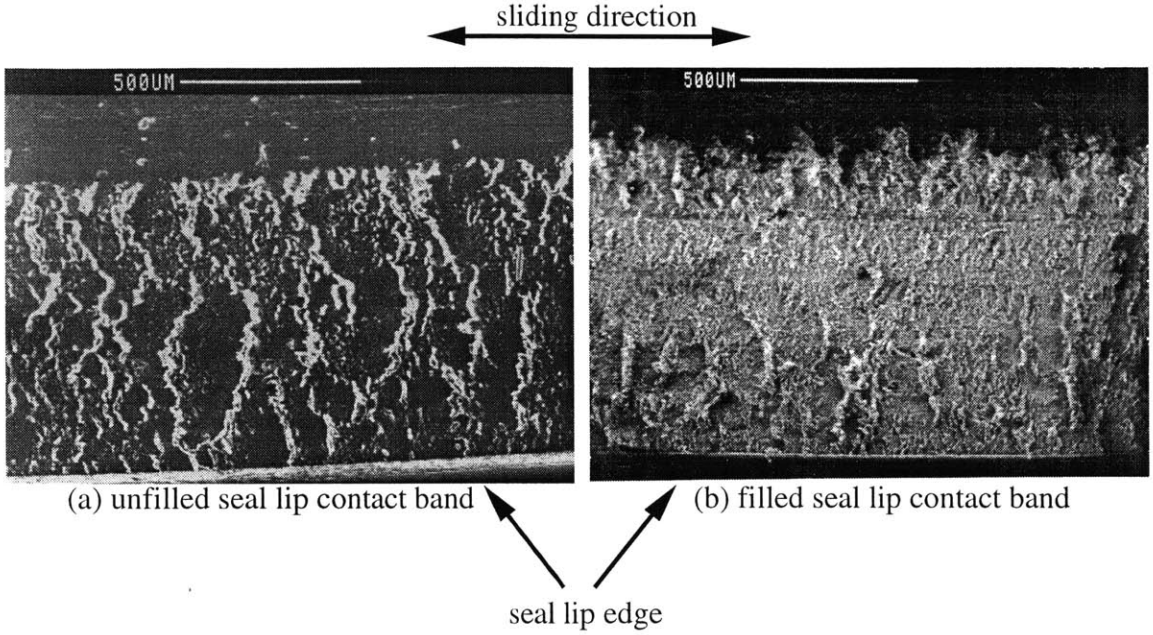

size and spacing of the ridges decrease to the magnitudes observed in Figures 2-8 and 2-9. As the clusters penetrate the seal lip, they grow in size such that they always span the entire width of the contact band. The region near the outside of the seal lip therefore experiences more cycles of abrasive wear and more material removal than the region further inside the seal lip. The large ridges near the outside of the seal lip are likely at or close to steady state size and spacing while the smaller ridges further inside are still growing and coalescing.

While the seal lips in Figures 2-8 and 2-10 show different abrasion patterns, they had nearly identical aggressive wear rates. More material was certainly removed from the seal lips with the larger ridges. It is clear, however, from the relatively small, closely spaced ridges throughout the contact bands in Figure 2-8 and at the inside of the contact bands in Figure 2-10, that only a minimal amount of material removal is necessarily associated with the dirt's advance. The majority of the material removal occurs on the area of the seal lip behind the innermost tip of the dirt front after the seal lip is "worn" by our definition. While the fibers might affect the rate of material removal once the ridge spacing approaches the fiber spacing, they clearly do not affect

the material removal process at the point of dirt penetration and therefore have no influence on the aggressive wear rate.

2.5 Conclusions

Preliminary experimental work indicates that fibers increase the wear resistance of track seals by prolonging the break-in period. The aggressive wear rate of filled and unfilled elastomer seals is nearly identical. Furthermore, SEM observations show that the aggressive wear mechanism is similar for the two seal lip materials. Both the filled and unfilled elastomer seal lips exhibit the ridge formation pattern characteristic of the abrasive wear of elastomers.

While the spacing and height of the ridges indicate that more material may be removed from the unfilled elastomer seal lip, by our measure, the rate of dirt penetration, the aggressive wear rate is the same for both materials. As mentioned previously, the ultimate measure of wear or seal failure is lubricant leakage. It is unlikely that debris could penetrate the entire seal lip contact band and begin to drop freely into the lubricant without the seal leaking immediately or soon thereafter. Furthermore, the difference in the abrasion losses of the two seal lip materials appears to be minimal – especially in view of the dramatic difference in the break-in periods of the seals. Even with the improbable assumption that leakage does not occur immediately after dirt penetrates the entire contact band, the abrasion resistance of the filled elastomer seal lip would have to be *much* greater than that of the unfilled elastomer seal lip for an improvement in seal life comparable to the observed increase in the break-in period. We will therefore concentrate our efforts on explaining why the break-in period of the filled elastomer seal is so much longer than that of the unfilled elastomer seal.

Chapter 3

Seal Surface Characteristics

The surface properties of the mating faces in a sealing application are crucial to the performance of the seal. A logical first step in determining how the presence of fibers extends the break-in period of the track seals is to examine the effect that the fibers have on the surface characteristics of the seal lip. In this chapter, results from four different types of surface analysis are presented.

3.1 Scanning Electron Microscopy

SEM observations reveal that the surfaces of unworn filled and unfilled elastomer seal lips are remarkably different. Figure 3-1 shows SEM pictures of filled and unfilled elastomer seal lips. The unfilled elastomer seal lip appears smooth and has only a few scattered blemishes on its surface. The filled elastomer seal lip, however, appears much rougher and has numerous imperfections on its surface.

3.2 Optical Surface Roughness Measurements

A Surfascan, a three-dimensional optical non-contact surface topography measurement machine at Caterpillar, was used to measure the surface roughness of filled and unfilled elastomer seal lips. The results are displayed in Figures 3-2 and 3-3. The top portion of each figure shows a three-dimensional height map of a 750 μm by 560

Figure 3-1: SEM of Unworn Seal Lips

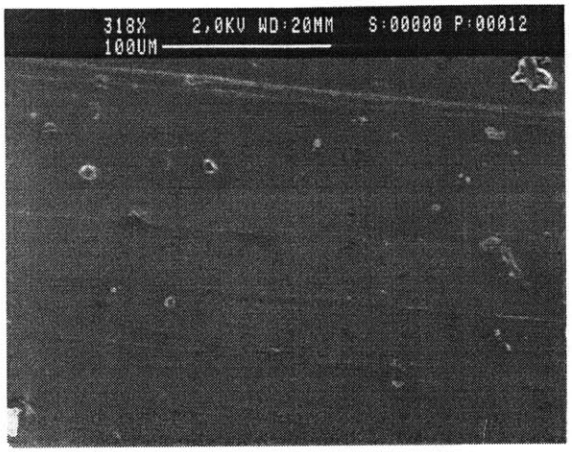

unfilled elastomer seal lip

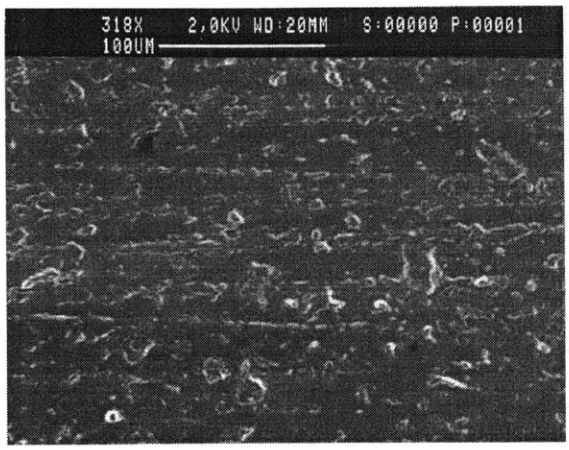

filled elastomer seal lip

μm patch on each seal lip. Qualitatively, the peaks are much higher for the filled elastomer seal lip indicating a rougher surface. The maximum height above the mean line is 8.14 μm for the filled elastomer seal lip and 4.44 μm for the unfilled elastomer seal lip. Furthermore, a statistical analysis indicates that the filled elastomer seal lip has an average surface roughness of 0.89 μm – more than twice the value of 0.41 μm of the unfilled elastomer seal lip. The bottom halves of Figures 3-2 and 3-3 show a 750 μm line segment profile of the surface topography of each seal lip. The peak to valley distance is 9.02 μm for the filled and 2.61 μm for the unfilled elastomer seal lip. Excluding the one large peak of 6.89 μm in the line profile in Figure 3-3, the peak to valley distance of the filled elastomer seal lip is 4.93 μm – still almost twice that of the unfilled elastomer seal lip. The line profiles also show the filled elastomer seal lip having a much higher average surface roughness. The average surface roughness is 0.96 μm for the filled elastomer seal lip and 0.34 μm for the unfilled elastomer seal lip.

3.3 Atomic Force Microscopy

An atomic force microscope (AFM) at the Center for Material Science and Engineering at MIT was also used to measure the surface roughness of the filled and unfilled

Figure 3-2: Surface Topography Measurements of Unfilled Elastomer Seal Lip

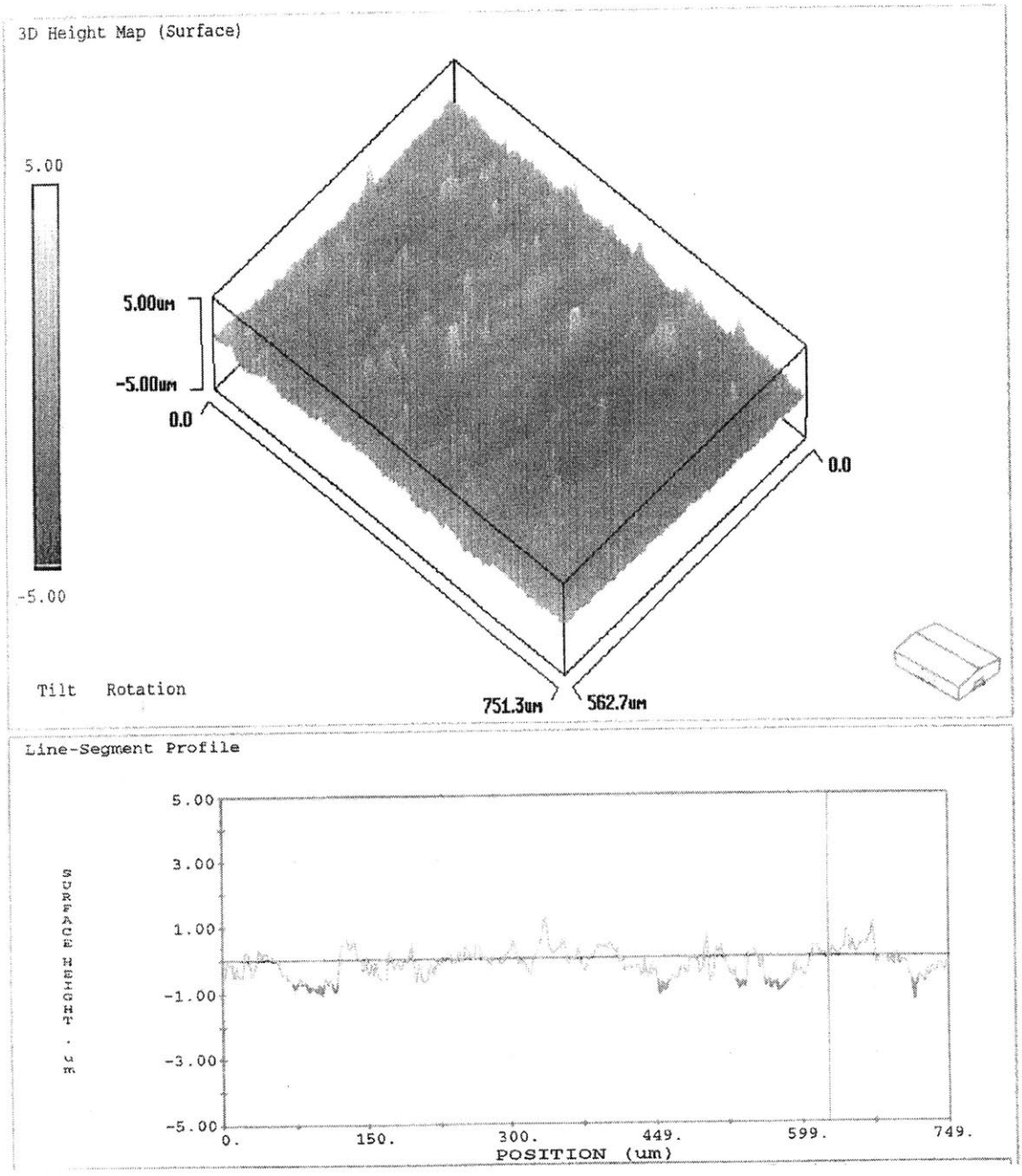

Figure 3-3: Surface Topography Measurements of Filled Elastomer Seal Lip

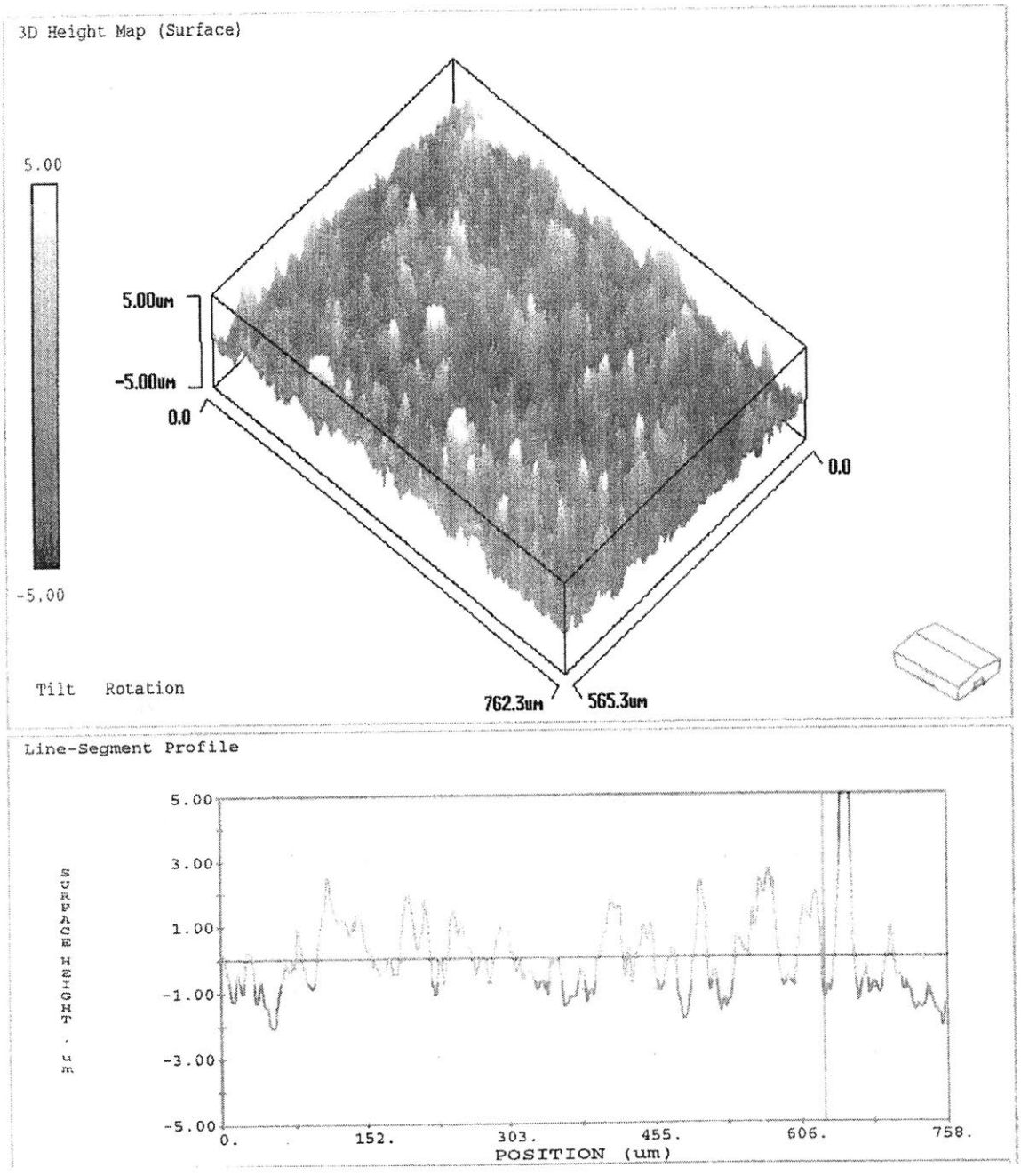

elastomer seal lips. A probe with a tip radius of 5 nm, mounted on a cantilever, scanned across the surface of the specimen. As the tip moved along, surface height variations caused the cantilever to deflect. The deflection of the cantilever was used to produce a high resolution topographic image. Numerous passes spaced 200 nm apart created a detailed map of the surface.

Figures 3-4 and 3-5 show AFM maps of unfilled and filled elastomer seal lips respectively. Each image corresponds to an area measuring 100 μm by 100 μm on the surface of the seal lip. In these images, black indicates the maximum distance below the mean and white corresponds to the maximum distance above the mean. The image for the filled elastomer seal lip has numerous black and white areas indicating deep valleys and high peaks respectively. The peak to valley distance is 5.65 μm. The image for the unfilled elastomer seal lip, however, has few black or white areas and is predominantly various shades of gray indicating a flatter, more uniform surface topography. The peak to valley distance is only 3.88 μm. Statistically, the AFM surface roughness measurements agree remarkably well with the optical surface roughness measurements. The unfilled elastomer seal lip exhibits an average surface roughness of 0.34 μm while the filled elastomer seal lip has an average roughness of 0.76 μm. Figure 3-6 shows a refined scan measuring 10 μm by 10 μm of a peak on the filled elastomer seal lip in Figure 3-5. The image in Figure 3-6 appears to be a fiber, possibly obscured by a thin layer of polyurethane, projecting from the surface of the seal lip. The white area is a maximum of 2.41 μm above the lowest point in the scan.

3.4 CCD Camera Pictures of Loaded Seals

Images from the seal wear experiments described in chapter 2 also provide valuable information about the differences in the surface characteristics of filled and unfilled elastomer seal lips. Figure 3-7 depicts the contact bands of fully loaded filled and unfilled elastomer seal lips before the abrasive slurry has been added. The white spots are air bubbles between the seal lip and the glass window. The unfilled seal

Figure 3-4: AFM Surface Roughness Measurement of Unfilled Elastomer Seal Lip

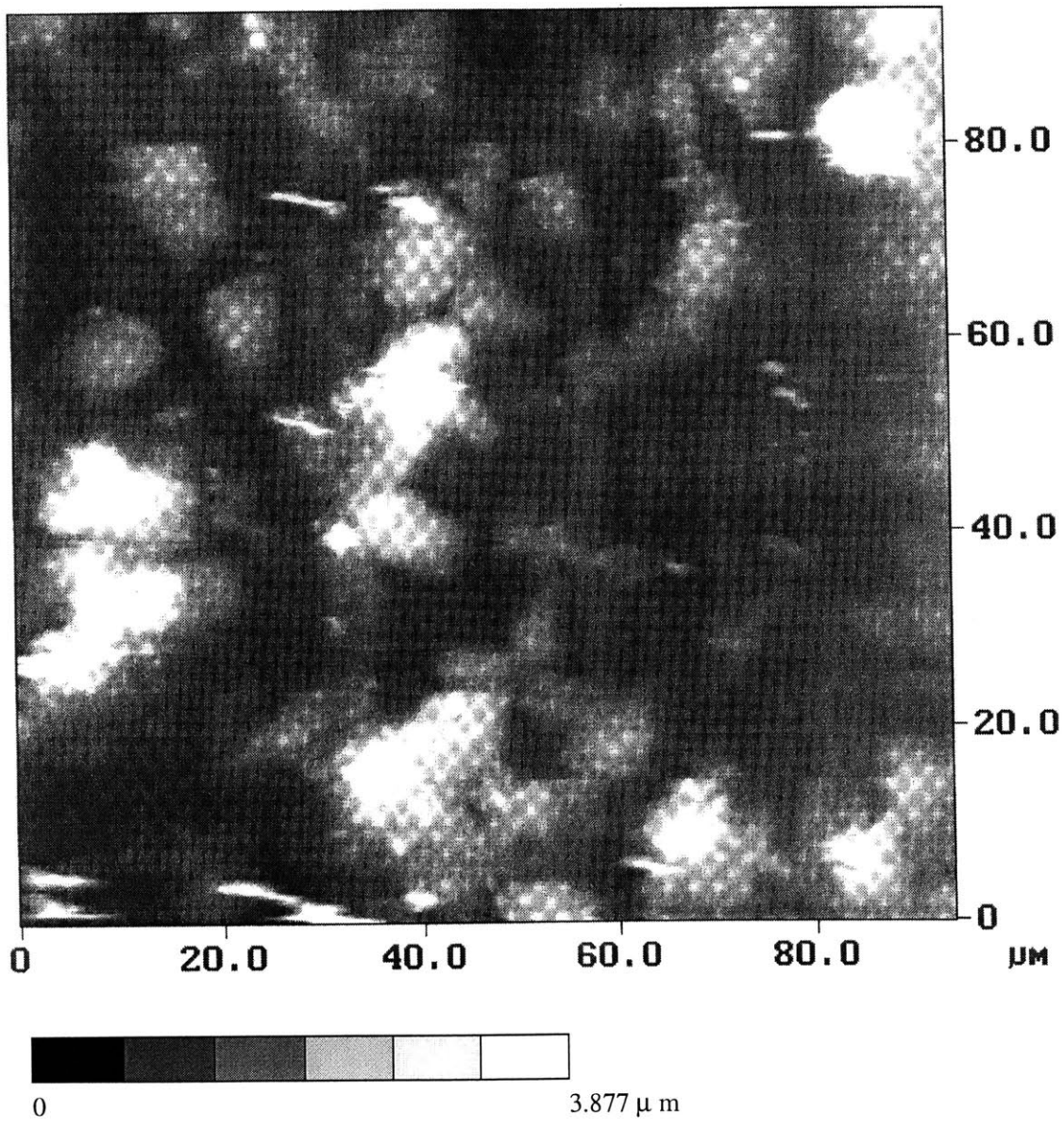

Figure 3-5: AFM Surface Roughness Measurement of Filled Elastomer Seal Lip

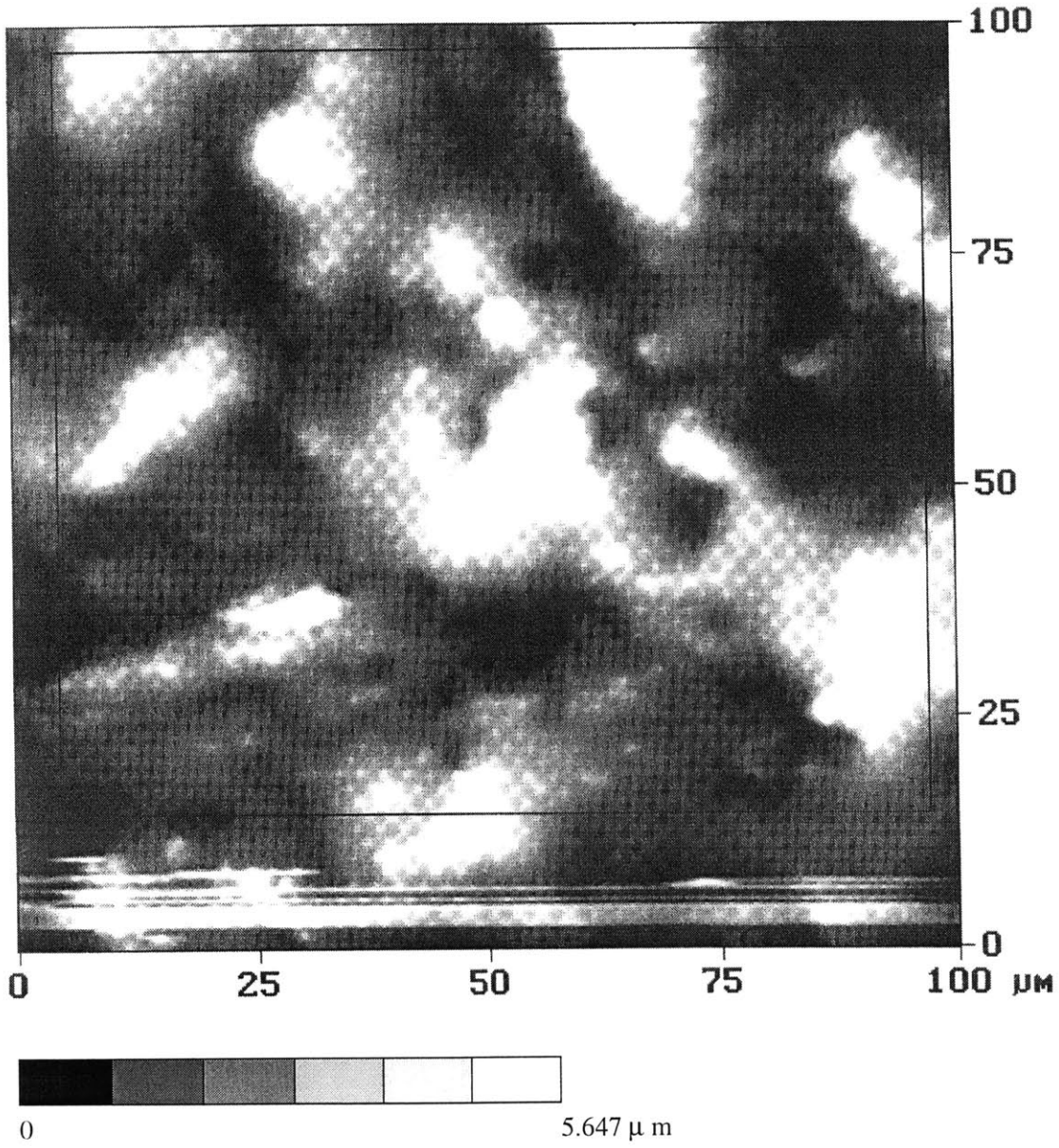

Figure 3-6: AFM of Single Fiber at Seal Lip Surface

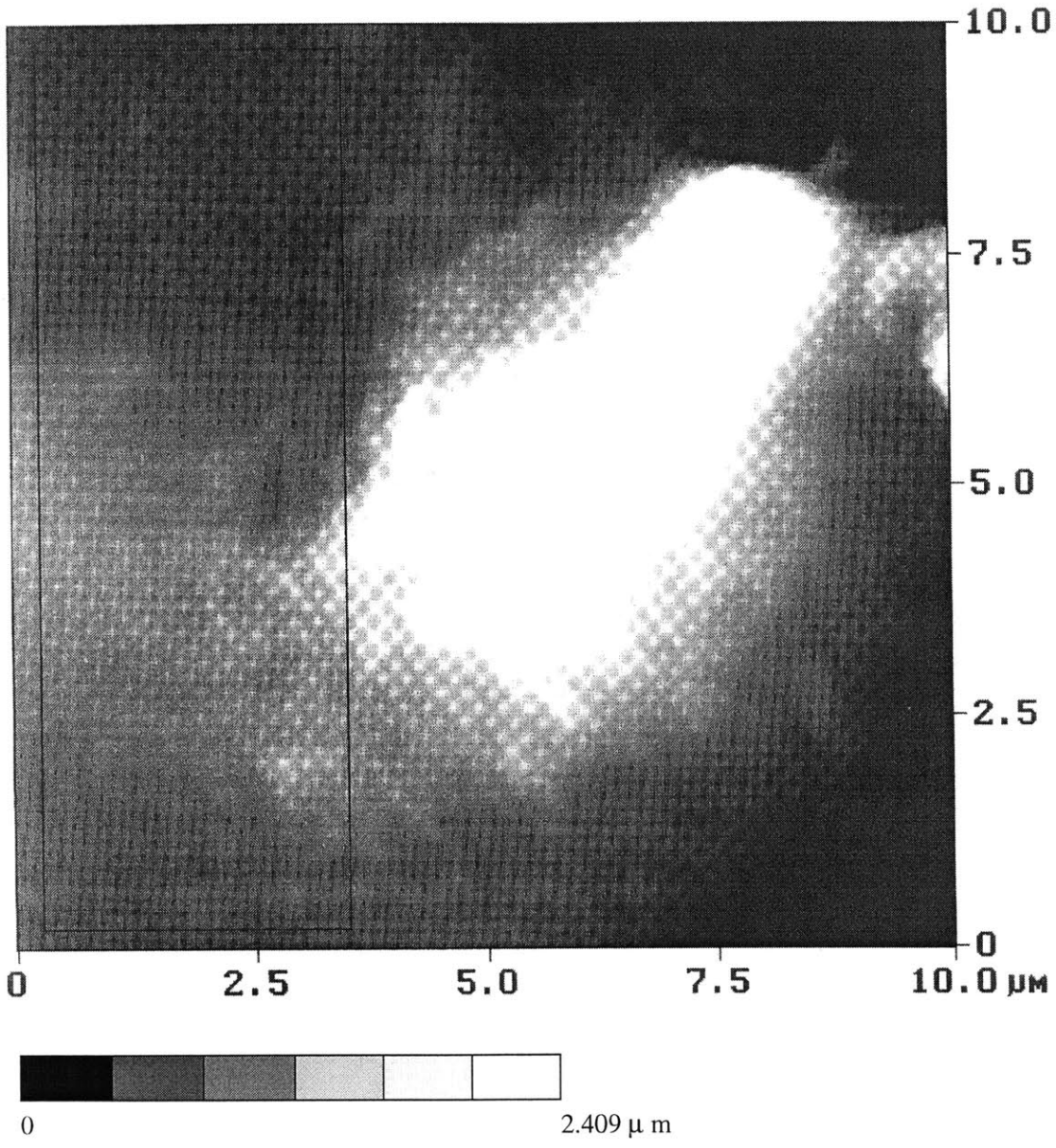

Figure 3-7: CCD Pictures of Seal Lip Contact Bands

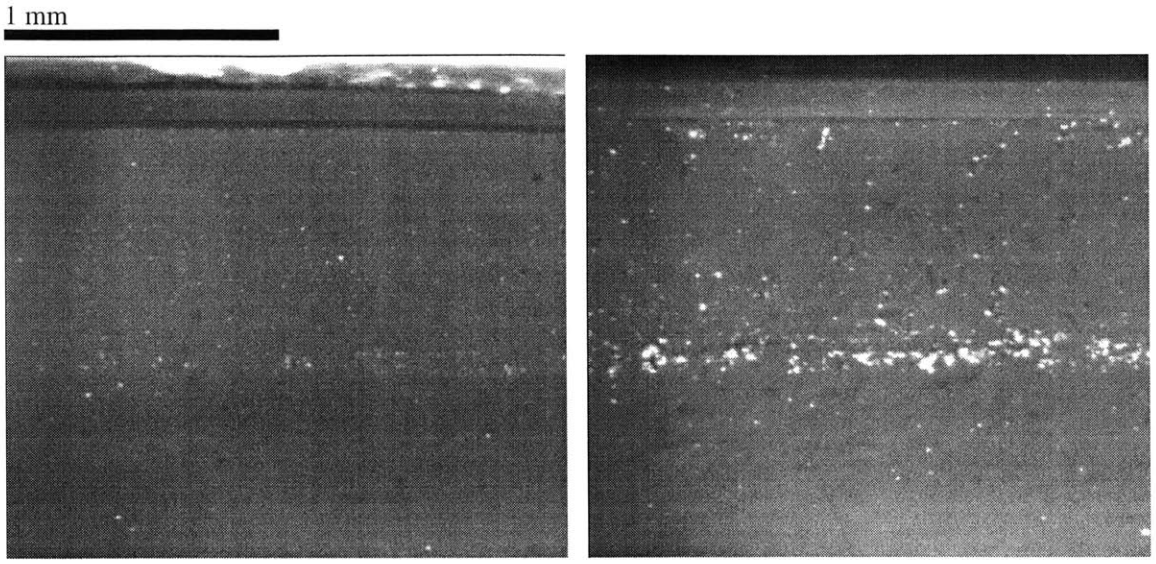

unfilled elastomer seal lip contact band

filled elastomer seal lip contact band

lip contact band is smooth and uniform with very small bubbles evenly distributed over the contact band area. The bubbles in the filled seal lip contact band are more numerous and also much larger. Furthermore, there are also numerous dark spots visible on the filled seal lip. The dark regions are approximately the same size and shape as the glass fibers in the seal lip material. Close examination reveals that the bubbles seem to be preferentially located in pairs near the tips of the dark spots.

There is always a thin film of oil between the seal and the glass window. The amount of light reflected is directly proportional to the amount of oil between the seal and the glass window. A thicker oil film therefore corresponds to a lighter image. The black spots are areas where there is less oil than in the surrounding regions. It appears that fibers near the surface of the seal lip effectively squeeze oil out of that portion of the contact band.

3.5 Conclusions

The presence of fibers clearly changes the surface characteristics of the seal lip. SEM observations show that the filled elastomer seal lip *appears* rougher than the unfilled

elastomer seal lip. Optical and AFM measurements verify that the filled elastomer seal lip is approximately twice as rough as the unfilled elastomer seal lip. The increase in surface roughness may be due to the location of the fibers. AFM and the CCD camera images indicate that fibers are present at or near the surface of the seal lip. The fibers may also affect the way the material fills the mold during the injection molding process and, as a result, alter the surface properties of the finished part.

The CCD images provide important clues regarding how the fibers affect the sealing behavior. The fibers near the surface of the seal lip deform much less than the soft elastomer and therefore bear a higher proportion of the applied load than the surrounding matrix material. As a result, the contact pressure is higher in the vicinity of the fibers. In Figure 3-7, the dark areas where the oil film thickness is smallest are due to the load bearing effect of the fibers near or at the surface of the seal lip. In chapter 6, finite element analysis will quantify this variation in the contact pressure.

Chapter 4

Micromechanical Modeling of Abrasive Wear of Unfilled Elastomers

The experimental work of the author and Ayala [6] has shown that the track seal wears only when dirt particles penetrate the contact band. The seal lip oscillates back and forth over the bushing surface with the dirt particles trapped in between. The particles cyclically deform the seal lip and eventually cause material to be removed in a fatigue fracture type process. The track seal wear process is representative of numerous applications where abrasive wear occurs. The modeling conducted in this and the following two chapters is therefore applicable in a much broader sense.

4.1 Finite Element Model Description

Micromechanical modeling of the abrasive wear of unfilled polyurethane was performed with the finite element package ABAQUS. The goal was to determine the effect that abrasive asperities have on the local stress and strain fields in the elastomer.

4.1.1 Geometry and Elements

Removing the geometry variable of the shape of the seal lip, a simple block of material is used to model a portion of the seal lip. The dirt particles and bushing surface are modeled as circular and flat rigid surfaces respectively. Figure 4-1 demonstrates how the block is compressed against the bushing and dirt particle and, in some cases, also sheared over the particle in the direction perpendicular to the compression. What is commonly referred to as a single dirt particle may also be thought to represent many particles aggregated into a cluster.

Figure 4-1: Micromechanical Modeling Schematic

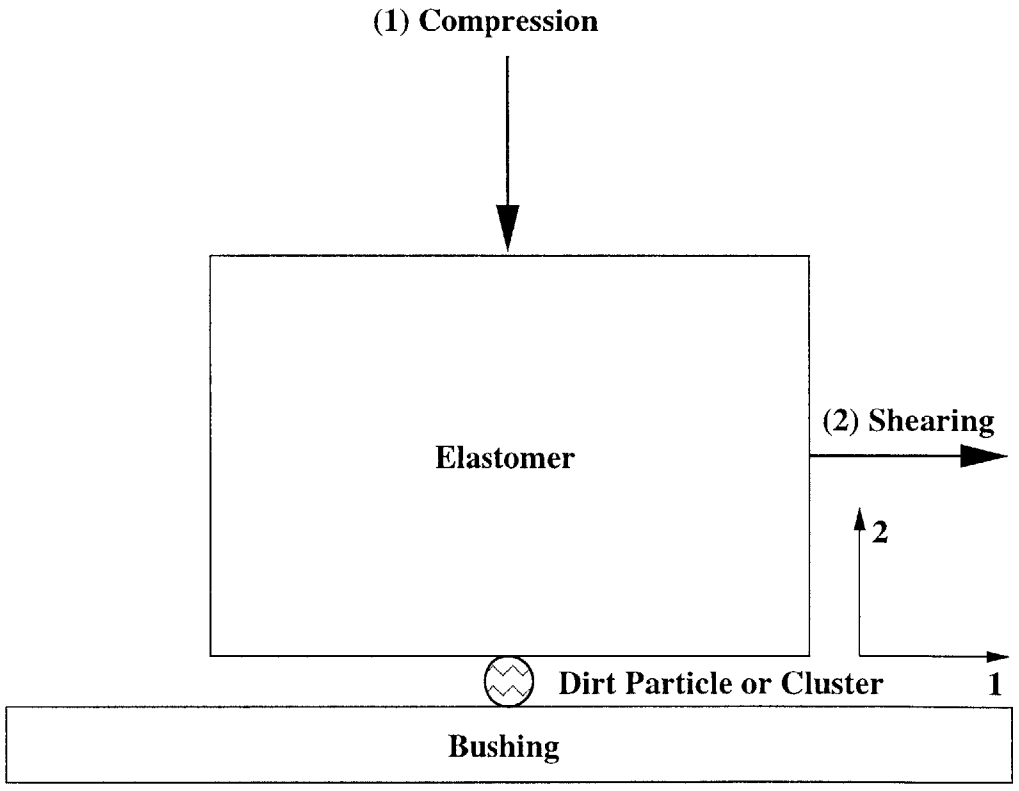

In all cases, two-dimensional plane strain quadratic hybrid elements (CPE8H) were used to model the elastomer block. Deformation is restricted to the 1-2 plane. The model geometry, therefore, effectively extends infinitely in the direction perpendicular to the plane of the page.

4.1.2 Material Models

Two constitutive models were used to model the material behavior of the matrix elastomer: the Arruda-Boyce Eight Chain model and the elastic-viscoplastic model first proposed by Boyce, Argon, and Parks [23]. The Eight Chain model, developed for large deformations of nonlinear elastic rubber materials, is rate-independent and does not capture the hysteresis effects apparent with cyclic loading. The elastic-viscoplastic model, however, does predict the strain-rate dependence and hysteresis effects exhibited by all elastomeric materials.

Arruda-Boyce Eight Chain Model

The hyperelastic Arruda-Boyce Eight Chain model [7], is based on an Eight Chain representation of the underlying macromolecular network structure of the polymer. Non-Gaussian chains extend from the center of a unit cube to each of the cube's eight corners as shown in Figure 4-2. The initial chain length from random walk

Figure 4-2: Eight-Chain Model Geometry [7]

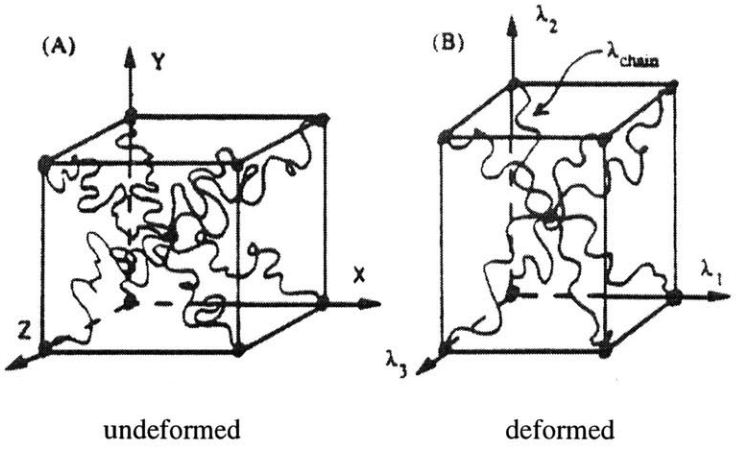

considerations is given by

$$r_0 = \sqrt{N}l, \tag{4.1}$$

where N is the number of statistical rigid links of length l between crosslink sites. The entropy of each chain in the network is described as a function of current chain

length by Langevin chain statistics. The deformed length of each chain is calculated from the geometry of the network and the applied principal global stretches, λ_1, λ_2, and λ_3, as

$$r_{chain} = \frac{1}{\sqrt{3}}\sqrt{N}l(\lambda_1^2 + \lambda_2^2 + \lambda_3^2)^{1/2}. \tag{4.2}$$

The strain energy can be derived from the entropy change due to chain stretching as

$$W = nk\Theta N\left(\frac{r_{chain}}{Nl}\beta + ln\frac{\beta}{\sinh\beta}\right) - \Theta c\prime, \tag{4.3}$$

where n is the the chain density, $c\prime$ is a constant, k is Boltzmann's constant, and β is the inverse Langevin function, $\mathcal{L}^{-1}[r_{chain}/Nl]$, for the Langevin function $\mathcal{L}[\beta] = \coth\beta - (1/\beta)$. Differentiation of the strain energy function leads to the stress-stretch relationship

$$\sigma_1 - \sigma_2 = \frac{nk\Theta}{3}\sqrt{N}\mathcal{L}^{-1}\left[\frac{\lambda_{chain}}{\sqrt{N}}\right]\frac{(\lambda_1^2 - \lambda_2^2)}{\lambda_{chain}}, \tag{4.4}$$

where the chain stretch, $\lambda_{chain} = r_{chain}/r_0$ is given by

$$\lambda_{chain} = \frac{1}{\sqrt{3}}(\lambda_1^2 + \lambda_2^2 + \lambda_3^2)^{1/2}. \tag{4.5}$$

Since the stretch in each chain is the same, the model is equivalent to averaging the response of a single chain over eight different orientations.

Elastic-Viscoplastic Model

The elastic-viscoplastic constitutive model [23, 24] was developed to model the behavior of glassy polymers. In one dimension, Figure 4-3 shows how the the model represents the material as a linear elastic spring in series with a nonlinear hardening spring and viscoplastic dashpot in parallel. The linear elastic spring provides the initial stiffness of the material. Once yielding occurs, the dashpot activates and provides the softening behavior. At large strains, the hardening spring takes effect.

The nonlinear spring and dashpot represent barriers to plastic deformation. The viscous element represents the Argon equation for the plastic strain rate, $\dot{\gamma}$, that

Figure 4-3: One-Dimensional Representation of the Elastic-Viscoplastic Model

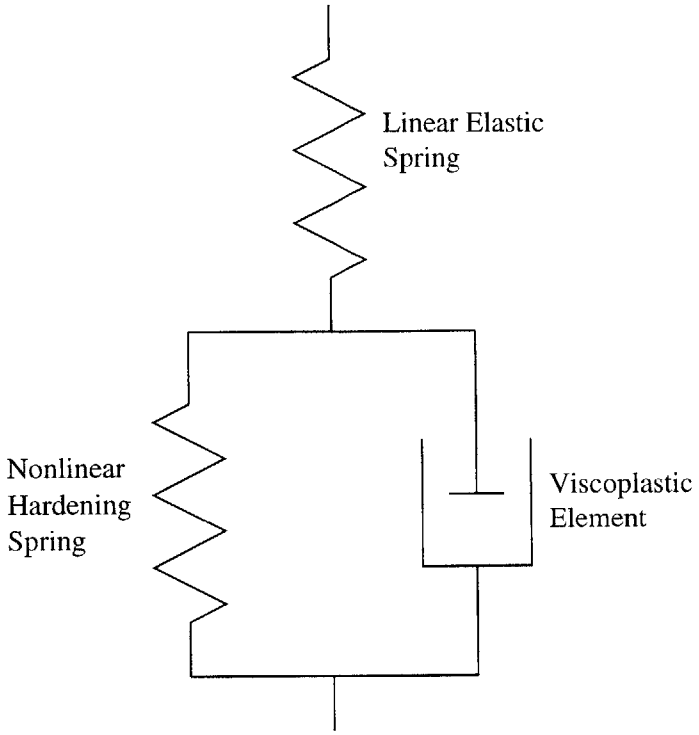

occurs once the isotropic resistance to chain segment rotation has been overcome:

$$\dot{\gamma} = \dot{\gamma}_0 exp\left[-\frac{As}{k\theta}\left\{1-\left(\frac{\tau}{s}\right)^{5/6}\right\}\right], \tag{4.6}$$

where $\dot{\gamma}_0$ is the pre-exponential factor proportional to the attempt frequency, s is the athermal shear strength, As is the zero stress level activation energy, τ is the effective equivalent shear strength, k is Boltzmann's constant, and θ is the absolute temperature. The athermal shear strength, s, is defined as $0.077\mu/(1-\nu)$ where μ is the elastic shear modulus and ν is Poisson's ratio.

The effective equivalent shear strength, τ, is found from the deviatoric part of the tensorial difference between the Cauchy stress, $\mathbf{T}$, and the convected back stress, $\mathbf{B}$, on the nonlinear spring element:

$$\tau = \frac{1}{\sqrt{2}}\left(\mathbf{T}^{*\prime}\mathbf{T}^{*\prime}\right), \tag{4.7}$$

where

$$\mathbf{T}^{\star} = \mathbf{T} - \frac{1}{J}\mathbf{F}^{e}\mathbf{B}\mathbf{F}^{eT}. \tag{4.8}$$

$\mathbf{T}^{*}$ is the portion of the total stress that continues to activate plastic flow. The nonlinear spring element represents the anisotropic resistance to chain alignment in the direction of the applied stress which must be subtracted from the total stress. The nonlinear spring element can be modeled by any classical hyperelastic model. In this case, as suggested by Arruda and Boyce [24] themselves, the Arruda-Boyce Eight Chain model is used to model this second barrier to plastic deformation. The components of the back stress come from equation 4.4 and have the form

$$B_i = \frac{nk\Theta}{3}\sqrt{N}\mathcal{L}^{-1}\left[\frac{\Lambda^{P}_{chain}}{\sqrt{N}}\right]\frac{\Lambda_i^{P2} - \frac{1}{3}I_1}{\Lambda^{P}_{chain}}, \tag{4.9}$$

where $I_1 = (\Lambda_1^{P2} + \Lambda_2^{P2} + \Lambda_3^{P2})$ is the first principal invariant of the stretches, $\Lambda^{P}_{chain} = (1/\sqrt{3})I_1^{1/2}$ is the plastic stretch on a chain, and Λ_i^{P} are the principal applied plastic stretches.

Determining Material Parameters

Testing was done on an Instron 1350 servohydraulic testing machine. Circular specimens 14.3 mm in diameter were machined from 3.2 mm thick plaques of the unfilled polyurethane. Two such specimens were roughened with fine grit sandpaper to prevent slippage and stacked one on top of the other. Sheets of teflon were placed between the specimens and the Instron grips to lubricate the interface and insure uniform deformation. Tests were conducted at room temperature and at a constant strain rate of -0.01 s^{-1} to a final strain of -1.2.

The Eight Chain model requires only two material parameters, an initial or "rubbery" modulus CR and a chain locking stretch λ_{L}. CR is defined as the familiar quantity $nk\Theta$ while λ_{L} is given by

$$\lambda_{\mathrm{L}} = \frac{r_{\mathrm{L}}}{r_0} = \sqrt{N}, \tag{4.10}$$

where $r_L = lN$ is the fully extended chain length. CR and λ_L can easily be determined from the results of a uniaxial compression test.

Figure 4-4 shows a representative stress-strain curve for the uniaxial compression of unfilled polyurethane. The material exhibits an initial stiff response, softens rather

Figure 4-4: Arruda-Boyce Eight Chain Model Prediction for Uniaxial Compression of Unfilled Polyurethane

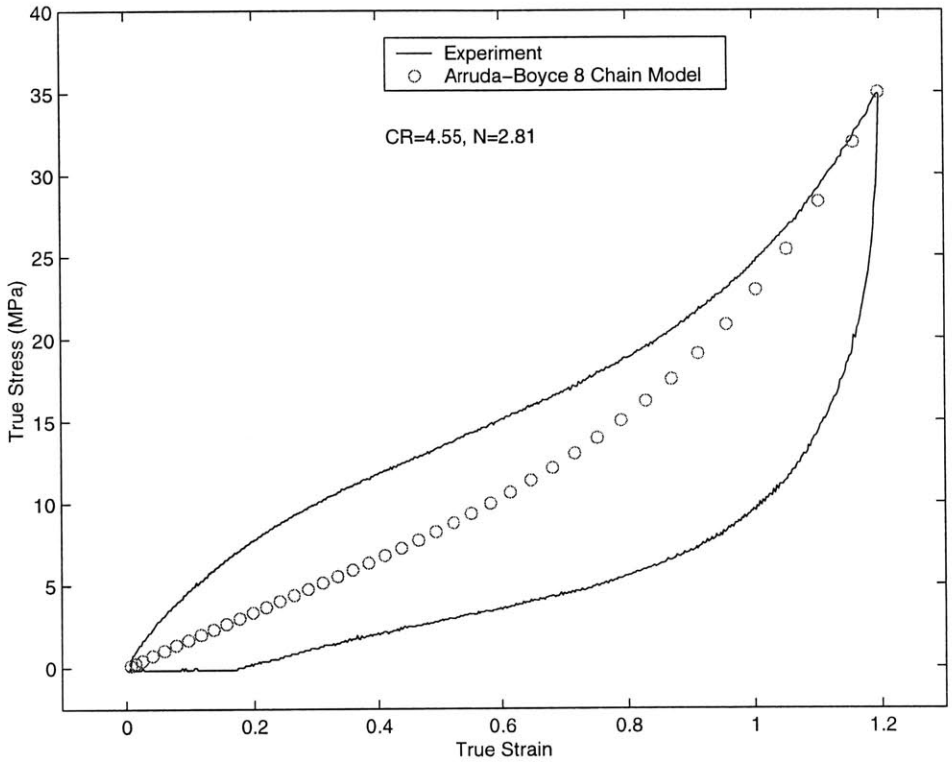

quickly, and finally hardens at high strains. Loading and unloading occur along the same curve. Fitting the Eight Chain model to this stress-strain curve, we find CR to be 4.55 MPa and λ_L to be 1.675. These values are used for the unfilled polyurethane in the majority of the subsequent finite element modeling.

There are seven material parameters required for the elastic-viscoplastic model: E and ν for the initial linear elastic behavior, CR and λ_L for the nonlinear spring, and s, As, and $\dot{\gamma}$ for the viscoplastic element. From the uniaxial compression data in Figure 4-4, the following values were determined: E = 47 MPa, ν = 0.48, CR = 3.75 MPa, λ_L = 1.16, ν = 0.48 and s = 5.8. Calculating As and $\dot{\gamma}$ requires uniaxial

compression data at two different strain rates. Values of As $= 1.89 \times 10^{-19} J$ and $\dot{\gamma} = 1.4365 s^{-1}$, determined by Yeh [25] for the same unfilled polyurethane, were used. The fit is shown in Figure 4-5.

Figure 4-5: Elastic-Plastic Model Prediction for Uniaxial Compression of Unfilled Polyurethane

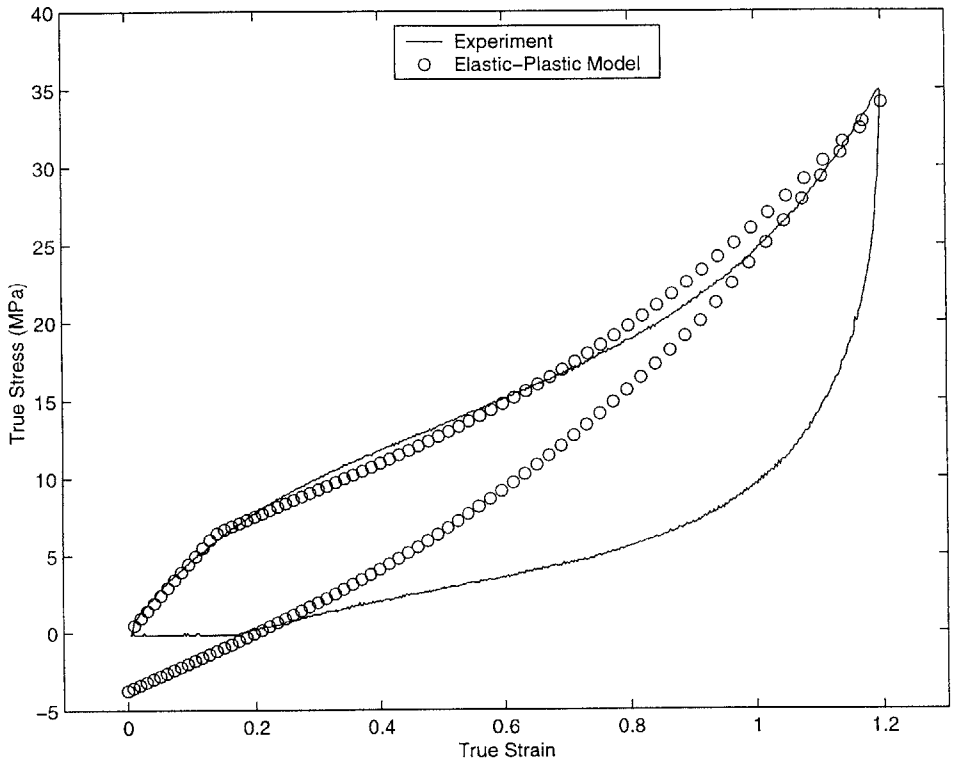

The elastic-viscoplastic model is clearly superior to the Eight Chain model. Most importantly, it captures the loading behavior exceptionally well. Both the initial stiffness of the material and the overall shape of the loading curve are predicted quite closely. In addition, while its prediction of the unloading behavior may not be particularly accurate, the elastic-viscoplastic model, unlike the Eight Chain model, does at least exhibit hysteresis. It should be noted that the material constants were chosen to best represent the loading behavior. An improvement in the unloading behavior prediction can only be made at the expense of a less accurate loading behavior prediction. Finally, the model has the ability to account for the strain rate and temperature dependence of the material. Despite its power, the elastic-viscoplastic model was used

sparingly because of its computational costs.

Modeling the Abrasive Particle and Bushing

In the track seal application, the abrasive particles and steel bushing surface are much harder than the polyurethane seal lip. While the Young's modulus of silica, the hardest mineral in the Caterpillar standard mud mix, can be as high as 69 GPa [25], and steel has a modulus of 207 GPa, the polyurethane has an approximate modulus of only 25 MPa. With moduli several orders of magnitude greater than the modulus of the polyurethane, the particle and bushing are therefore modeled as rigid surfaces. The bushing is modeled as planar, and the particles are modeled as circular.

4.1.3 Boundary Conditions and Loading

As shown in Figure 4-1, the loading of the polyurethane block occurs in two steps. A multi-point constraint forces the entire top row of nodes to displace the same distance in the 2-direction as one of the upper corner nodes. In the first step, a displacement boundary condition moves the corner node in the negative 2-direction compressing the block against the particle and bushing surface. An additional multi-point constraint forces the nodes on the left and right sides of the block to displace equally in the 1-direction. The sides are constrained to remain vertical so that the material block represents a repeatable volume element. In the second step, the top row of nodes is displaced in the 2-direction shearing the block over the particle and bushing surface. In all simulations, the particle and bushing surface are fixed in space.

4.2 Results of Unfilled Elastomer Simulations

Modeling of the abrasive wear of unfilled polyurethane is presented in this section. The particles' effect on the local stress and strain field in the elastomer is investigated. The results of compression only and compression followed by shearing simulations both with and without friction are shown. Results with the Arruda-Boyce Eight Chain and elastic-viscoplastic material models are compared.

Figure 4-6: Unfilled Elastomer Mesh – Compressed

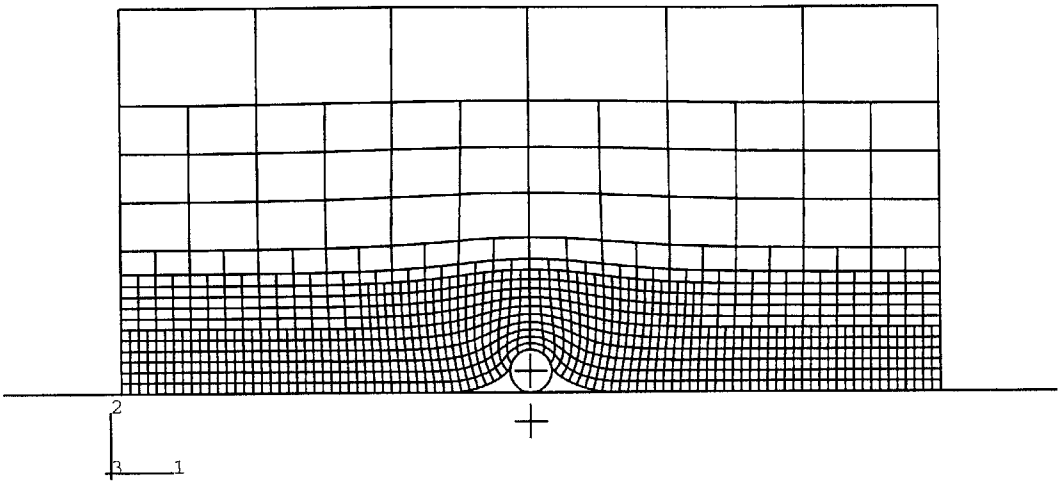

In all simulations in this chapter, the abrasive particle is 30 μm in diameter, and the block of polyurethane is 320 μm tall. The top row of nodes is displaced 78 μm in the negative 2-direction, a displacement corresponding to 15% compression in the absence of the dirt particle. It is important to note that, as long as the elastomer block is much larger than the particle, all lengths are arbitrary. Not until fibers are introduced into the elastomer does the particle size become meaningful. Unless otherwise noted, the material has been modeled with the Arruda-Boyce Eight Chain model.

4.2.1 Effect of Particle on Local Stress and Strain Fields in the Elastomer

Figure 4-6 shows the block of unfilled polyurethane compressed over the dirt particle. There is no friction between either the elastomer and the particle or the elastomer and the rigid surface. Figure 4-7 shows a close-up view of the particle and the surrounding elastomer. The material has deformed around the particle but left small gaps on either side.

Figures 4-8 and 4-9 show the stress and strain contour plots in the direction of compression. The maximum compressive stress, -33.4 MPa, occurs directly over the

Figure 4-7: Deformed Unfilled Elastomer Mesh – Zoomed in Around Particle

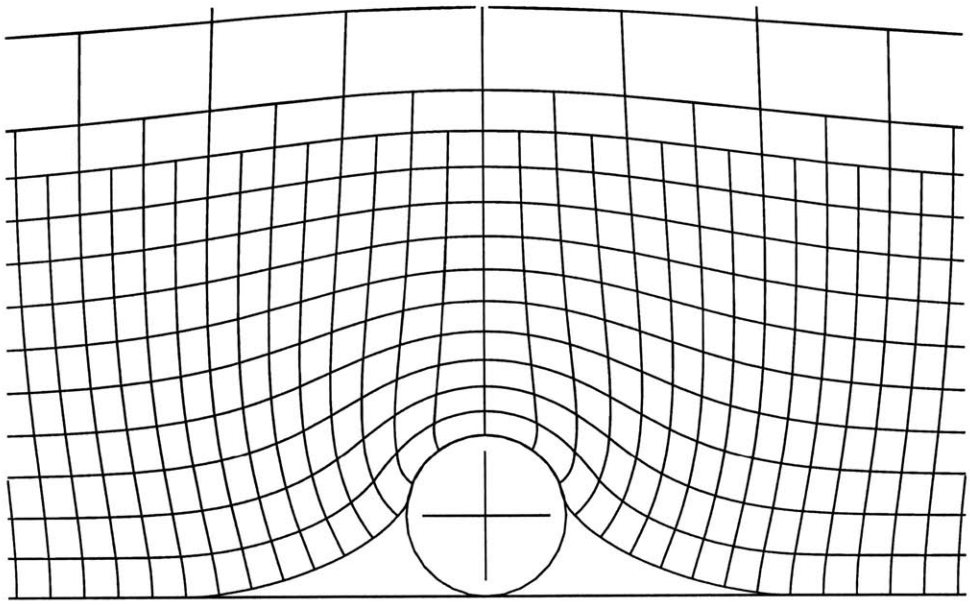

Figure 4-8: 2-Direction Stress Contour Plot

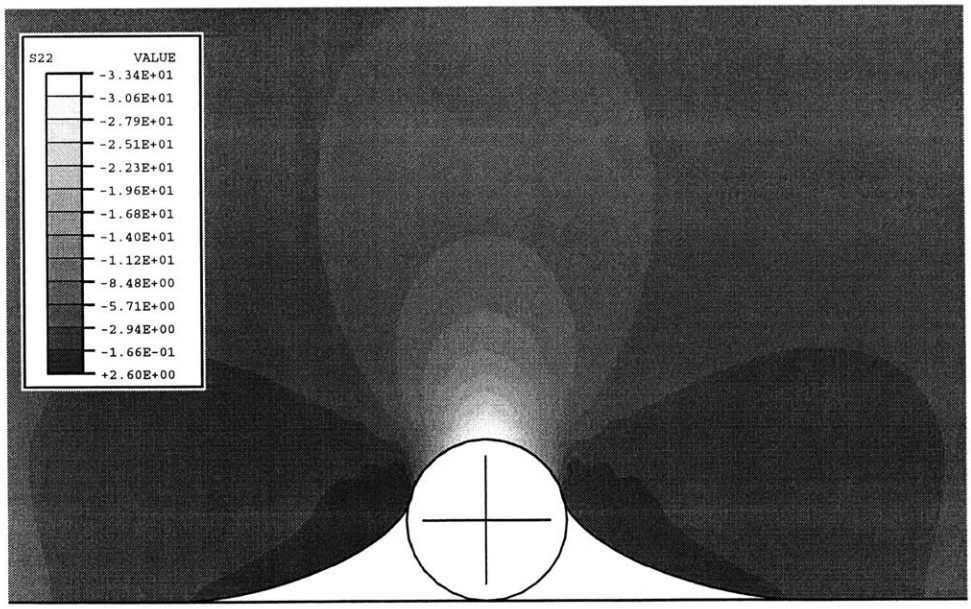

Figure 4-9: 2-Direction Strain Contour Plot

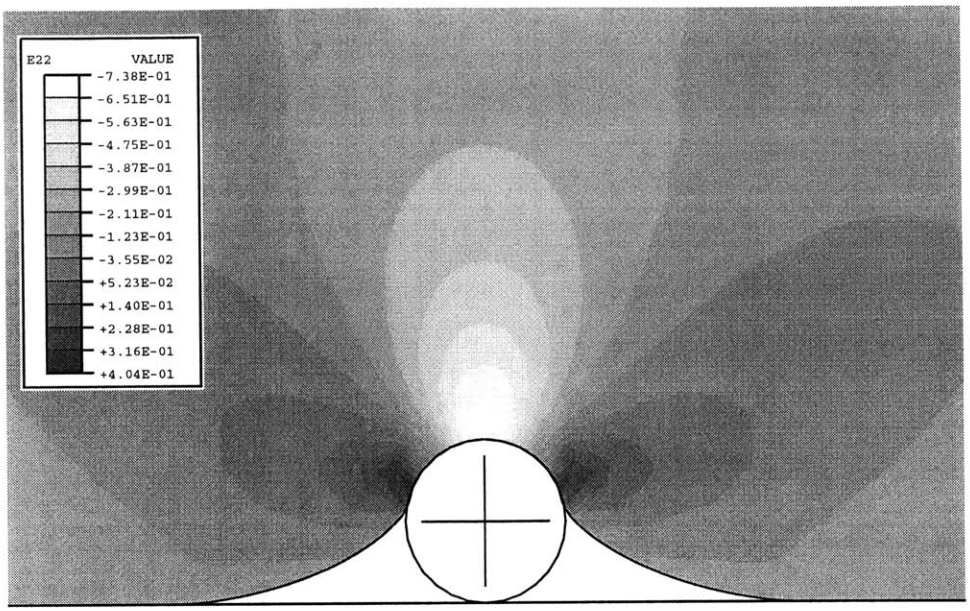

particle. Consistent with St. Venant's principle, the compressive stress decreases with vertical distance from the top of the particle until it reaches approximately -4 MPa, the value in the absence of the particle, 100 μm from the particle. Regions of tensile stress as high as 2.6 MPa exist near at surface of the elastomer on either side of the particle. Similarly, the maximum compressive strain of -0.74 occurs directly above the particle. Tensile strains exist on either side of the particle and reach a maximum of 0.40 at the particle surface just above the centerline of the particle.

Figures 4-10 and 4-11 show the stress and strain contour plots in the 1-direction. The maximum compressive stress, -13.4 MPa, occurs at the surface of the elastomer on either side of the particle approximately 45 degrees above the particle centerline. The maximum tensile stress, 9.76 MPa, is found directly above the particle at a distance of approximately 1/6 particle diameter. The compressive and tensile stress concentrations exist with diminishing magnitude for approximately two particle diameters from the location of their maximum values. Regions of significant tensile stress are also seen where the elastomer lifts up from the bushing surface to deform around the particle. The magnitude at the elastomer surface is as high as 6.20 MPa.

Figure 4-10: 1-Direction Stress Contour Plot

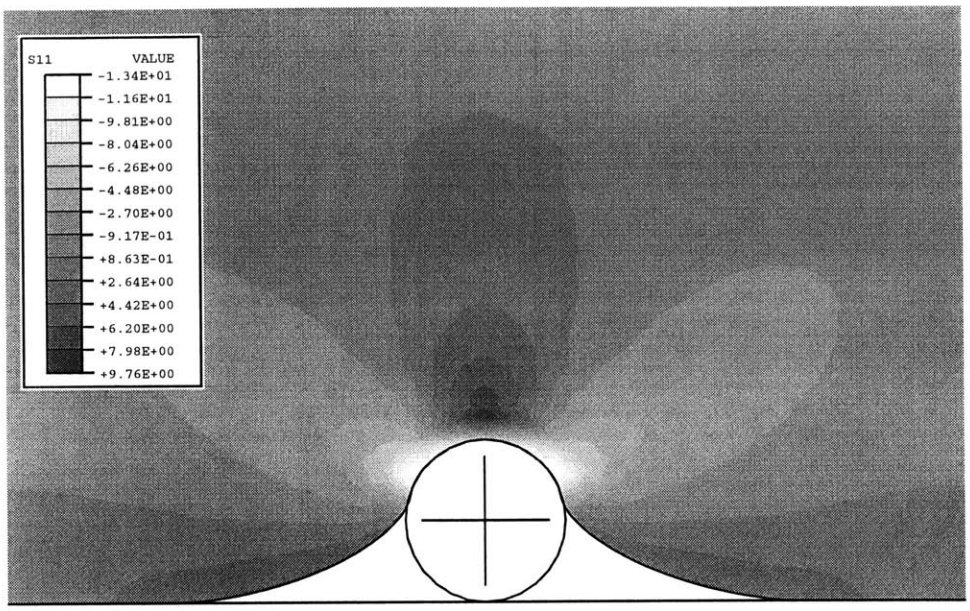

Figure 4-11: 1-Direction Strain Contour Plot

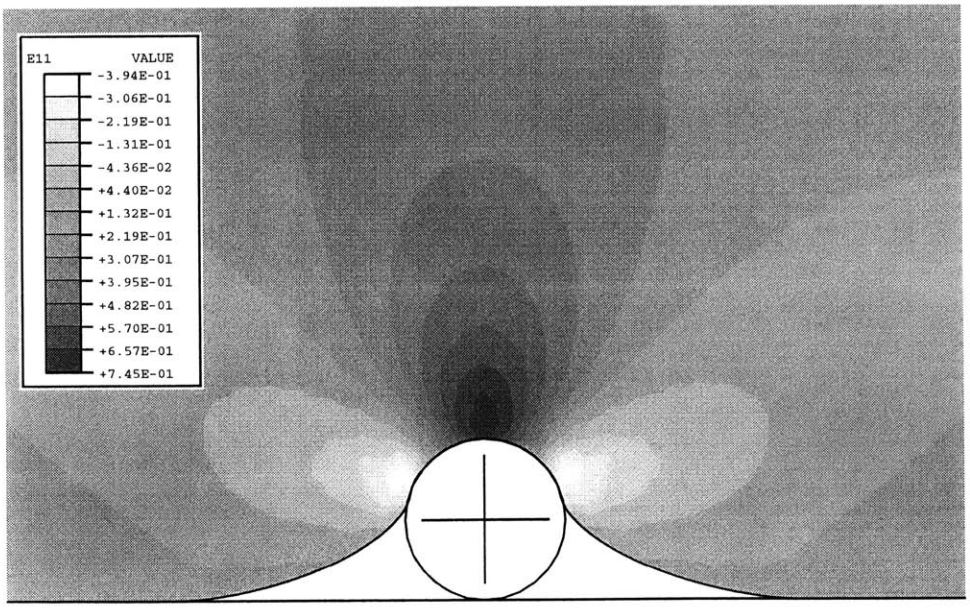

Figure 4-12: Maximum Principal Stress Contour Plot

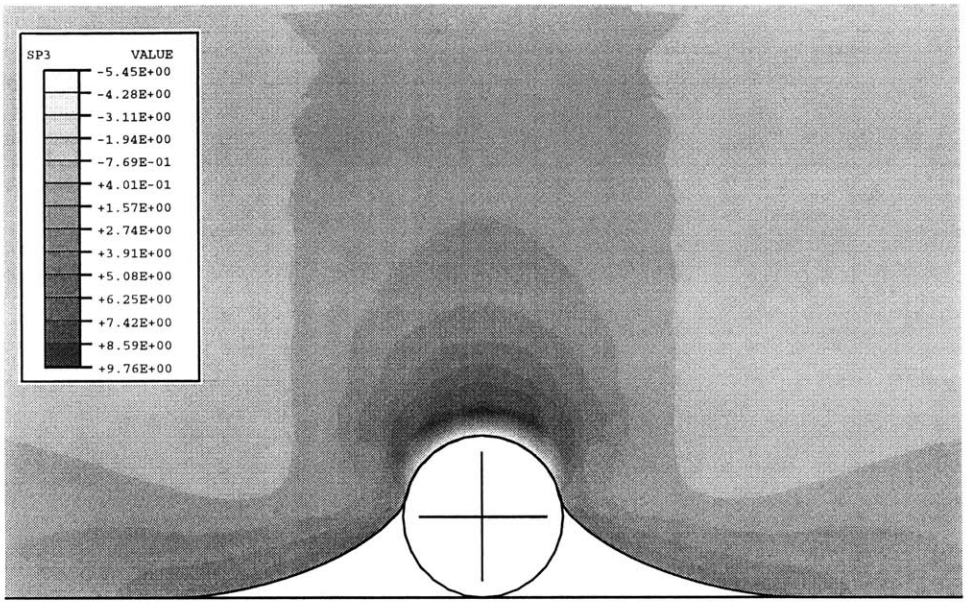

The 1-direction strain plot exhibits a similar pattern but with further reaching effects. The maximum compressive strain is -0.39 on either side of the particle, and the maximum tensile strain is 0.75 directly over the particle.

4.2.2 Effect of Particle on Maximum Tensile Stress in the Elastomer

On a microscopic scale, the abrasive wear of elastomers is a fracture process. Deformations caused by abrasive asperities create high tensile stresses in the elastomer and, when the cohesive strength of the material is reached, microcracking occurs. The effect that the particle has on the maximum tensile stress reached in the elastomer is therefore investigated. The maximum tensile stress, irrespective of direction, is also known as the maximum principal stress. The maximum principal stress in the elastomer will henceforth become a standard measure used to compare different materials and models.

Figure 4-12 shows a contour plot of the maximum principal stresses in the elastomer around the particle. The largest tensile stress, 9.76 MPa, occurs directly above

Figure 4-13: Deformed Unfilled Elastomer Mesh with Friction

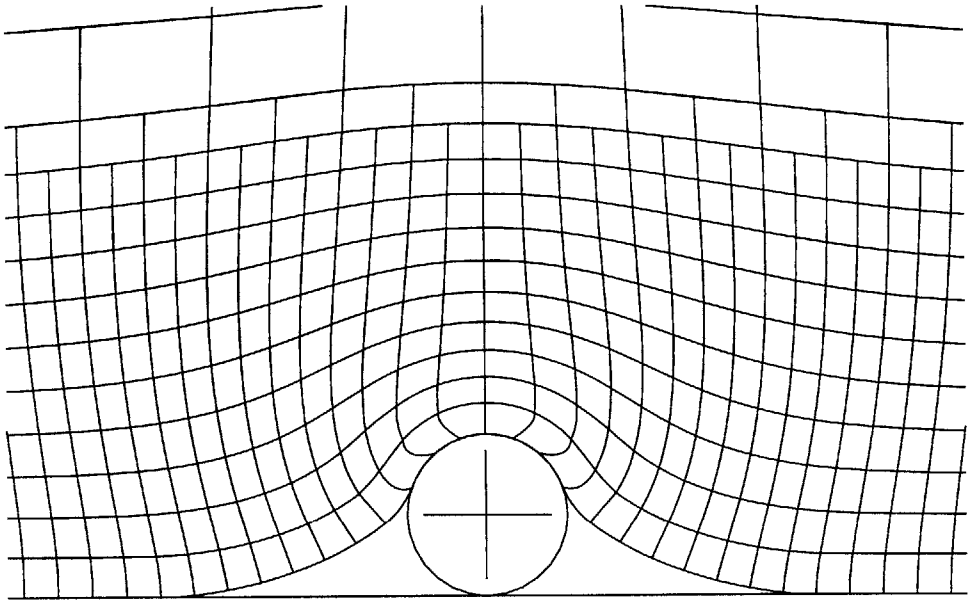

the center of the particle at a distance of approximately 1/6 particle diameter. Referencing Figure 4-10, we see that the maximum principal stress is clearly in the 1-direction. Tensile stresses exist, in at least one direction, everywhere in the vicinity of the particle except *immediately* above the particle where the maximum principal stress is as small as -5.45 MPa.

4.2.3 Compression with Friction

Figure 4-13 shows the results of the compression simulation with a coefficient of friction of 0.4 between the elastomer and the particle. Friction clearly restricts the flow of material away from the particle. The contour plot in Figure 4-14 shows that including friction increases the maximum tensile stress in the polyurethane to 14.4 MPa. The maximum tensile stress now occurs at the sides of the particle. In addition, there is a more extensive region directly above the particle where the stresses are compressive in all directions.

Figure 4-14: Maximum Principal Stress with Friction Contour Plot

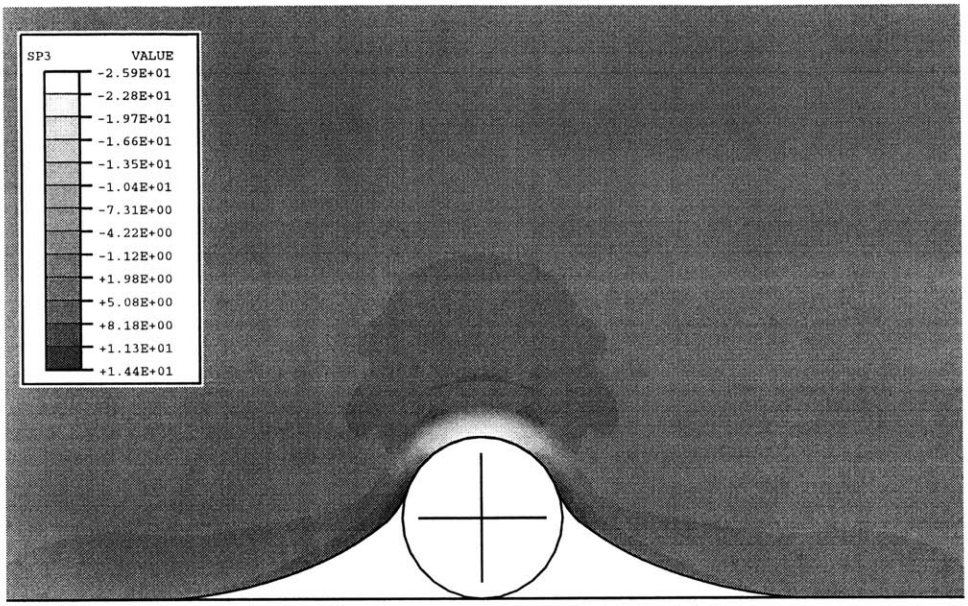

4.2.4 Compression and Shearing with Friction

Figure 4-15 shows the effect of, after compression, shearing the elastomer block in the positive 1-direction over the dirt particle. As Schallamach [21] and Barquins [17] reported, compression behind and tension in front of the particle produce an asymmetric contact area. The material bunches up on the left hand side of the particle and starts to fold over and buckle just as Schallamach observed. This behavior is consistent with several investigators' proposed wear mechanisms. Once the initial micron size pits or microcracks that Gent [22] and Fukahori and Yamazaki [19] discuss form, large pieces of the elastomer may be removed during this folding over period producing the characteristic ridge pattern. We see in Figure 4-16 that the shearing action further increases the maximum tensile stress in the polyurethane. As Schallamach [21] observed, the maximum tensile stress now occurs on the side of the particle in the direction of material flow and has increased to 62.9 MPa by the end of the simulation. This agrees perfectly with the stick-slip model proposed by Fukahori and Yamazaki. Microcracks that form during the slip phase propagate in the region of high tensile stress that forms during this, the stick phase.

Figure 4-15: Shearing Elastomer Block Over Particle with Friction

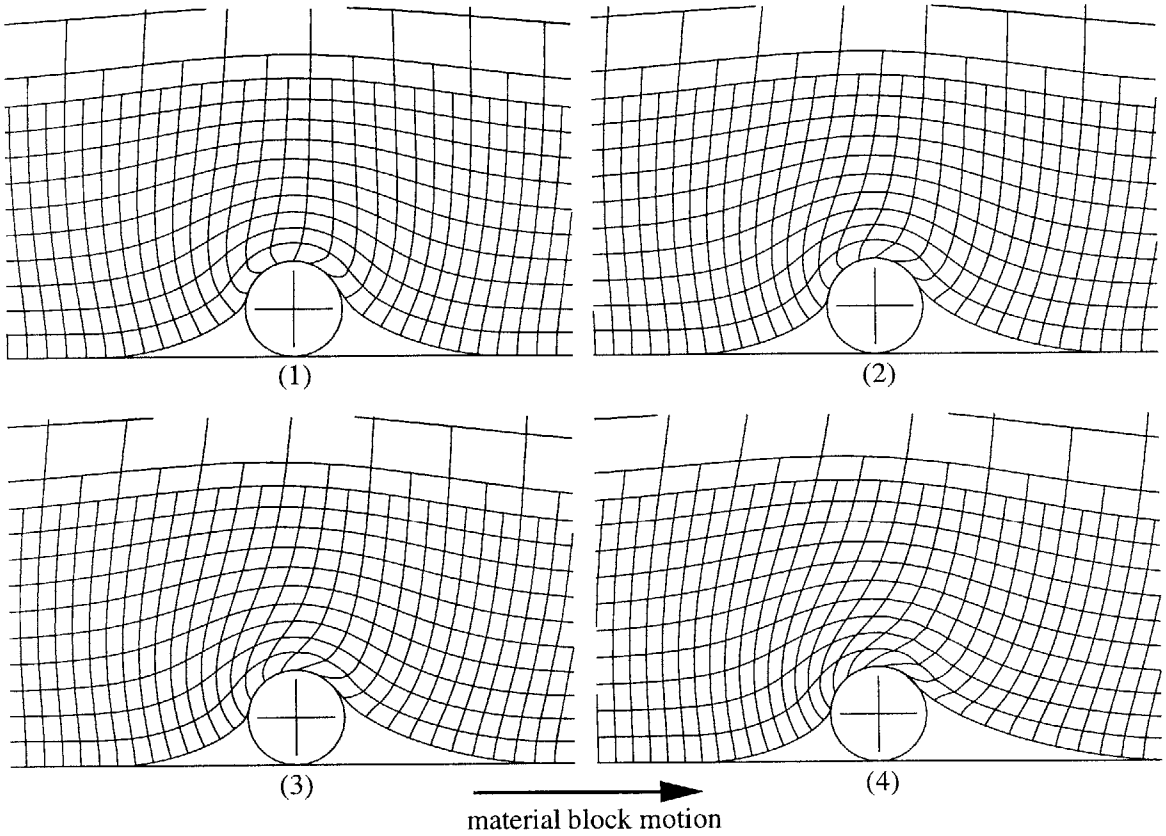

4.2.5 Comparison of Arruda-Boyce Eight Chain and Elastic-Viscoplastic Material Models

The frictionless compression simulation was also run with the elastic-viscoplastic constitutive model in order to compare the results with those of the Eight Chain model. The elastic-viscoplastic model was implemented into ABAQUS via a user material written by M.C. Boyce [24]. Because of convergence problems with the elastic-viscoplastic model, for comparative purposes, the simulations with both models were run to a displacement of only 41 μm.

Figures 4-17 and 4-18 show the deformed meshes for the two simulations. In Figure 4-18, the deformation of the elastomer modeled with the elastic-viscoplastic model is highly concentrated around the particle. The elastomer has enveloped nearly half of the circumference of the particle, and the elements close to the particle are

Figure 4-16: Maximum Principal Stress during Shearing Contour Plots

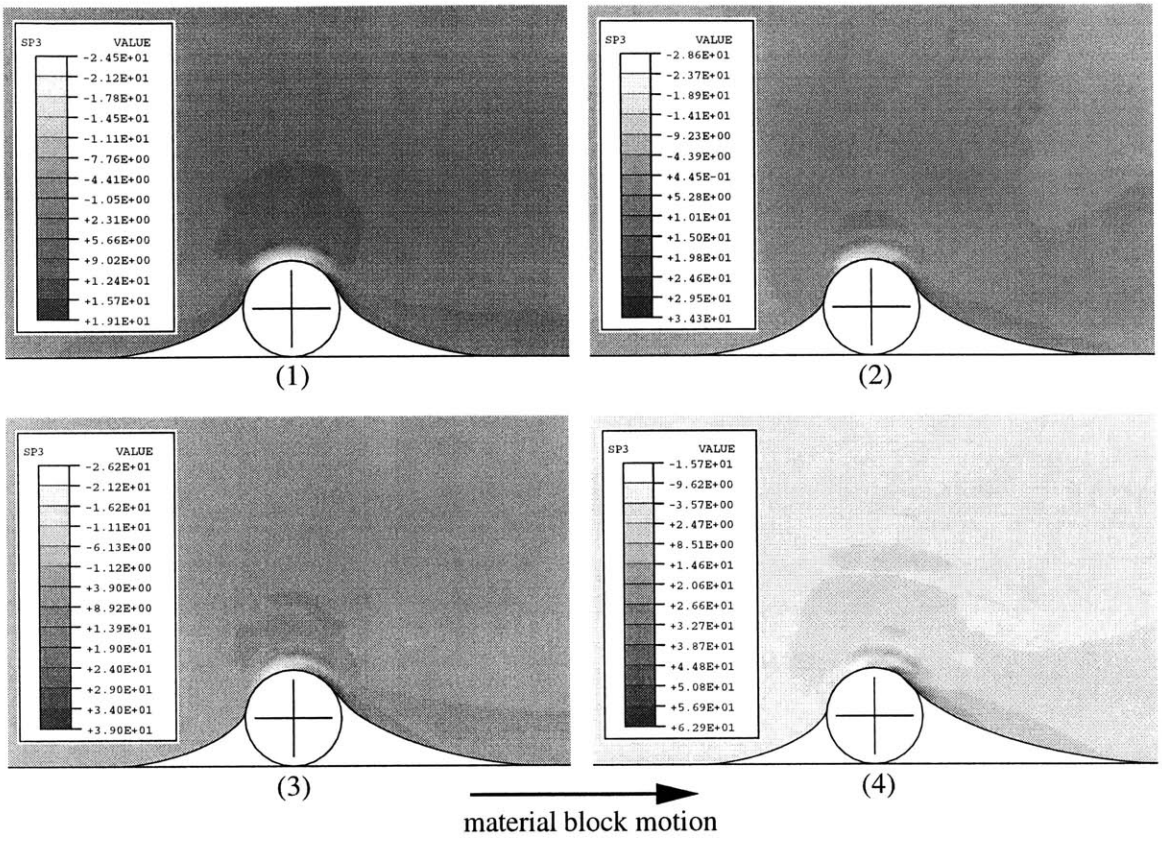

Figure 4-17: Deformed Unfilled Polyurethane Mesh with Eight Chain Model

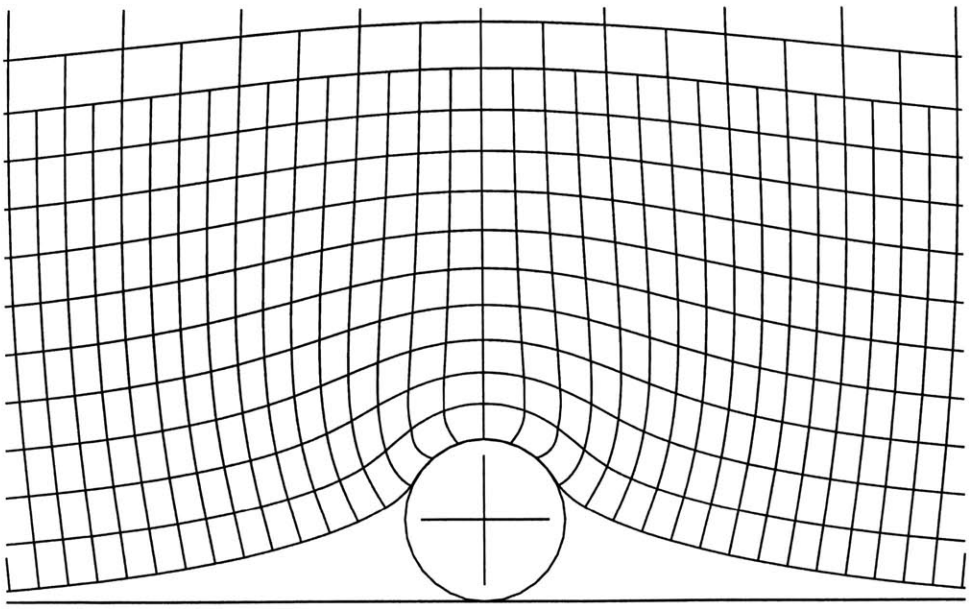

Figure 4-18: Deformed Unfilled Polyurethane Mesh with Elastic-Viscoplastic Model

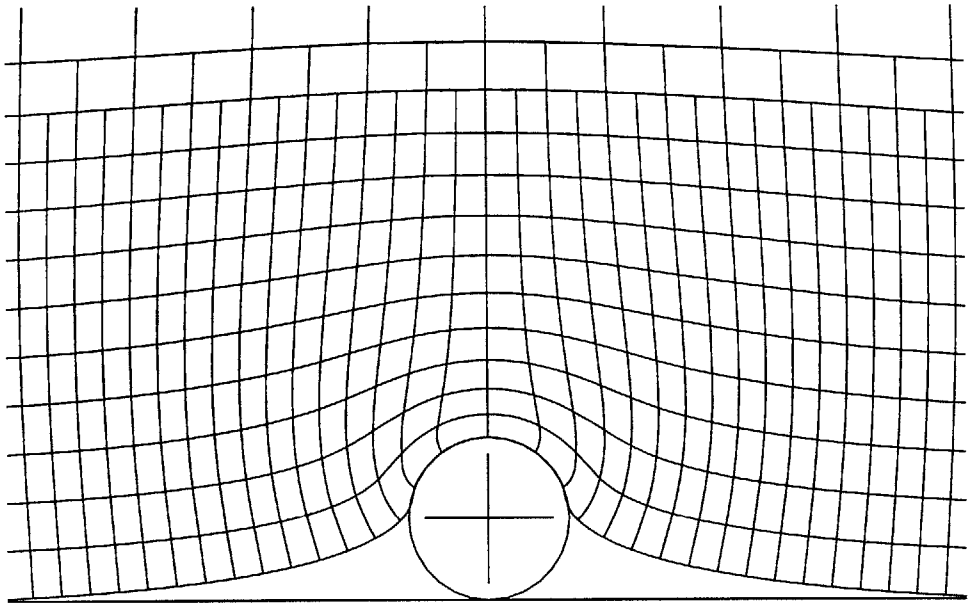

highly distorted. The deformation of the elastomer modeled with the Eight Chain model in Figure 4-17, however, is relatively uniform. The elastomer has not yet contacted the entire upper circumference of the particle. Furthermore, the elements around the particle are not nearly as distorted as those in Figure 4-18.

Contour plots of the maximum principal stresses for both simulations are displayed in Figures 4-19 and 4-20. The contour plot for the simulation with the Eight Chain model shows a maximum tensile stress of 4.70 MPa in the region where the elastomer lifts off the particle. On top of the particle, for a distance of approximately 4 μm, a region of entirely compressive stresses still exists. The elastic-viscoplastic model has significantly greater maximum of 7.77 MPa also in the area where the elastomer lifts off the particle. Directly above the particle, however, the stresses are predominantly tensile with a maximum of 6.03 MPa.

Modeling the elastomer with the elastic-viscoplastic model clearly changes the way the material interacts with the particle. Whereas the Eight Chain model allows the elastomer to uniformly "bend" over the particle, the elastic-viscoplastic model forces the elastomer to deform around the particle. The discrepancy is due to the elastic-

Figure 4-19: Maximum Principal Stress Contour Plot with Eight Chain Model

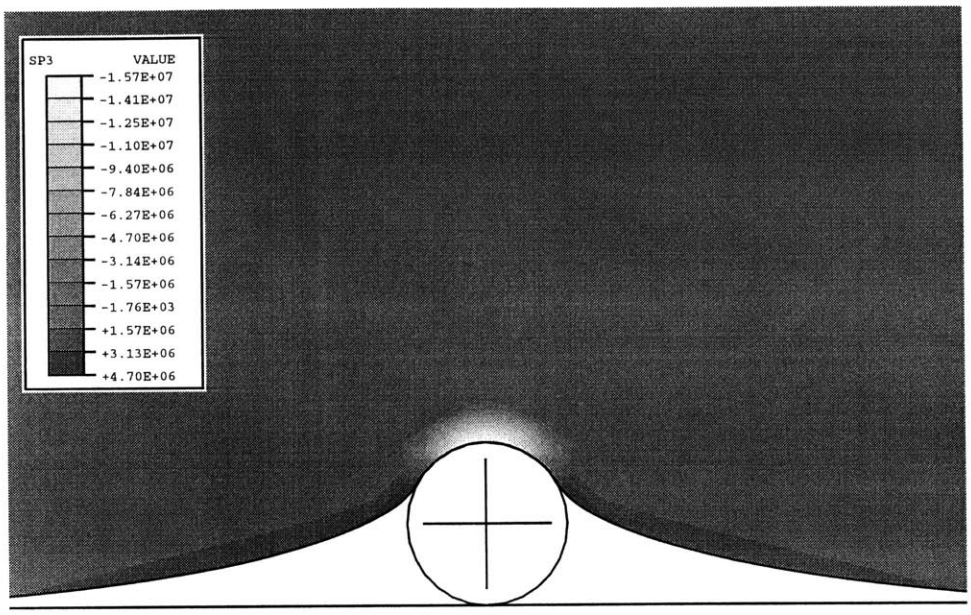

Figure 4-20: Maximum Principal Stress Contour Plot with Elastic-Viscoplastic Model

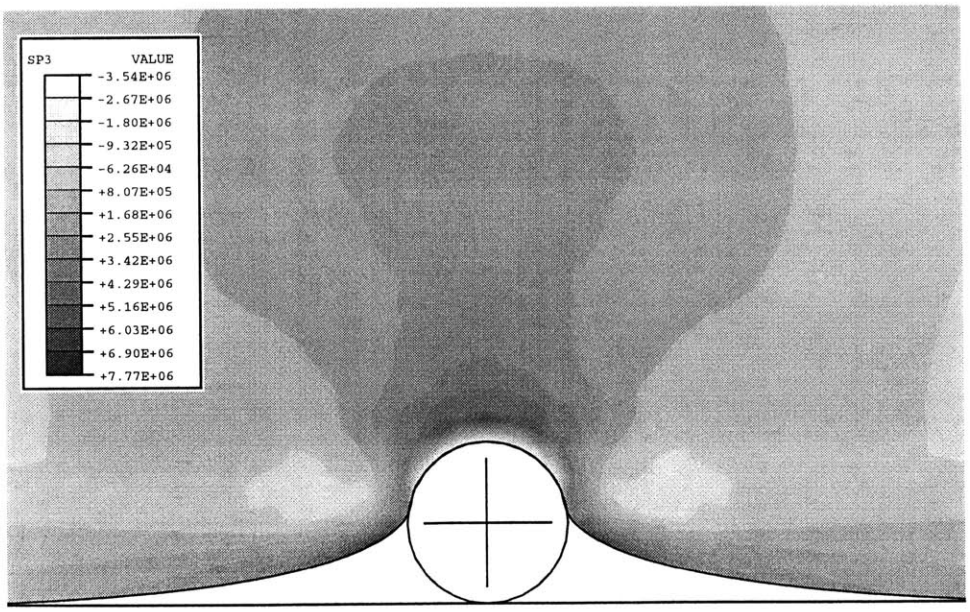

viscoplastic model's ability to capture the initially stiff response of the elastomer. Figure 4-5 shows that the elastic-viscoplastic model does not "yield" until a stress of ~6.5 MPa. Near the particle, where the strains are high, the material deforms extensively. Further from the particle, where the strains are lower, however, the stiffness of the material prevents extensive deformation. The initial stiffness of the elastic-viscoplastic model is also responsible for the large stress gradients in Figure 4-20. The Eight Chain model, on the other hand, exhibits a smooth, gently accelerating stress-strain curve. This material behavior allows the deformation to spread more evenly throughout the material and prevents steep stress gradients from forming.

While clearly more accurate than the Eight Chain model, the elastic-viscoplastic model has very high computational costs. Furthermore, at high strains, the differences between the models are not as severe. For these reasons, the Eight Chain model was used in all simulations presented in chapters 5 and 6.

Chapter 5

Micromechanical Modeling of Abrasive Wear of Filled Elastomers

Micromechanical modeling of fiber-filled polyurethane interacting with dirt particles was performed using the finite element package ABAQUS. The goal was to determine how the presence of fibers improves the wear resistance of the elastomer. The effect of fibers at various filler fractions on the maximum tensile stress in the matrix and the mobility of particles was investigated.

As discussed in chapters 2 and 4, on a microscopic scale, the abrasive wear of elastomers is a fatigue fracture process. Deformations due to abrasive particles create high tensile stresses in the elastomer and, when the cohesive strength of the material is reached, microcracking occurs. In this chapter, we, therefore, investigate the effect that the addition of fibers has on the maximum tensile stress reached in the elastomer during interaction with a dirt particle.

5.1 Preliminary Modeling Results

In this section, preliminary modeling of the abrasive wear of fiber-filled polyurethane is presented. In all simulations, the dirt particle is 30 μm in diameter, and the block of polyurethane is 320 μm tall. The width of the block varies depending on fiber orientation. The top row of nodes is displaced 78 μm in the negative 2-direction, a

displacement corresponding to 15% compression in the absence of the dirt particle.

A cylindrical glass fiber is added to the mesh at two different orientations. The fiber is 16 μm in diameter and has a length to diameter ratio of 8. The fiber is modeled as an isotropic linear elastic material with a Young's modulus of 72.5 GPa and a Poisson's ratio of 0.22. Friction is not considered in this section.

Figure 5-1 shows a mesh with a fiber oriented at 45 degrees to the horizontal. Before loading, the bottom tip of the fiber is 50 μm from the surface of the elastomer.

Figure 5-1: Elastomer with 45 Degree Fiber Mesh – Compressed

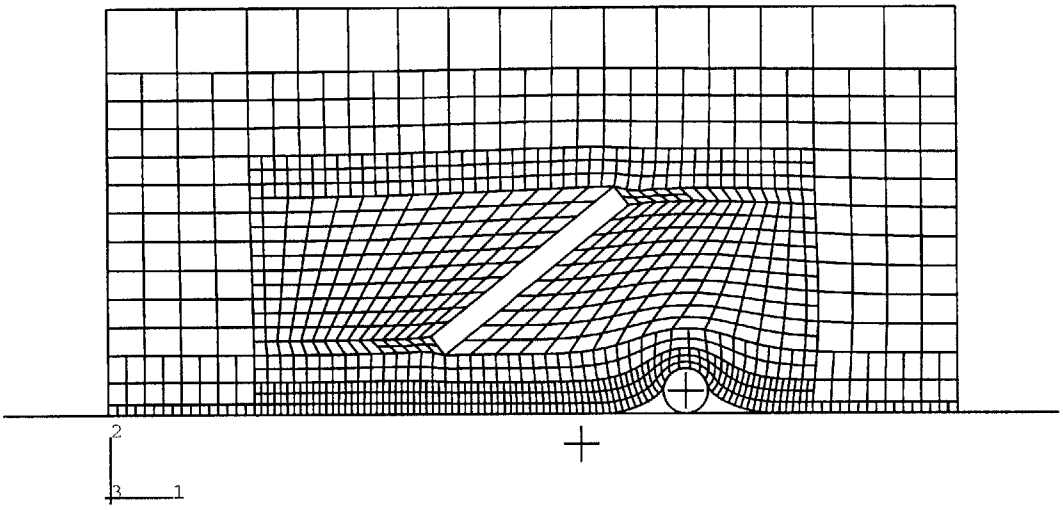

As in the previous section, the mesh is first compressed onto a 30 μm dirt particle and then sheared in the positive 1-direction over the dirt particle. Figure 5-2 displays contour plots of the maximum principal stresses in the elastomer at several different points in the shearing process. We compare the maximum value in each plot in Figure 5-2 to the value of 9.76 MPa for the unfilled elastomer block in Figure 4-12. Initially, in plot 1, the maximum stress is slightly lower at 9.19 MPa. As the fiber moves over the particle, however, the stress increases in plots 2 and 3 to 12.7 MPa and 14.0 MPa, respectively. In plot 4, when the fiber leaves the particle in its wake, the stress decreases to 8.96 Pa. Finally, in plot 5, when the fiber is well past the particle, the stress increases again to 10.2 MPa.

Figure 5-3 shows a mesh with the fiber oriented parallel to the bushing surface

Figure 5-2: Maximum Principal Stress Contour Plots

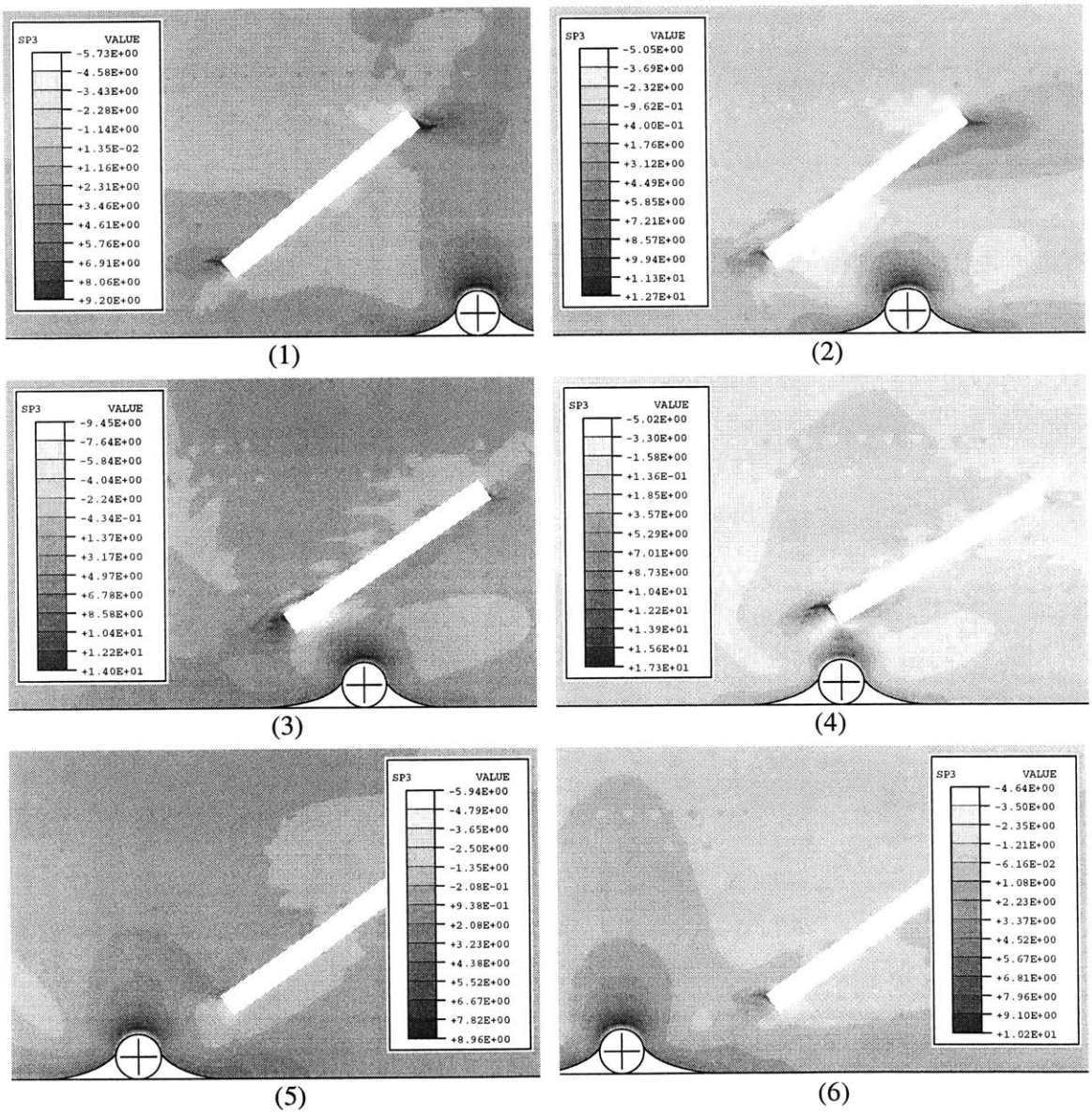

and perpendicular to the plane of the page. Before loading, the bottom of the fiber

Figure 5-3: Elastomer with Horizontal Fiber Mesh – Compressed

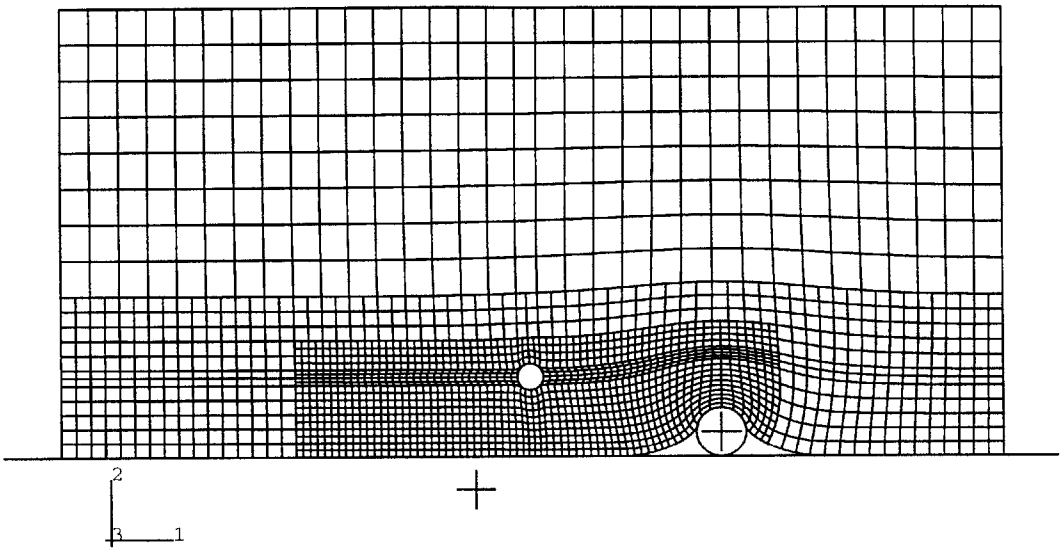

is 50 μm from the surface of the elastomer. The block is compressed onto a 30 μm dirt particle. Figure 5-4 shows the results of shearing the block from left to right over the dirt particle. In plot 1, the fiber has yet to influence the stress field around the particle, and the maximum principal stress is 8.04 MPa. This value is slightly lower than the values seen in the previous simulations due to the use of a more refined mesh. As the fiber moves closer to the dirt particle in plot 2, the maximum stress decreases slightly to 7.74 MPa. In plot 3, the fiber is directly over the particle, and the stress increases to its maximum value of 9.27 MPa. As the fiber moves past the particle in plot 4, the stress decreases again to 7.76 MPa. Continued shearing motion causes the stress at the particle to return to the level shown in plot 1.

Simulations were also run with fibers oriented at 15 degrees and 67 degrees to the horizontal. Results were similar to those presented above.

Figure 5-4: Maximum Principal Stress Contour Plots

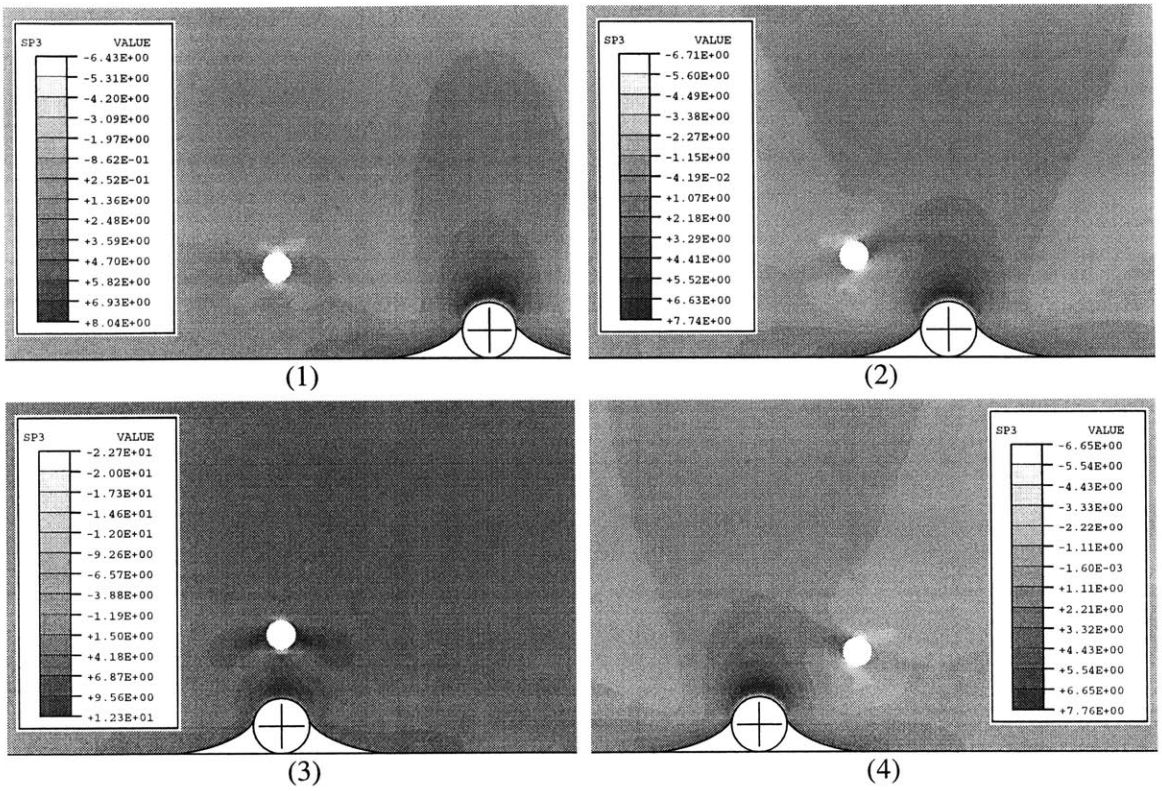

5.2 Parallel Fiber Simulations: Effect on Maximum Tensile Stress in Matrix

The observations of chapter 3 indicate that fibers are present near or at the surface of the seal lip. Simulations were therefore conducted with fibers immediately at the surface of the elastomer block. In the spirit of the experimental work of Wada and Uchiyama, simulations in this section were run with two parallel fibers oriented normal (N), longitudinal (L), and tangential (T) to the shearing direction. To simulate the effect of varying the filler fraction of the material, fiber spacings of 5, 7 and 10 fiber diameters were used. The dirt particle is 15, 30, or, in several instances, 5 μm in diameter. Approaching the estimated critical cluster size of 100 μm, the 30 μm dirt particle can also be thought to represent a small cluster of particles. The height of the polyurethane block is 192 μm while the width varies depending on the fiber

orientation. The top row of nodes is displaced in the negative 2-direction 28.8 μm plus the diameter of the dirt particle. This displacement corresponds to 15% compression in the absence of the dirt particle.

5.2.1 Unfilled Elastomer Simulations

Unfilled elastomer simulations were repeated with meshes of the same size and similar refinement as the meshes used in the parallel fiber simulations presented later in this section. Figure 5-5 shows the 5 μm particle simulation. The maximum principal stress

Figure 5-5: Unfilled Elastomer with 5 μm Particle

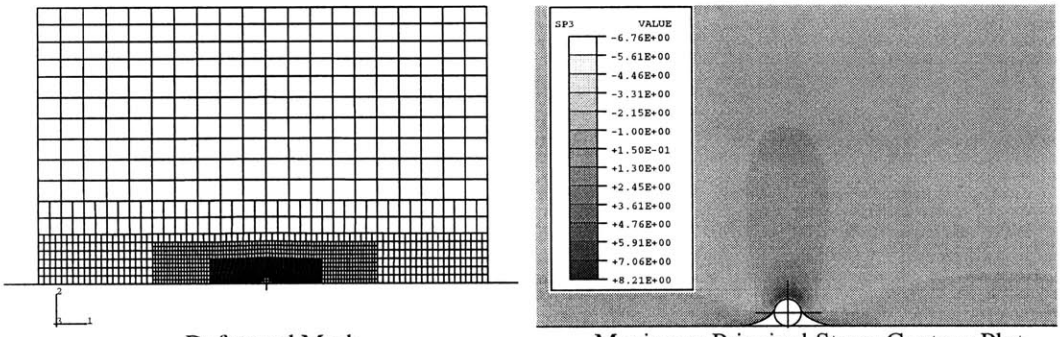

Deformed Mesh

Maximum Principal Stress Contour Plot

is 8.21 MPa. Figure 5-6 shows the 15 μm particle simulation which has a slightly

Figure 5-6: Unfilled Elastomer with 15 μm Particle

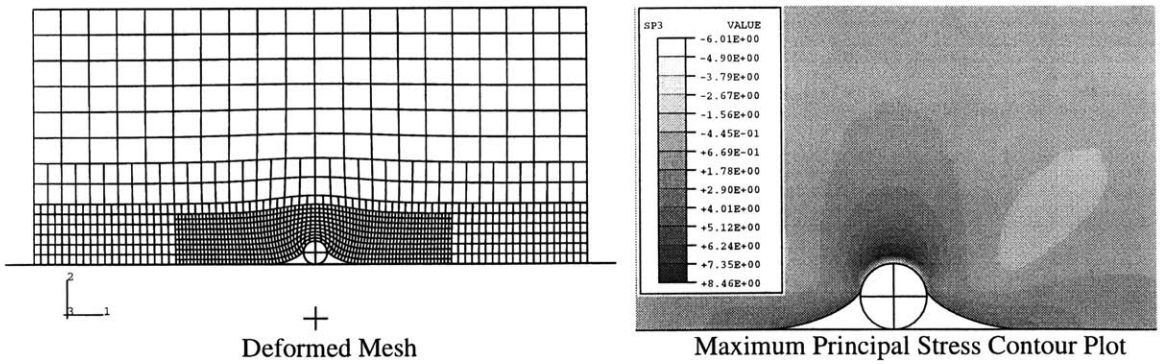

Deformed Mesh

Maximum Principal Stress Contour Plot

higher maximum principal stress of 8.46 MPa. The 30 μm particle simulation, with a maximum principal stress of 8.73 MPa, is displayed in Figure 5-7. If the elastomer

Figure 5-7: Unfilled Elastomer with 30 μm Particle

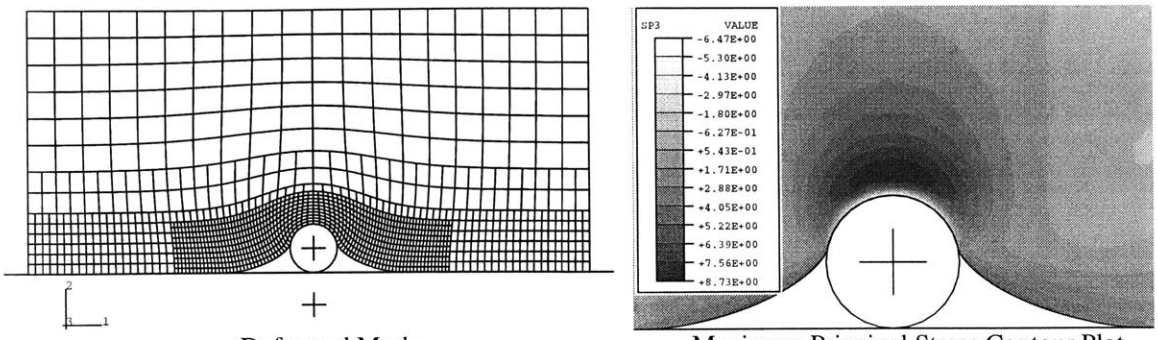

Deformed Mesh

Maximum Principal Stress Contour Plot

block were infinite in size, the stress field around the particle would be independent of the size of the particle. While it *is* much larger than the particle, the block is not infinite and the stress therefore increases slightly with the particle size. The discrepancy is small enough to neglect. Regardless of particle size, we expect to see a maximum principal stress of ~8.5 MPa.

5.2.2 Normal Fiber Simulations

Figures 5-8 through 5-14 show the results for the normal fiber simulations. Two glass fibers are positioned perpendicular to the bushing surface with their ends at the surface of the elastomer.

The results for fibers oriented normally at a spacing of 5 fiber diameters are shown in Figure 5-8 for a 15 μm particle and Figure 5-9 for a 30 μm particle. The meshes have been extensively refined in the vicinity of the tips of the fibers to allow for the strain concentrations that exist there. We see that, in both Figures 5-8 and 5-9, the elastomer deforms around the particles less than in Figures 5-6 and 5-7. The amount of deformation can easily be gaged by noting the increase in the size of the gap between the particle and the elastomer and the decrease in the curvature of the elastomer surface around the particle in the simulations with fibers.

The fibers act as load bearers shielding the much softer matrix elastomer from a portion of the applied load. In the case of the 15 μm particle, the protection provided

Figure 5-8: Normal Fibers 5X Spacing with 15 μm Particle

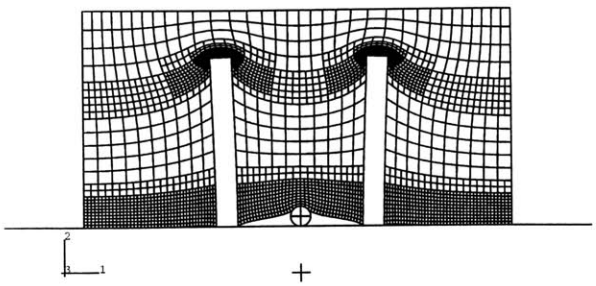

Deformed Mesh

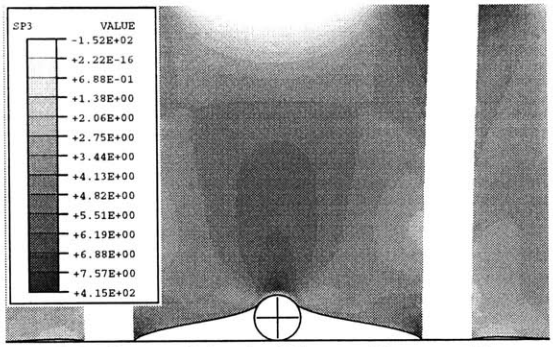

Maximum Principal Stress Contour Plot

Figure 5-9: Normal Fibers 5X Spacing with 30 μm Particle

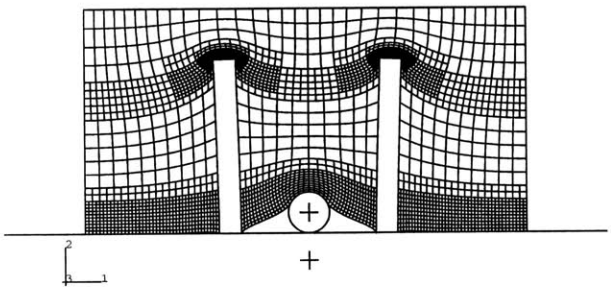

Deformed Mesh

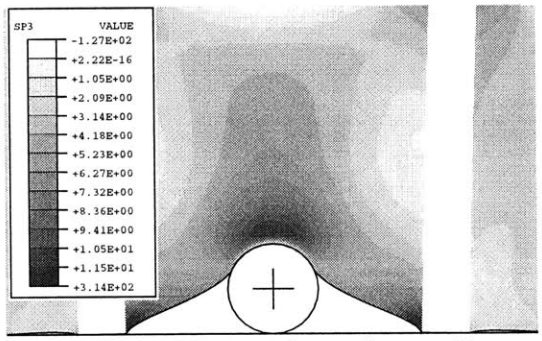

Maximum Principal Stress Contour Plot

by the fibers reduces the maximum principal stress at the particle from 8.5 MPa with the unfilled elastomer to 7.57 MPa with the normal fiber elastomer. Increasing the particle size to 30 μm, however, increases the maximum principal stress with the normal fiber elastomer to 11.5 MPa at the particle. The fibers prevent material from flowing into the region around the particle. In effect, the elastomer is "clamped" on either side of the particle at the fibers and, as the elastomer block is compressed, the material at the surface is stretched around the particle producing higher than normal tensile stresses at the particle. This phenomenon is exacerbated as the particle size and, hence, the amount of deformation increases. With a 30 μm particle, the load bearing advantage of the fibers is more than cancelled out by their restriction of material flow.

Increasing the fiber spacing to 7 fiber diameters, we see an increase in the maximum tensile stress at the particle to 12.4 MPa with the 15 μm particle in Figure 5-10 and 14.1 MPa with the 30 μm particle in Figure 5-11. The decrease in the size of the gaps and the increase in the curvature of the elastomer around the particles indicate that the fibers are bearing a smaller proportion of the load in the vicinity of the particle than they are in the simulations with the 5 fiber diameter spacing. The fibers are still, however, restricting the flow of material around the particle. As the load bearing effect weakens, the tensile stress at the particle increases. Figure 5-12

Figure 5-10: Normal Fibers 7X Spacing with 15 μm Particle

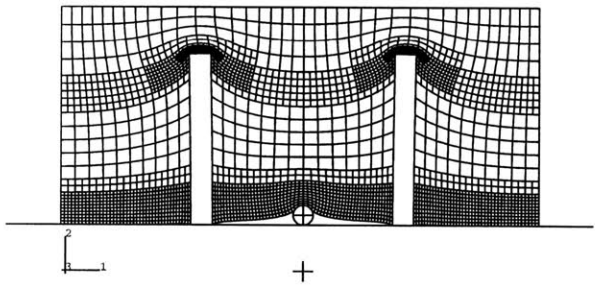

Deformed Mesh

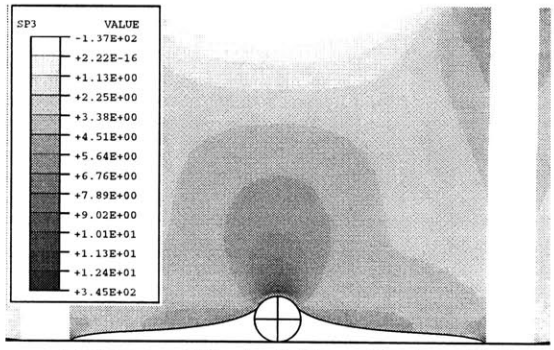

Maximum Principal Stress Contour Plot

Figure 5-11: Normal Fibers 7X Spacing with 30 μm Particle

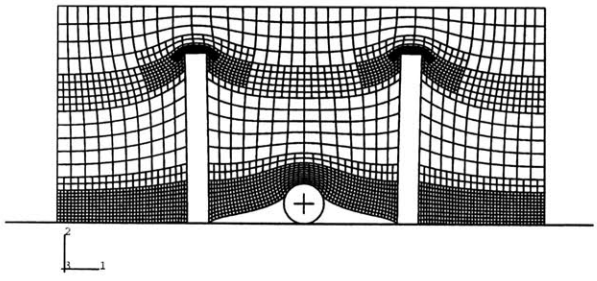

Deformed Mesh

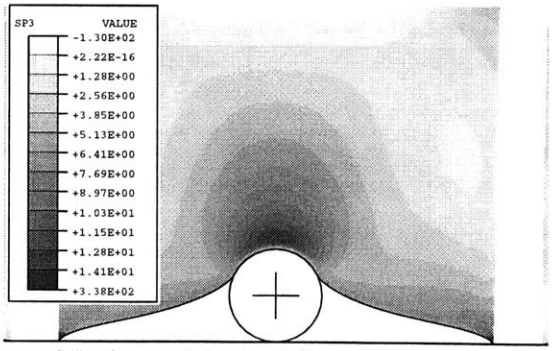

Maximum Principal Stress Contour Plot

shows that, even with a 5 μm particle, the maximum tensile stress increases to 10.7 MPa.

Figure 5-12: Normal Fibers 7X Spacing with 5 μm Particle

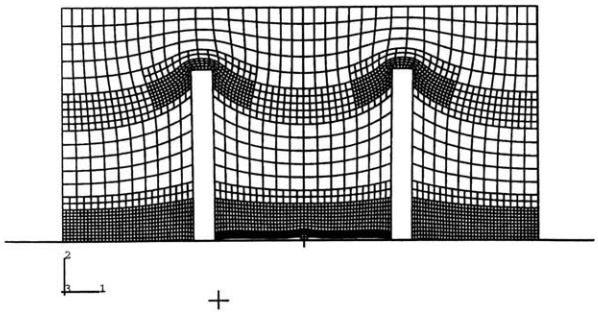

Deformed Mesh

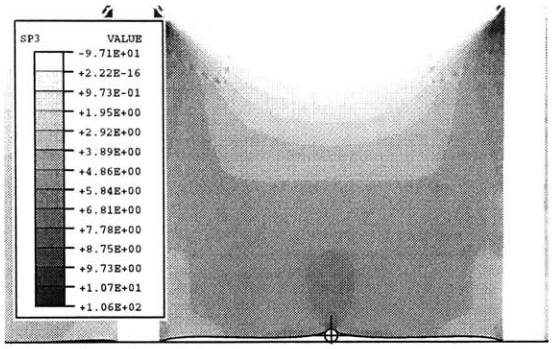

Maximum Principal Stress Contour Plot

A further increase in fiber spacing to 10 fiber diameters eliminates most, if not all, of the fibers' load bearing effect at the particle. We see a corresponding further increase in the maximum principal stress to 16.0 MPa with the 15 μm particle in Figure 5-10 and 15.4 MPa with the 30 μm particle in Figure 5-11. The fibers are not spaced closely enough to shield the elastomer from deforming at the particle but still restrict the flow of material into this region creating higher than normal tensile stresses at the particle.

Figure 5-13: Normal Fibers 10X Spacing with 15 μm Particle

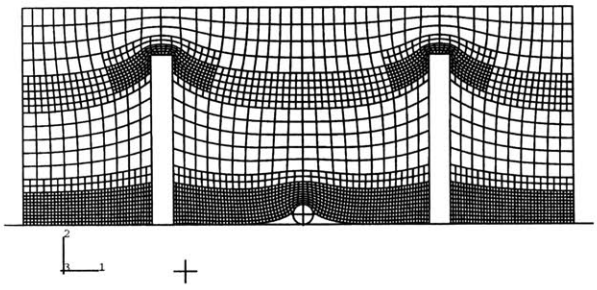

Deformed Mesh

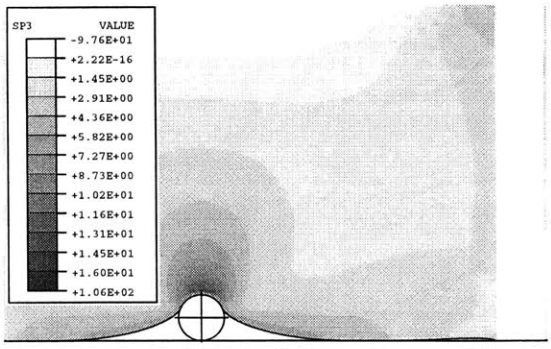

Maximum Principal Stress Contour Plot

Figure 5-14: Normal Fibers 10X Spacing with 30 μm Particle

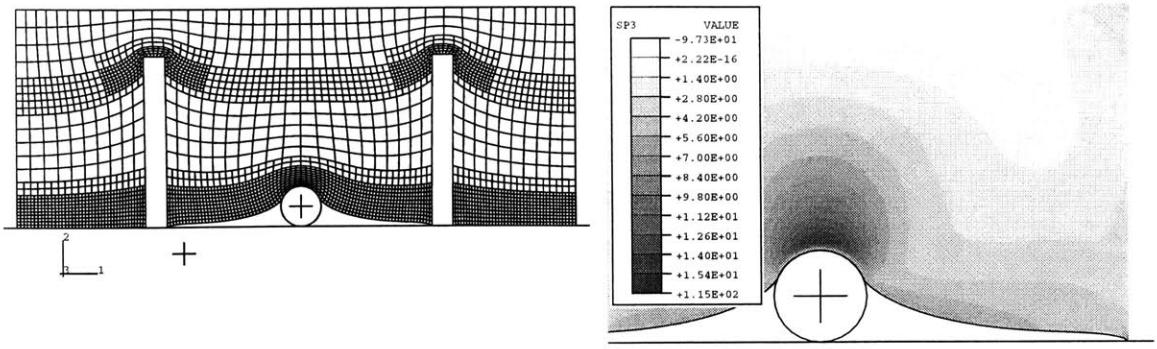

Deformed Mesh

Maximum Principal Stress Contour Plot

5.2.3 Longitudinal Fiber Simulations

Figures 5-8 through 5-14 show the results for the longitudinal fiber simulations. Two glass fibers are positioned parallel to the bushing surface and perpendicular to the plane of the page with their edges at the surface of the elastomer. In order to facilitate the meshing of the surrounding elastomer, the fibers were modeled with a flat edge in contact with the bushing surface. This is a realistic approximation as a flat would likely be created by the abrasive wear process on any fiber in this position and at this orientation.

The results for longitudinal fibers spaced 5 fiber diameters apart are shown in Figure 5-15 for a 5 μm particle, Figure 5-16 for a 15 μm particle, and Figure 5-17 for a 30 μm particle. The maximum principal stress increases slightly to 9.36 MPa with the 5 μm particle, 9.95 MPa with the 15 μm particle, and 10.3 MPa with the 30 μm particle. The longitudinal fiber configuration clearly has minimal load bearing capacity. The contour plots indicate that the fibers do, however, affect the stress field around the particle. Similar to the normal fibers, the longitudinal fibers restrict the flow of material into the vicinity of the particle intensifying the tensile stress at the particle.

Increasing the fiber spacing to 7 fiber diameters, we see a decrease in the maximum principal stress to 9.12 MPa with the 15 μm particle in Figure 5-18. The fibers' effect on the elastomer's flow characteristics weakens as the fiber spacing increases.

Figure 5-15: Longitudinal Fibers 5X Spacing with 5 μm Particle

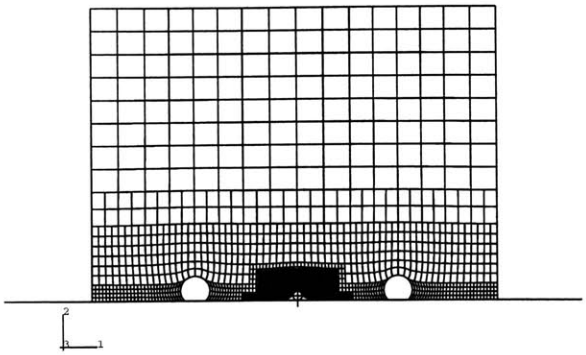

Deformed Mesh

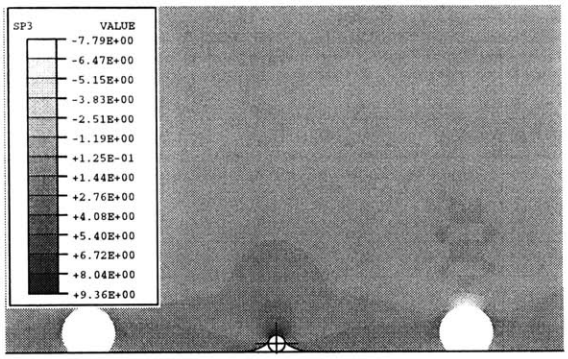

Maximum Principal Stress Contour Plot

Figure 5-16: Longitudinal Fibers 5X Spacing with 15 μm Particle

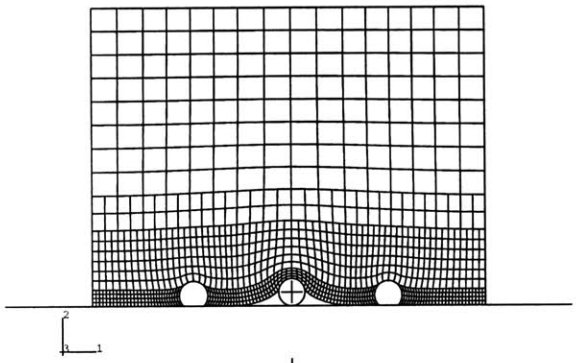

Deformed Mesh

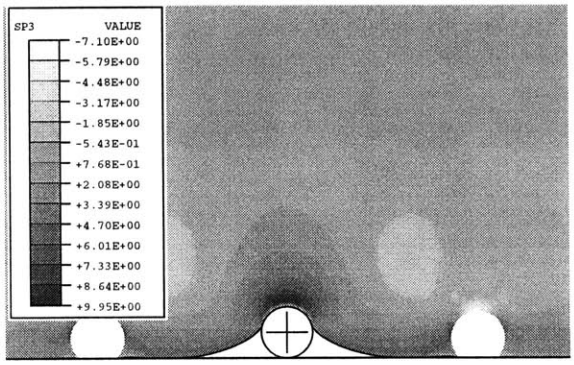

Maximum Principal Stress Contour Plot

Figure 5-17: Longitudinal Fibers 5X Spacing with 30 μm Particle

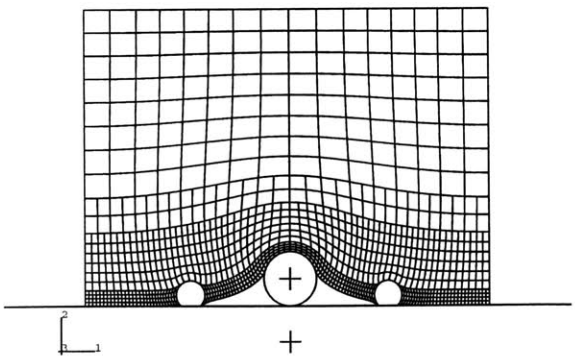

Deformed Mesh

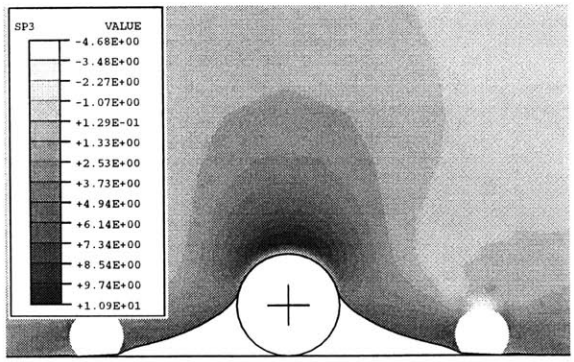

Maximum Principal Stress Contour Plot

Figure 5-18: Longitudinal Fibers 7X Spacing with 15 μm Particle

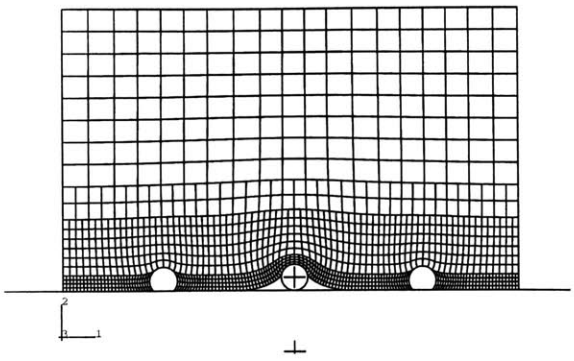

Deformed Mesh

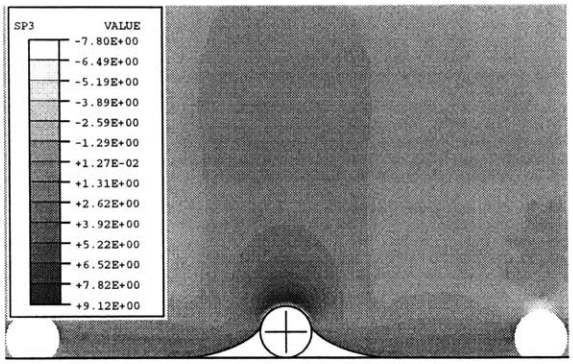

Maximum Principal Stress Contour Plot

Figure 5-19: Longitudinal Fibers 7X Spacing with 30 μm Particle

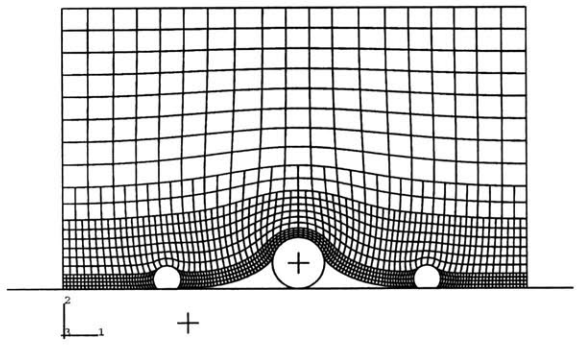

Deformed Mesh

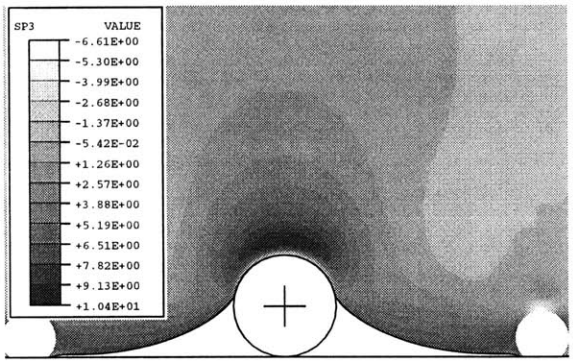

Maximum Principal Stress Contour Plot

For the 30 μm particle simulation shown in Figure 5-19, the maximum principal stress increases negligibly to 10.4 MPa. The contour plot shows a more extensive interaction between the stress field around the particle and the stress field around the fiber than in the case of the 15 μm particle. The fibers' effect on the material's flow field has not yet begun to diminish.

Further increasing the fiber spacing to 10 fiber diameters decreases the maximum tensile stress to 8.46 MPa with the 15 μm particle in Figure 5-20 and 9.95 MPa with the 30 μm particle in Figure 5-21. As the fiber spacing increases, the stress field around the particle approaches that of the unfilled elastomer for both particle sizes. The fibers' effect wanes as the spacing increases.

Figure 5-20: Longitudinal Fibers 10X Spacing with 15 μm Particle

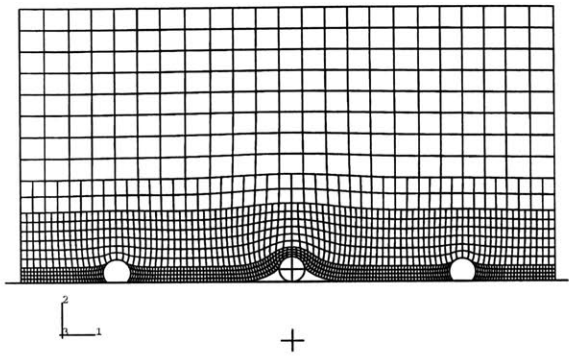

Deformed Mesh

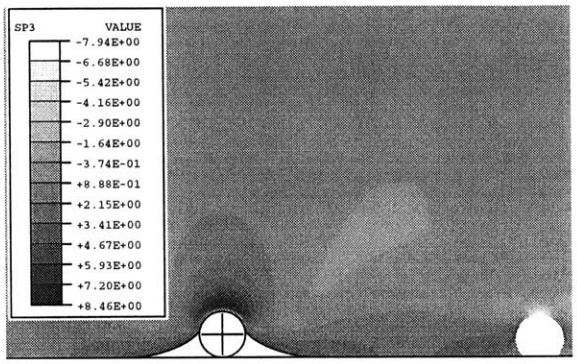

Maximum Principal Stress Contour Plot

Figure 5-21: Longitudinal Fibers 10X Spacing with 30 μm Particle

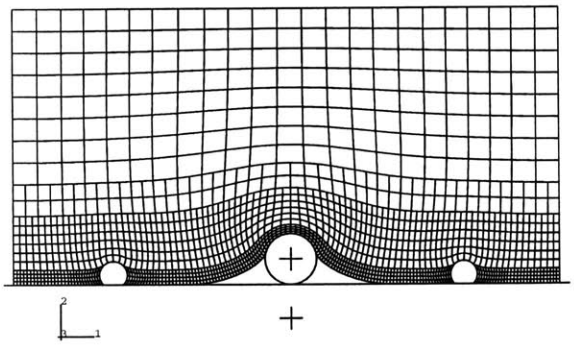

Deformed Mesh

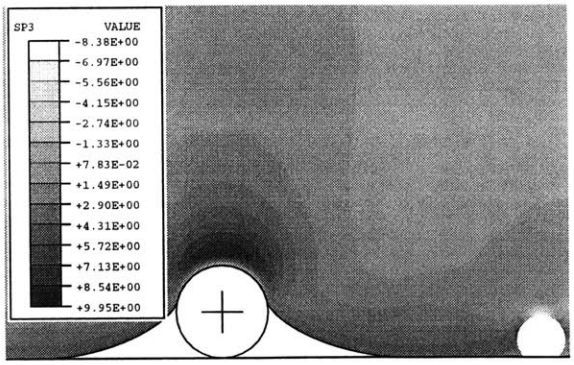

Maximum Principal Stress Contour Plot

5.2.4 Tangential Fiber Simulations

Figures 5-22 through 5-27 show the results for the tangential fiber simulations. Two glass fibers are positioned parallel to the bushing surface and parallel to the plane of the page with their edges at the surface of the elastomer.

The tangential fiber configuration with a fiber spacing of 5 fiber diameters proves to be the worst case scenario. The maximum tensile stress increases to 23.9 MPa with the 15 μm particle in Figure 5-22 and 23.3 MPa with the 30 μm particle in Figure 5-23.

Figure 5-22: Tangential Fibers 5X Spacing with 15 μm Particle

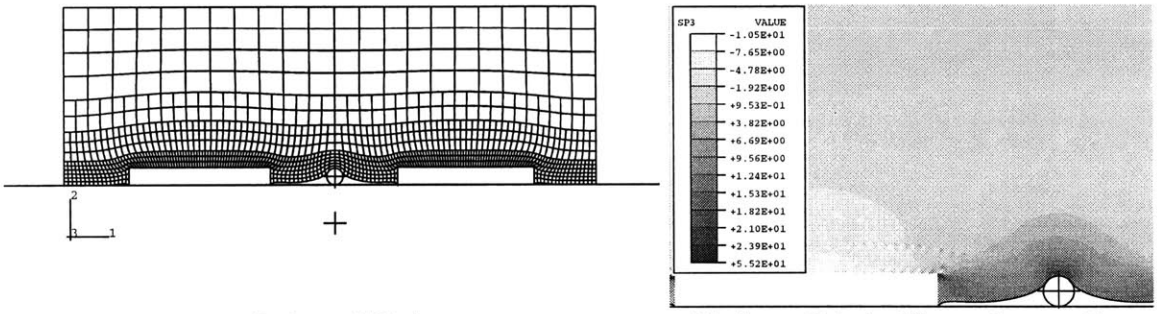

Deformed Mesh | Maximum Principal Stress Contour Plot

Figure 5-23: Tangential Fibers 5X Spacing with 30 μm Particle

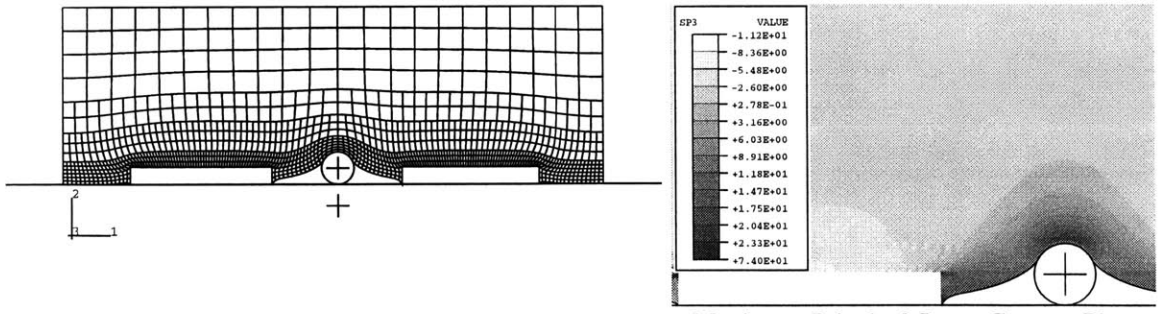

Deformed Mesh | Maximum Principal Stress Contour Plot

The deformed meshes clearly indicate how the fibers interrupt the flow field of the elastomer. In the unfilled elastomers shown in Figures 5-6 and 5-7, on either side of the particle, the mesh smoothly and consistently bends in the direction of the

particle as the material flows freely around the particle. In the tangential fiber-filled elastomers, however, the material is effectively pinned at the fibers. The mesh curves in the direction of the fiber near the fiber and in the direction of the particle near the particle as the elastomer is stretched between the two. The result is a significant magnification of the tensile stresses between the fibers and around the particle.

Increasing the fiber spacing moves the effect of the fiber further from the particle and therefore decreases the maximum principal stress in the elastomer. For the 7 fiber diameter spacing, the maximum tensile stress decreases to 21.1 MPa with the 15 μm particle in Figure 5-24 and 19.2 MPa with the 30 μm particle in Figure 5-25. For the 10 fiber diameter spacing, the maximum tensile stress decreases to 17.6

Figure 5-24: Tangential Fibers 7X Spacing with 15 μm Particle

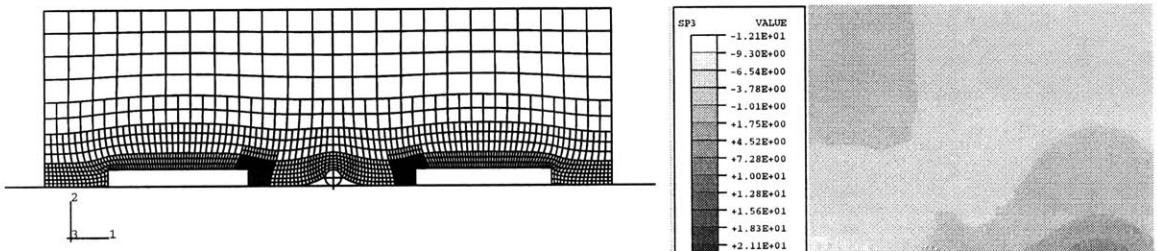

Deformed Mesh

Maximum Principal Stress Contour Plot

Figure 5-25: Tangential Fibers 7X Spacing with 30 μm Particle

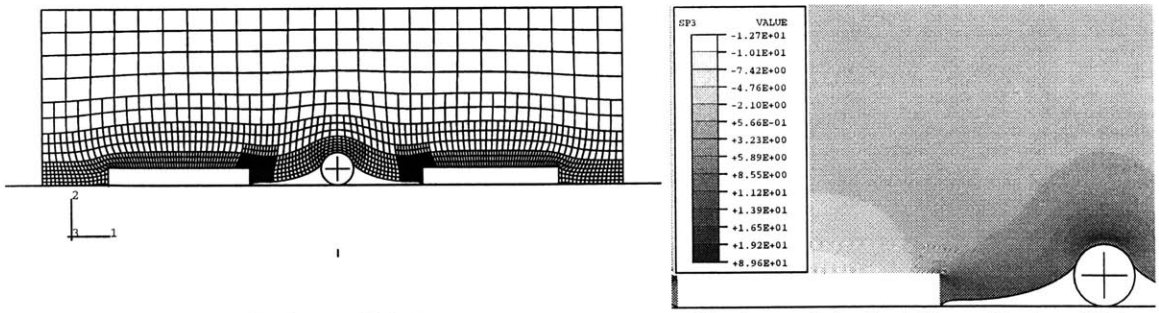

Deformed Mesh

Maximum Principal Stress Contour Plot

MPa with the 15 μm particle in Figure 5-26 and 16.3 MPa with the 30 μm particle in Figure 5-27. Figure 5-28 shows that even with a 5 μm particle the maximum

Figure 5-26: Tangential Fibers 10X Spacing with 15 μm Particle

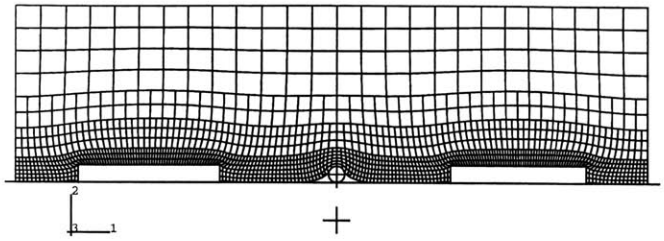

Deformed Mesh

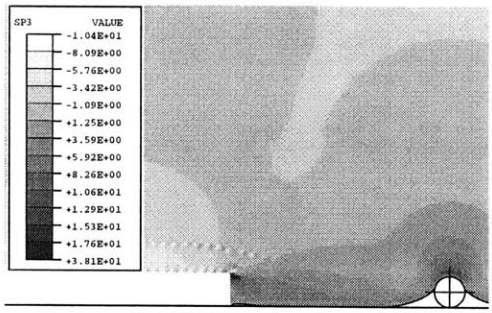

Maximum Principal Stress Contour Plot

Figure 5-27: Tangential Fibers 10X Spacing with 30 μm Particle

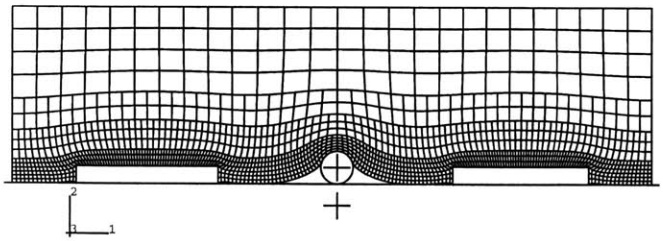

Deformed Mesh

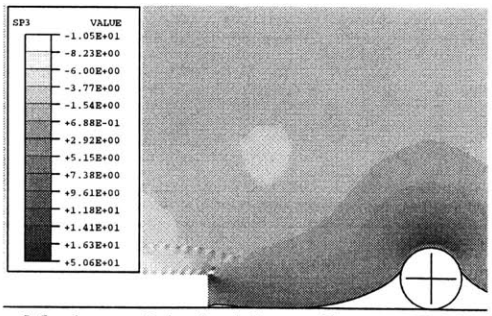

Maximum Principal Stress Contour Plot

Figure 5-28: Tangential Fibers 10X Spacing with 5 μm Particle

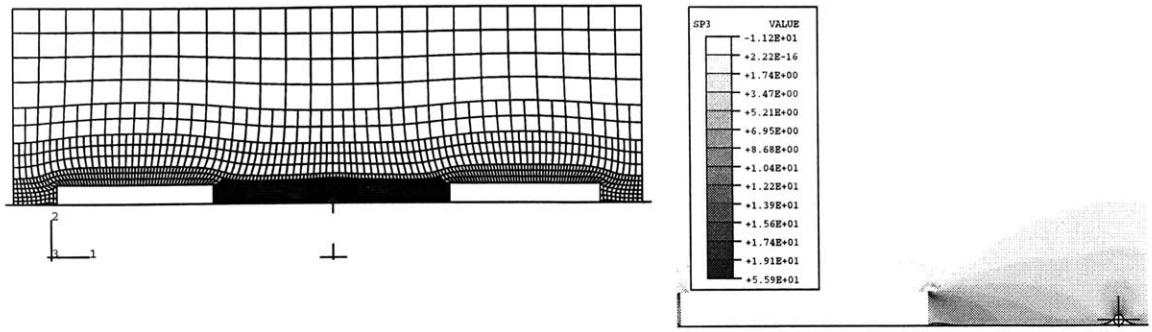

Deformed Mesh

Maximum Principal Stress Contour Plot

principal stress more than doubles to 19.1 MPa. Further increase of the fiber spacing would eventually produce a stress field identical to that of the unfilled elastomer.

5.2.5 Summary

The preceding simulations show that, for the most part, the addition of fibers to the elastomer actually *increases* the maximum principal stress in the elastomer at the particle by influencing the way material flows around the particle. The exception is the normal fiber configuration with a 15 μm particle and a fiber spacing of 5 fiber diameters. In this particular case, the maximum principal stress is reduced by slightly more than 10%. It appears that closely spaced normal fibers might increase the wear resistance of an elastomer if the abrasive particles were significantly smaller than the fibers.

5.3 Parallel Fiber Simulations: Effect on Particle Mobility

In the track seal application, the end of the break-in period and the beginning of the aggressive wear period is marked by the formation of the critical size clusters of particles. Discouraging particles from entering the seal lip contact band and, once they have penetrated the contact band, deterring them from aggregating would delay

cluster formation and, hence, extend the break-in period. In this section, we therefore investigate how fibers affect the ability of particles to move between the elastomer and the bushing surface.

5.3.1 Model Description

Select meshes from Section 5.2 were used for the simulations in this section. As in Section 5.2 and depicted in Figure 4-1, the elastomer block was compressed onto a fixed particle in step 1 and then sheared over the particle in step 2. The elastomer was again compressed in the negative 2-direction by 28.8 microns plus the diameter of the dirt particle, a displacement corresponding to 15% compression in the absence of the dirt particle. The block was then sheared in the positive 1-direction until the mesh became too distorted for the simulation to continue. The total force required to move the block was calculated and plotted as a function of the distance traveled. While it is the elastomer that is actually moved, these simulations are equivalent to fixing the block and measuring the force required to displace the particle in the 1-direction. We may therefore speak equivalently in terms of the force required to move the particle.

5.3.2 Normal Fibers

Figures 5-29, 5-30, and 5-31 show the results for the particle mobility simulations with the normal fiber configuration mesh. In all three cases, the fiber is clearly inhibiting the particle's motion. The particle moves easily between the elastomer and the bushing surface until it encounters the fiber. The particle then pushes against the fiber causing the fiber to rotate within the elastomer matrix. In Figure 5-29, the 5 μm particle is completely trapped by the fiber when the simulation ends. There is no gap between the fiber and the rigid surface for the particle to pass through. In Figure 5-30, we see that the 15 μm particle lifts the fiber ever so slightly off of the rigid surface before the simulation ends. In Figure 5-31, however, we notice that the 30 μm particle has lifted the fiber nearly 10 μm from the rigid surface. If the simulation

Figure 5-29: Normal Fibers and 5 μm Particle

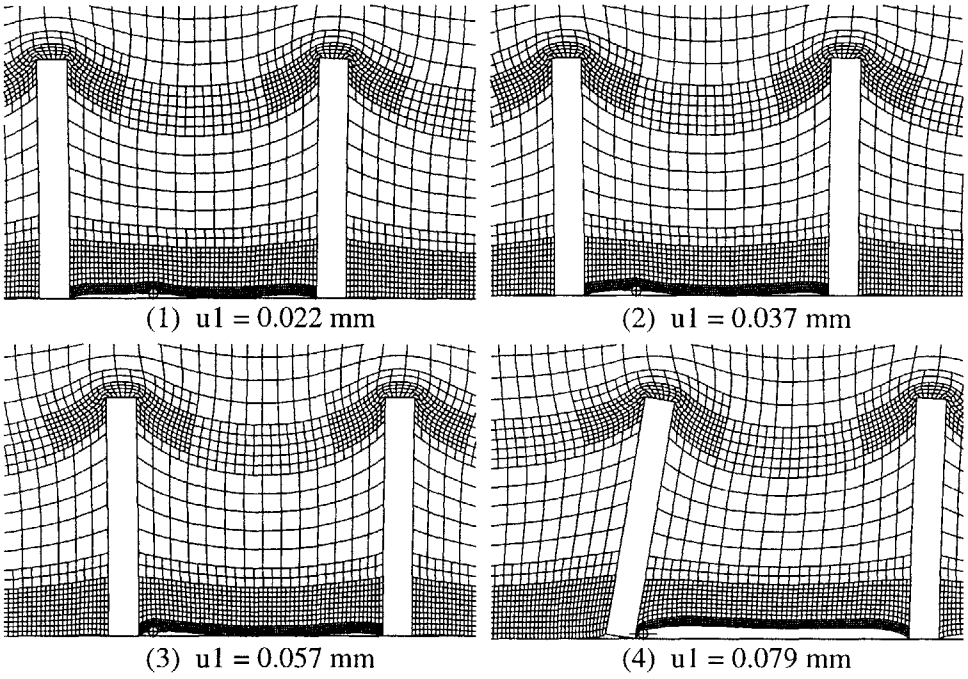

Figure 5-30: Normal Fibers and 15 μm Particle

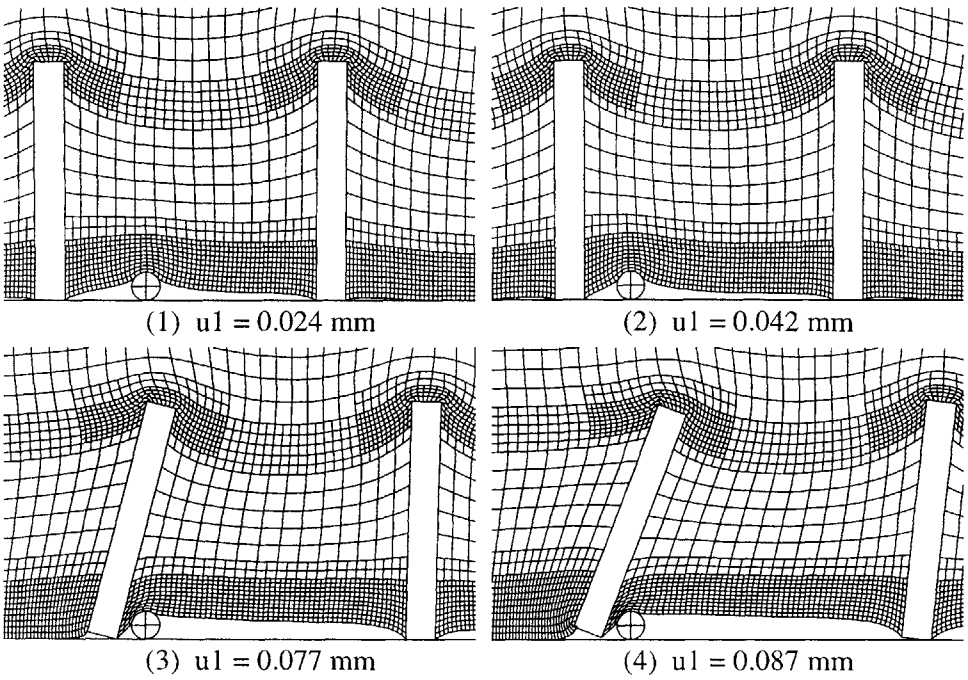

Figure 5-31: Normal Fibers and 30 μm Particle

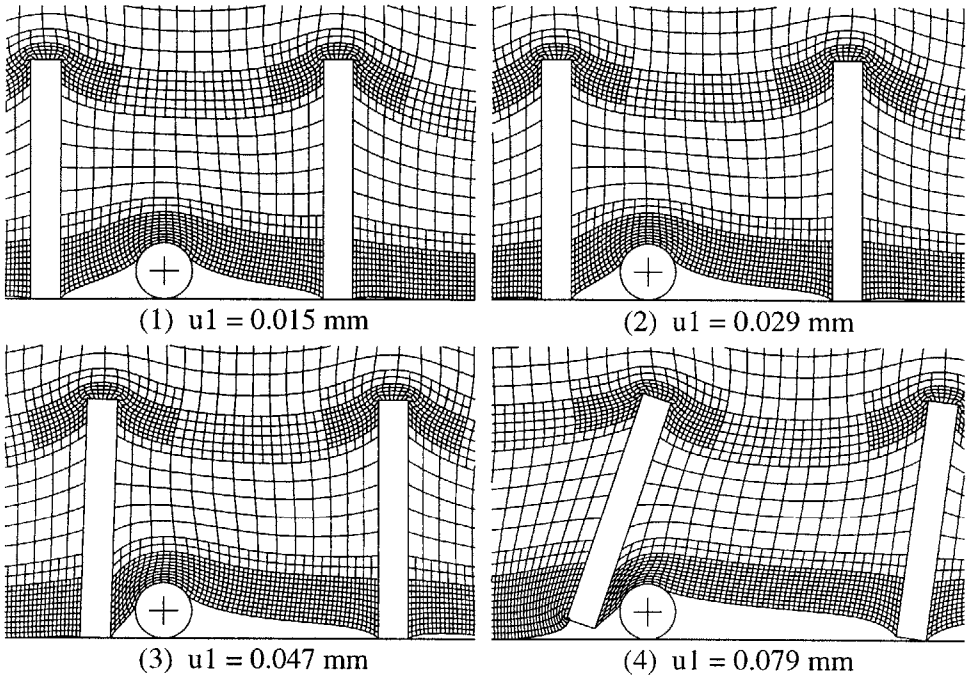

were to continue, it appears that the particle would be able to pass underneath the fiber.

The force vs. displacement curves for the three simulations are shown in Figure 5-32. The curves are initially flat indicating that, as mentioned above, before the particle encounters the fiber, very little force is required to move the particle between the elastomer and the bushing. As the particle moves closer to the fiber, the force required increases gradually. The 30 μm particle produces the largest deformation in the elastomer and therefore feels the effect of the fiber more rapidly. Both the 15 and 30 μm particles' curves end at approximately 700 kN. The 15 μm particle's curve ends with a fairly constant slope, but the 30 μm particle's curve, however, levels off at high displacements. It appears that the 30 μm particle would be able to pass beneath the fiber with a slight increase in the applied force while the 15 μm particle would be stuck against the fiber until the force increased dramatically.

By this theory, the simulation with the 5 μm particle should exhibit a rather steep, constant slope force vs. displacement curve with a maximum that surpasses

Figure 5-32: Normal Fibers: Reaction Force vs. Displacement

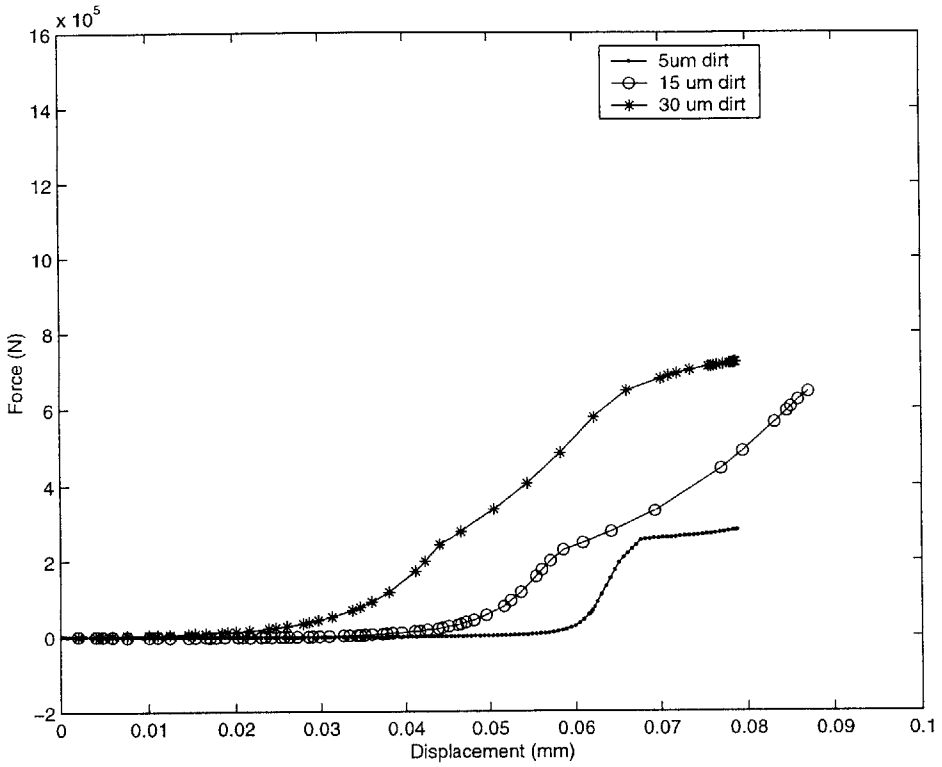

the final values of the 15 and 30 μm particles' curves. Figure 5-32 indicates that, to the contrary, the 5 μm particle's curve levels off first at less than 300 kN. We notice in the other two curves inflection points at approximately the same force value. Comparing the displacements at which these inflection points occur to the displacements in Figures 5-29, 5-30, and 5-31, we see that they correspond to when the particles cause the fibers to rotate in the matrix. Before the particle draws near to the fiber, most of the resistance is due to the deformation of the elastomer. Once the particle reaches the fiber, however, a large proportion of the resistance is caused by the fiber itself. At first it is relatively easy for the fiber to rotate, and the force vs. displacement curve dips correspondingly, but, as the material around the fiber deforms and hardens, the force required to move the particle increases again. The reduction in slope becomes more pronounced as the particle size decreases because the amount of material to deform between the fiber and the particle during fiber rotation decreases

with particle size. Furthermore, contacting the fiber very close to its end, a small particle applies the largest possible moment for a given force and induces nearly pure rotation of the fiber. Most of the resistance to motion of the 5 μm particle is due to the fiber's resistance to rotation. We see in Figure 5-29 that the fiber has rotated only slightly by the end of the simulation. Continued displacement of the particle would undoubtedly require an increase in the force applied.

5.3.3 Longitudinal Fibers

Figures 5-33 and 5-34 show the results for the particle mobility simulations with the longitudinal fiber configuration mesh. We see in Figure 5-33 that the smaller particle again becomes stuck against the fiber and barely lifts the fiber from the bushing surface. The larger particle, however, almost squeezes under the fiber before the

Figure 5-33: Longitudinal Fibers and 15 μm Particle

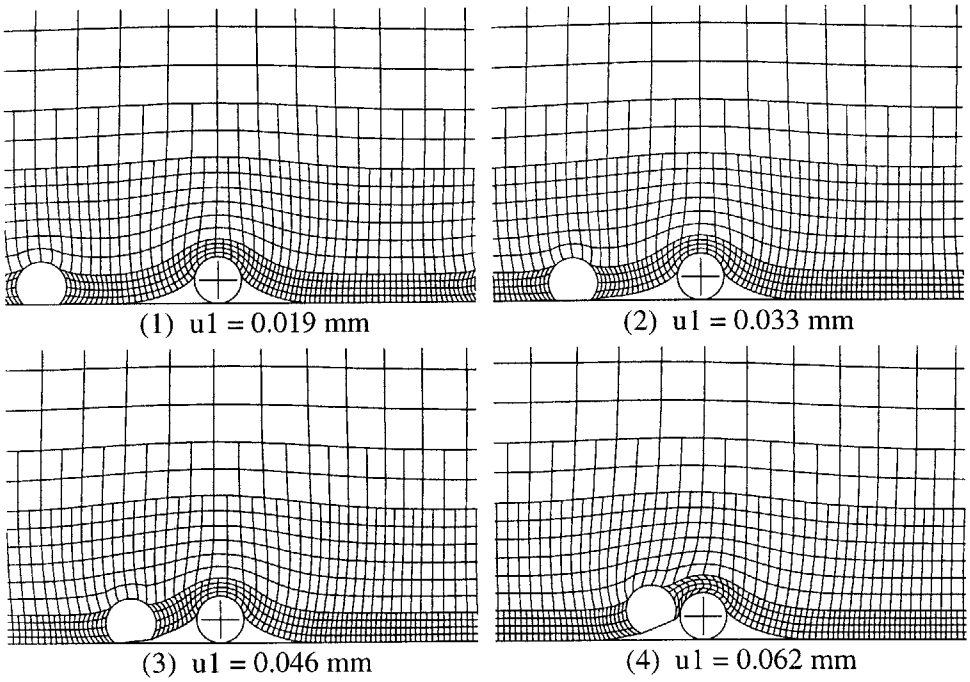

simulation ends.

The force vs. displacement curves for the longitudinal fiber simulations are shown in Figure 5-35. The flat initial slope indicates again that, before the particle ap-

Figure 5-34: Longitudinal Fibers and 30 μm Particle

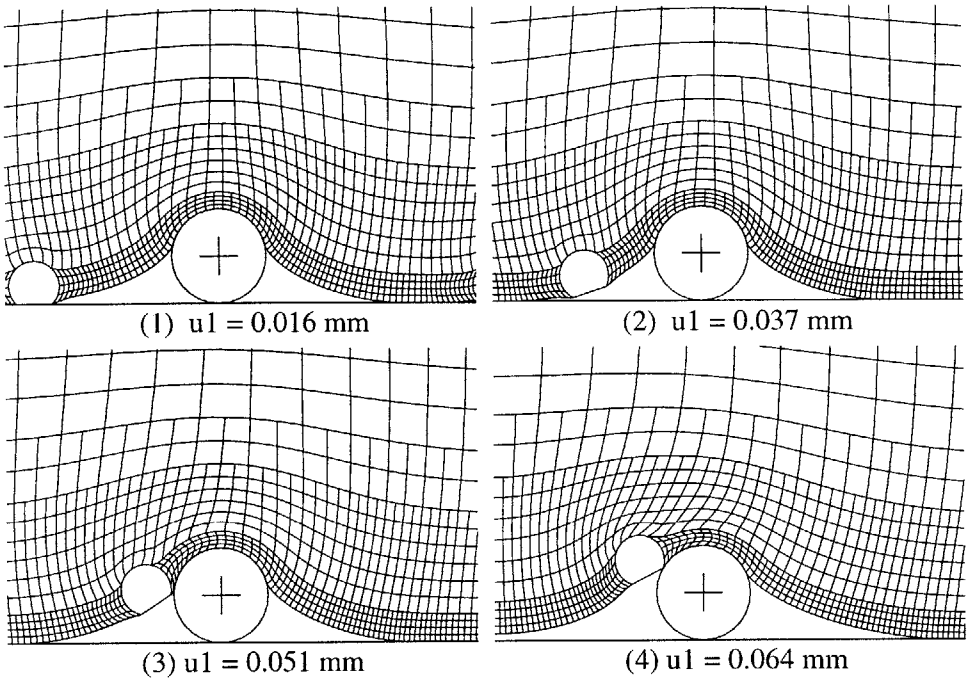

proaches the fiber, there is little barrier to particle motion. As the particle moves into the vicinity of the fiber, the applied force increases quite dramatically. The curve for the 30 μm particle takes off first since the larger particle and the larger corresponding deformation in the elastomer are felt by the fiber sooner. The force vs. displacement curves for the longitudinal fiber simulations have much steeper slopes than the curves for the normal fiber simulations. The steeper force vs. displacement curves are a result of the lower compliance of the longitudinal fiber. The longitudinal fiber does not rotate in the matrix as the normal fiber does when the particle presses against it.

The curves for the 15 μm particle and 30 μm particle have approximately equal and constant slopes once they start to increase from zero. The 30 μm particle simulation stopped at an applied force of 188.6 kN while the 15 μm particle simulation stopped at 108.5 kN. It is presumed that, if the simulations were to continue to run, the 30 μm particle would soon work its way completely underneath and then past the fiber. The force vs. displacement curve would level off and return to zero as the particle left

Figure 5-35: Longitudinal Fibers: Reaction Force vs. Displacement

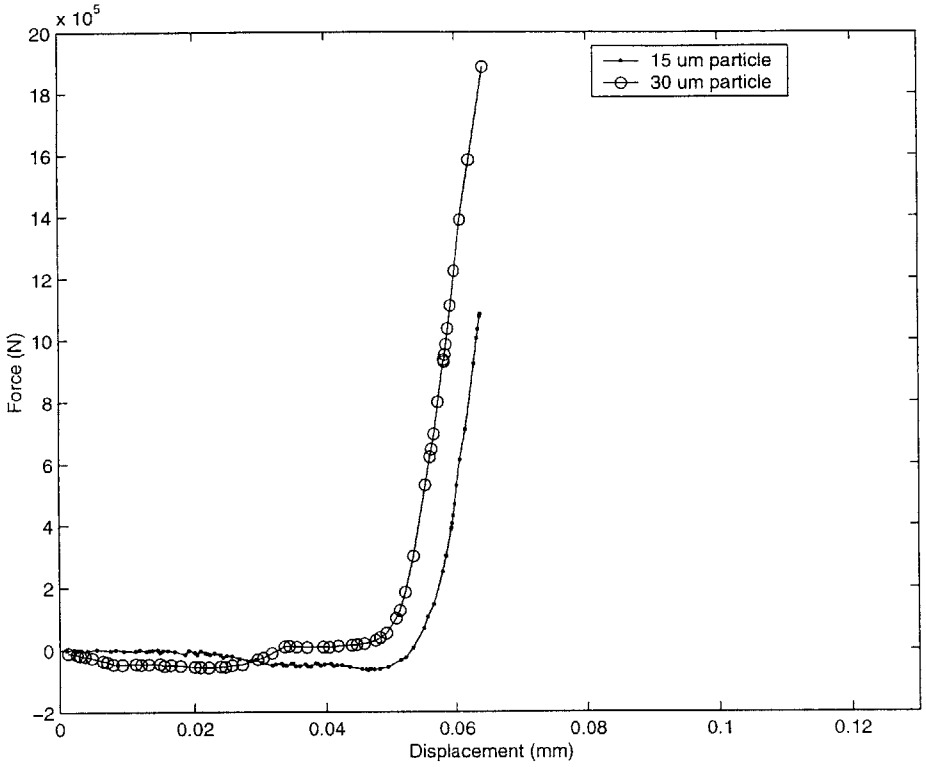

the fiber behind. The 15 μm particle would, however, continue to be stuck against the fiber until the force was increased significantly. It is expected that the force vs. displacement curve for the 15 μm particle would eventually level off but at a higher force than the curve for the 30 μm particle.

5.3.4 Tangential Fibers

Figures 5-36, 5-37 and 5-38 show the results for the particle mobility simulations with the tangential fiber configuration mesh. The fiber again clearly blocks the particles' motion. In Figure 5-36, the 5 μm particle is completely stuck against the fiber. With both larger size particles, however, the fiber starts to lift up and rotate about its opposite bottom corner as the particle comes close to and then contacts the fiber. As with the normal and longitudinal fiber configurations, the 30 μm particle is able to lift the fiber further from the surface than the 15 μm particle. The 30 μm particle is

Figure 5-36: Tangential Fibers and 5 μm Particle

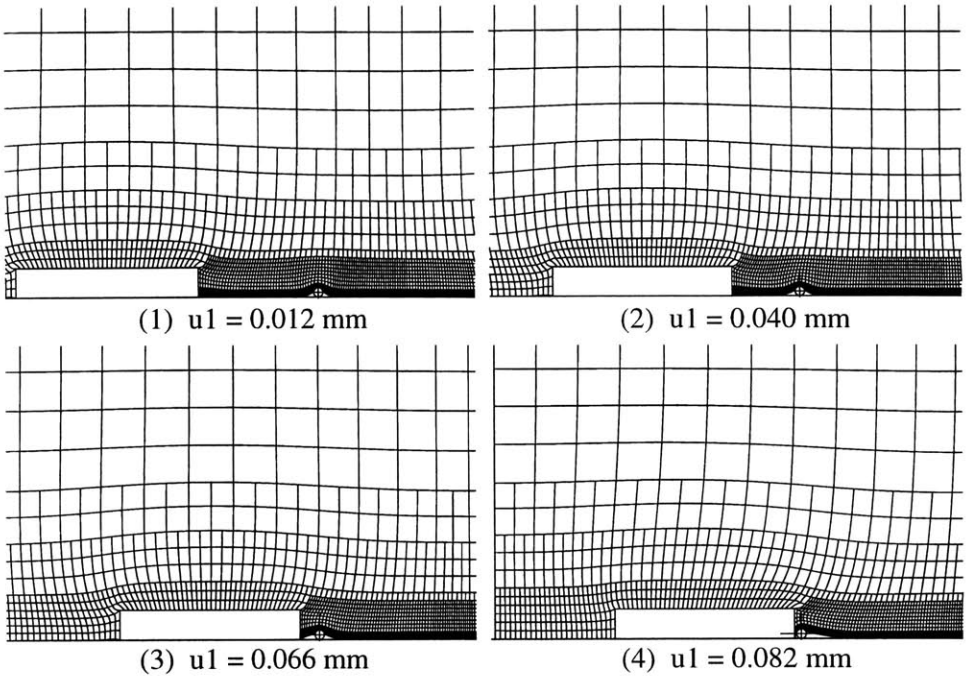

Figure 5-37: Tangential Fibers and 15 μm Particle

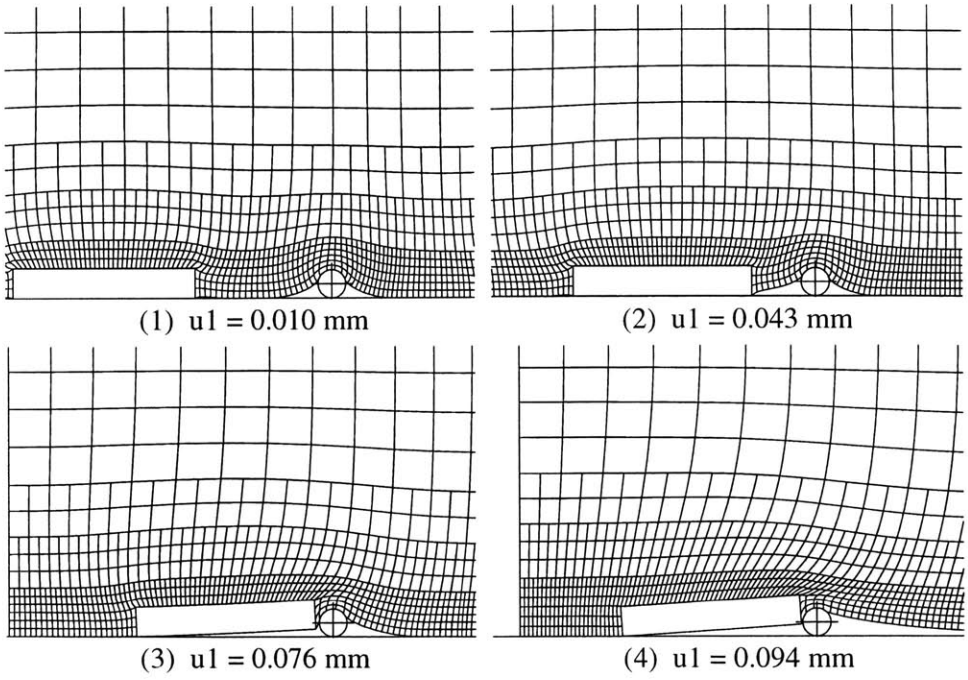

Figure 5-38: Tangential Fibers and 30 μm Particle

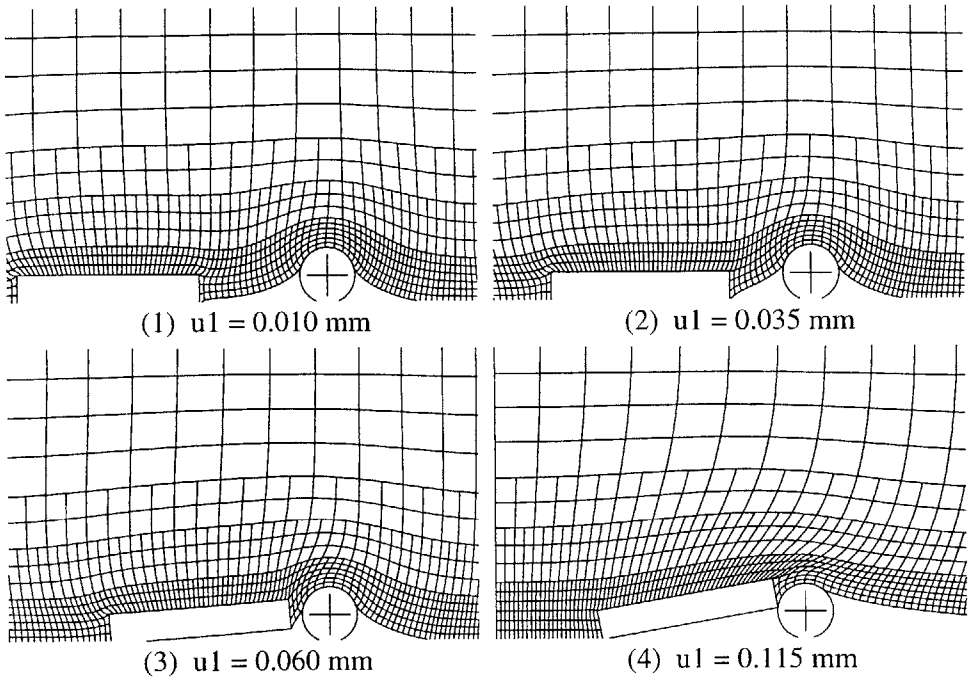

closer to moving under and past the fiber than the 5 and 15 μm particles.

Figure 5-39 shows the force vs. displacement curves for the three particle sizes. Again we see initially flat curves which climb at relatively constant rates once the particles approach the fibers. As in the normal and longitudinal fiber configuration simulations, the applied force begins to increase soonest with the 30 μm particle. The slopes of all three curves are only slightly steeper than the slopes of the curves for the normal fiber simulations. The relatively gradual upward slope of the tangential fiber curves is due to the fibers rotating in response to the pressure applied by the particles. Compressed along their entire length by the material above, the tangential fibers, however, do not rotate as easily as their normally oriented counterparts.

The slopes of the force vs. displacement curves increase as the particle size decreases. The fibers are most effective at inhibiting the motion of the small particles. We anticipate that the applied force for the 15 and 30 μm particles would eventually level off as the particles moved underneath and past the fiber while the applied force for the 5 μm particle would continue to increase.

Figure 5-39: Tangential Fibers: Reaction Force vs. Displacement

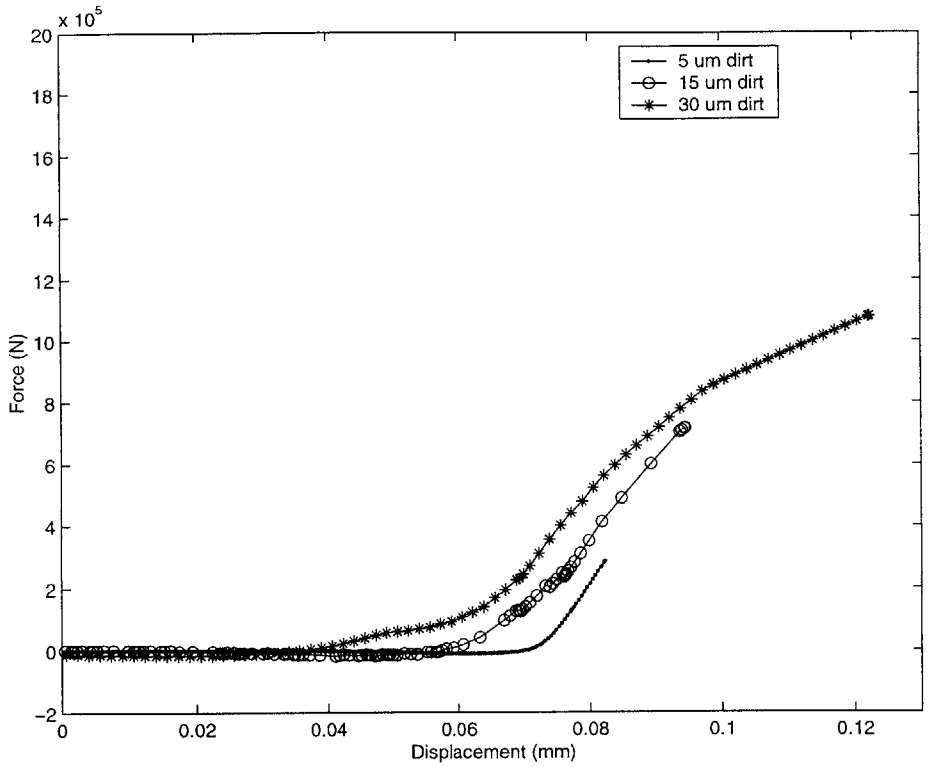

5.3.5 Summary

The fibers clearly inhibit the motion of particles between the elastomer and the bushing surface. The force required to move the particle increases as the particle approaches a fiber. The ability of a particular size fiber to block particle movement is a function of the size of the particle. Smaller particles become trapped against the fiber while larger particles produce deformations in the elastomer large enough to lift the fiber and pass beneath it. 5, 15 and 30 μm particles can all be considered to be of the same order of magnitude in size as the fibers. While the fibers are still quite effective at obstructing the motion of the 30 μm particle, we can infer that particles (or clusters of particles) a whole order of magnitude larger in size than the fibers would pass under them rather easily. The estimated critical cluster size of 100 μm would seem to approach that size. Furthermore in a real material, the fibers would not all be right at and perfectly parallel to the elastomer surface. In most cases, particles

significantly smaller than the fibers could find a way to move relatively unobstructed past the fibers.

5.4 Conclusions

The simulations in this chapter, while motivated by the track seal application, are meant to represent fundamental material behavior. At the same time, they do, not surprisingly, offer insight into the mechanisms at work during the abrasive wear of the track seal.

Many of the results in this chapter are notable for what they *didn't* show rather than what they did. The preliminary modeling of particles interacting with an elastomer block containing a single fiber several fiber diameters away from its surface indicates that the fibers do not significantly affect the stress field around the particle. The simulations with two parallel fibers at the surface of the elastomer block at normal, longitudinal, and tangential orientations show that the fibers actually increase the tensile stresses at the particle except in the case of closely spaced normal fibers. In the track seal lip, however, fibers are rarely oriented normal to the surface. When the seal lip is molded, the material flows into the mold in a direction parallel to the surface of the seal lip. Therefore, the fibers preferentially align parallel to the seal lip surface.

The simulations in sections 5.1 and 5.2 show little evidence that the addition of fibers increases the wear resistance of the track seal lip. Considering the wear process on a microscopic scale as a fatigue fracture phenomenon, we observe that the fibers do not reduce the tensile stresses in the matrix elastomer due to deformations caused by abrasive particles. This is, however, completely consistent with the experimental results. The aggressive wear rate and mechanism were shown to be the same for filled and unfilled polyurethane seals. The filled elastomer seals were superior only because they exhibited a longer break-in period.

The simulations presented in this chapter are representative of wear due to individual particles or small clusters. In chapter 2, we observed that the spacing of

the abrasion pattern formed by the advancing dirt front was much smaller than the typical fiber spacing. In complete agreement with the experimental results, the simulation results show the high tensile stress concentrations to be confined to areas much smaller than the fiber size and spacing. There is no evidence that fibers should reduce wear due to asperities in this size range. In the area between fibers, extensive microcracking and ridge formation should occur unaffected by the presence of the fibers.

The particle mobility simulations, however, do offer clues to how fibers extend the break-in period of the seal. By interfering with particles migrating within the contact band, fibers near or at the surface of the seal lip may discourage particles and small clusters from joining to form the critical size clusters that initiate aggressive wear. The fibers may also prevent some particles in a certain size range from entering the contact band at all. The simulations indicate that, as the particle size increases, it becomes easier for the particles to displace and pass underneath the fibers. The critical size clusters must therefore be large enough to be virtually unaffected by the presence of the fibers. The mechanism breaks down once the clusters reach this size, and aggressive wear occurs without interruption from the fibers.

Chapter 6

Effect of Fibers on the Contact Stress Distribution

We have shown in chapter 3 that fibers are present at or near the surface of the track seal lip. In chapter 5, we examined the effect that these fibers have on particle mobility and the stress concentration in the elastomer caused by the particle. Here we investigate how the presence of fibers near and at the surface of the elastomer changes the contact stress distribution between the elastomer and the rigid surface.

6.1 Fibers at the Surface of the Elastomer

In this section, two-dimensional plane strain meshes introduced in section 5.2 are compressed in the absence of the dirt particle. Specifically, the meshes with fibers at the normal, longitudinal, and tangential orientations spaced 7 particle diameters apart are compressed by 20%. The Arruda-Boyce Eight Chain model represent the material behavior of the elastomer. The contact stress profiles are compared with the constant result of -5.690 MPa for 20 % compression of an unfilled elastomer block.

6.1.1 Normal Fibers at the Surface

Figure 6-1 shows the results for the normal fiber configuration. We see sharp peaks in the contact stress reaching a maximum value of -530 MPa – a full order of magnitude greater than the contact stress of the unfilled elastomer block. The peaks occur at the fibers and are indicative of the high load bearing capacity of fibers in the normal configuration. The fibers bend slightly to the outside creating an asymmetric contact stress profile with maximums at the outer edges of the fibers.

Figure 6-1: Contact Stress: Normal Fibers at Surface

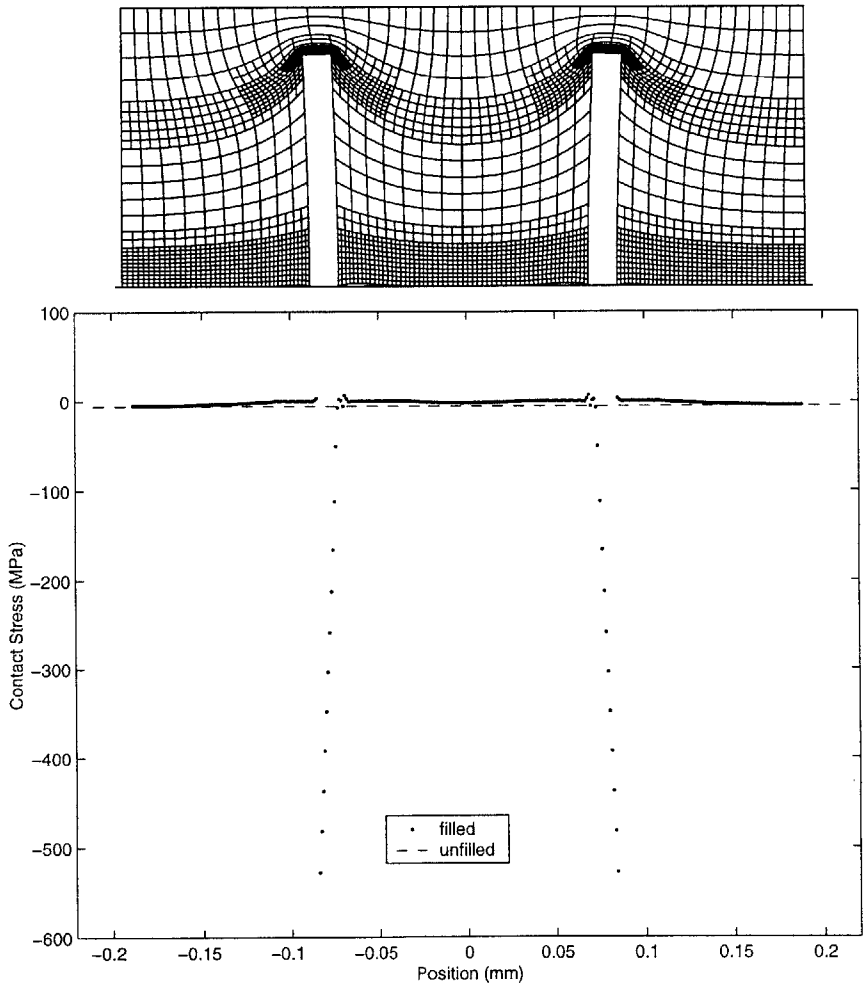

Figure 6-4 shows a blow up of a portion of the contact stress plot in Figure 6-1. We see regions on either side of the fibers where the contact stress is substantially

less than that of the unfilled elastomer block. In fact, immediately adjacent to fibers, the contact stress is zero. Close examination of the mesh in Figure 6-1 reveals that the elastomer matrix does not contact the rigid surface at all in these areas.

6.1.2 Longitudinal Fibers at the Surface

Figure 6-2 shows the results for the longitudinal fiber configuration. We again see

Figure 6-2: Contact Stress: Longitudinal Fibers at Surface

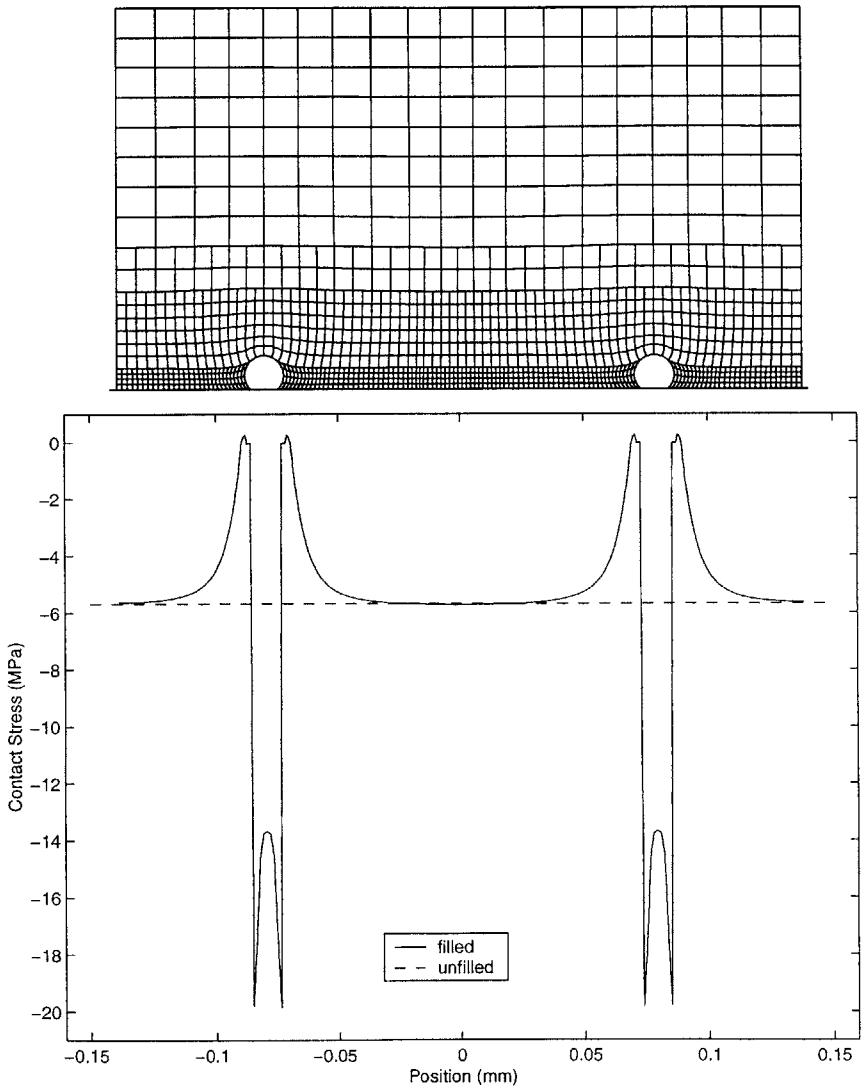

peaks in the contact stress at the fibers. With a maximum value of -20 MPa, the peaks are, however, far less imposing than those observed with the normal fibers.

Furthermore, the peaks are nearly symmetric with almost identical maxima at the inside and outside edges of the fibers. As with the normal fibers, the contact stress decreases to zero adjacent to the longitudinal fibers

6.1.3 Tangential Fibers at the Surface

Figure 6-3 shows the results for the tangential fiber configuration. In this case, the

Figure 6-3: Contact Stress: Tangential Fibers at Surface

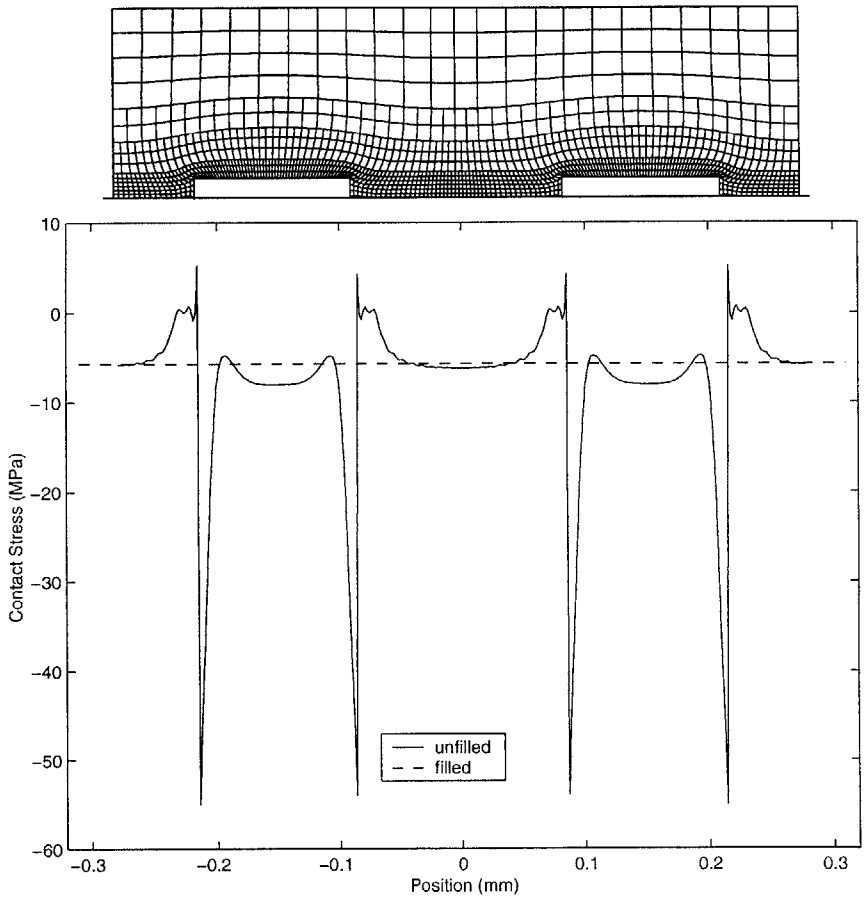

contact stress profile is rather complex. Two nearly identical peaks of -54 MPa and -56 MPa occur on the inside and outside ends of the fiber respectively. Along the interior of the fiber, the contact stress is only marginally greater than that for the unfilled elastomer block. The fibers appear to undergo simple bending in response to the load imposed by the surrounding elastomer. We again see regions at the ends

Figure 6-4: Contact Stress Profile Comparison

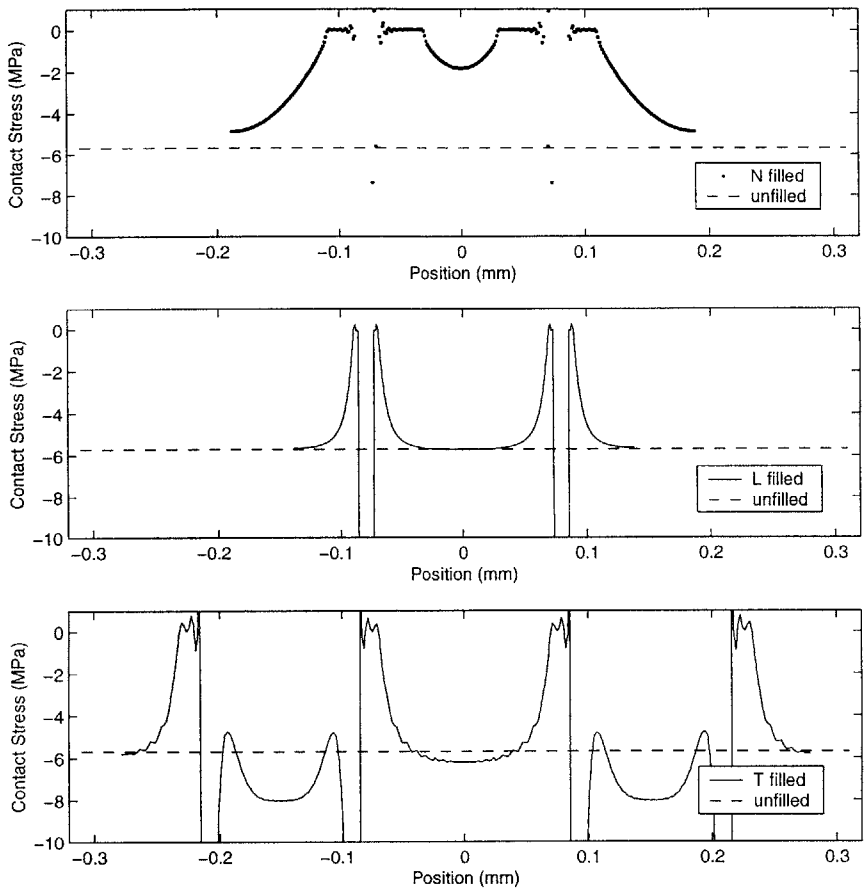

of the fibers where the contact stress is substantially less than that of the unfilled elastomer block.

6.1.4 Discussion

Figure 6-4 displays a comparison of the contact stress profiles of the three fiber orientations. We have shown previously that peaks in the contact stress exist at the fibers. The peaks indicate that the fibers are bearing a higher proportion of the applied load than the surrounding elastomer matrix. Regions with contact stresses greater than the value of an unfilled elastomer block must be balanced by regions with contact stresses less than the value of an unfilled elastomer block. We see the largest peaks with the normal fiber configuration. Figure 6-4 shows that, as required, the normal

fiber orientation plot also has the largest area of reduced contact stress. The normal fiber configuration is clearly the best at shielding the elastomer matrix from the applied load.

6.2 Fibers Below the Surface of the Elastomer

We have shown in the previous section that fibers at the surface of the elastomer have a significant effect on the nature of the contact stress distribution. However, in reality, fibers are rarely found right at the surface of a fiber-filled elastomer. Furthermore, unless they were oriented normally, fibers right at the surface would be quickly pulled out during the abrasive wear process. The analyses of chapter 3, however, indicated that fibers are present *near* the surface of the seal lip. In this section, we therefore investigate the effect that fibers a short distance below the elastomer surface have on the contact stress profile. Two-dimensional plane strain elements and the Arruda-Boyce Eight Chain model were again used to model the elastomer.

Since the seal lip molding process favors the longitudinal and tangential fiber orientations, we therefore concentrate on these configurations in this section.

6.2.1 Longitudinal Fibers Below the Surface

Figure 6-5 shows the results for the longitudinal fiber configuration. Simulations were run with fibers positioned both one fiber diameter (pictured) and one half fiber diameter from the elastomer surface. In both cases, we see a contact stress profile similar to that of the simulation with longitudinal fibers right at the surface – peaks in the contact stress below the fibers and regions of reduced contact stress adjacent to the fibers. Material beneath the fiber becomes trapped between the fiber and the rigid surface and is compressed to a higher stress level than the surrounding elastomer.

The buffer layer of elastomer present between the fiber and the rigid surface does, however, dampen the effect of the fiber on the contact stress profile. The symmetric peaks reach only -8.9 MPa for the fiber one diameter from the surface and -11.4 MPa for the fiber one half diameter from the surface. Furthermore, the regions of reduced

contact stress no longer decrease to zero contact stress. The minimum values are -5.1 MPa and -4.5 MPa for the fibers one diameter and one half diameter from the surface respectively.

Figure 6-5: Contact Stress: Longitudinal Fibers Below the Surface

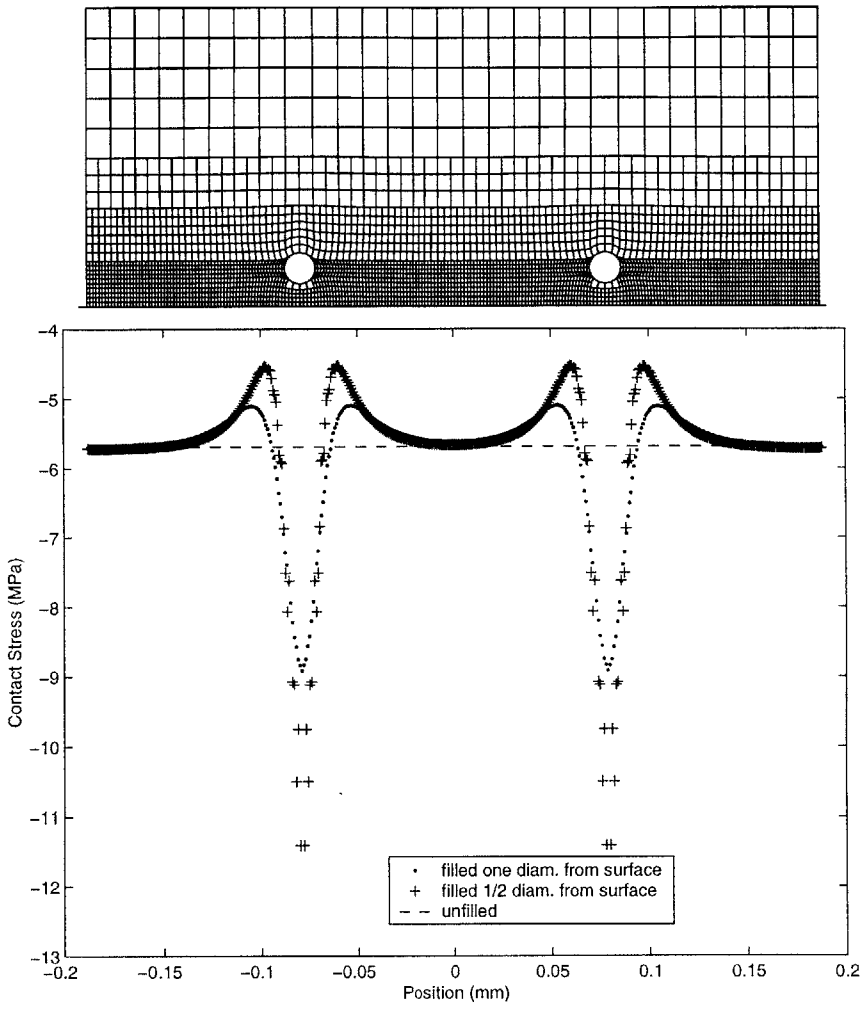

6.2.2 Tangential Fibers Below the Surface

Figure 6-6 shows the results for the tangential fiber configuration. Simulations were again run with fibers positioned both one fiber diameter (pictured) and one half fiber diameter from the elastomer surface. We once more see the pattern of peaks in the contact stress below the fibers and regions of reduced contact stress adjacent to the

Figure 6-6: Contact Stress: Tangential Fibers Below the Surface

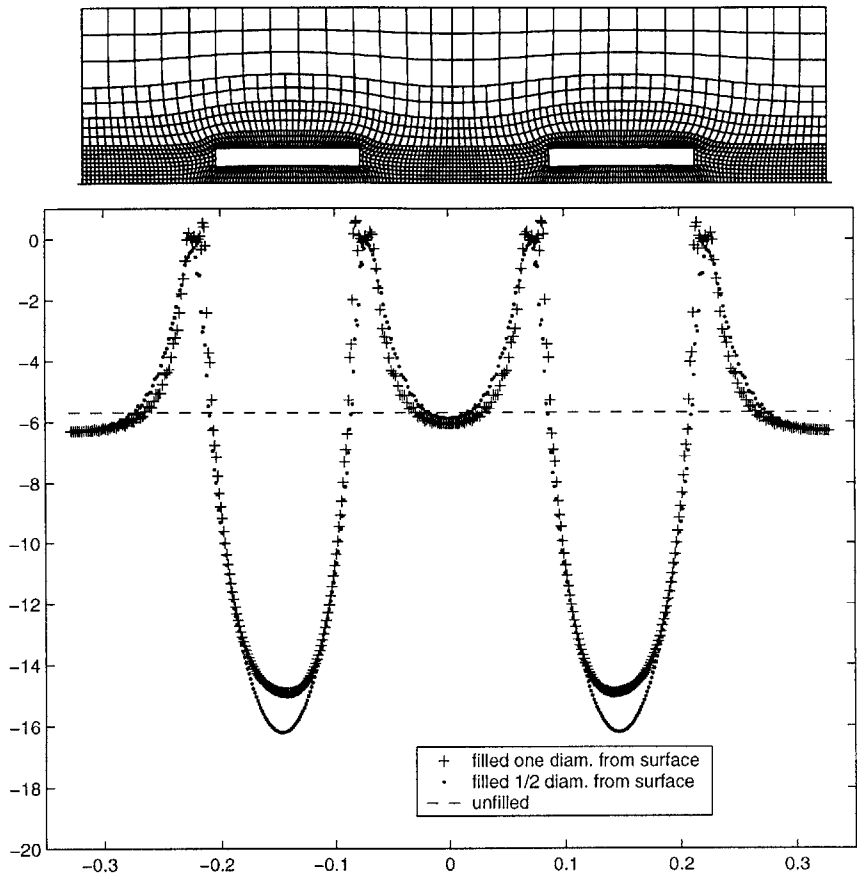

fibers. In contrast to the simulation with the fibers right at the surface, the contact stress profile, however, has symmetric peaks with the maximums at the fiber centers. The material under the centers of the fibers is more constrained and less able to flow in the 1-direction than the material near the ends of the fibers.

The layer of elastomer between the tangential fibers and the rigid surface only softens the effect of the fibers on the peaks in the contact stress profile. The maximums, -14.9 MPa and -16.2 MPa for fibers one diameter and one half diameter from the surface respectively, are significantly smaller than the maximums with the fiber right at the surface. Adjacent to the fibers, however, the contact stress still decreases to zero.

6.2.3 Discussion

The results of the simulations with fibers a short distance below the surface of the elastomer share many features with the results of the simulations with fibers right at the surface of the elastomer. While the thin layer of elastomer between the fiber and the rigid surface dampens it somewhat, the effect of the fibers on the contact stress distribution is still significant.

6.3 Three-Dimensional Modeling

Three-dimensional modeling of fibers in an elastomer matrix was also performed in order to validate the results of the two-dimensional plane strain simulations. While a reasonable approximation, the plane strain assumption used in the preceding sections creates unrealistic geometries and imposes unnecessary constraints on the deformation of the models. In the two-dimensional plane strain models, the fibers effectively extend infinitely in the 3-direction. Therefore, the normal and tangential fibers are actually infinitely long sheets of glass, and the longitudinal fibers are actually infinitely long cylinders. Furthermore, by definition, plane strain models do not permit deformation in the 3-direction. This restriction magnifies the stress in the 2-direction. A three-dimensional or axisymmetric unfilled elastomer block compressed by 20% exhibits a contact stress of only -3.70 MPa – almost 2 MPa less than that of the plane strain simulation.

6.3.1 Fibers Near the Surface

Model Description

Meshes of three-dimensional elastomer blocks with fibers one fiber diameter and one half fiber diameter from the surface were constructed. 20 node hybrid quadratic brick elements (C3D20H) were used. The symmetry of the geometry and the use of appropriate boundary conditions allowed only one quarter of the block and fiber to be modeled. The meshes are 200 μm tall and were compressed by 20%. The

Arruda-Boyce Eight Chain model was used to represent the material behavior of the elastomer.

Results

The deformed and undeformed meshes with a fiber one half diameter from the surface are pictured in Figure 6-8. The contour plots of the contact stress for both simulations

Figure 6-7: Deformed Mesh: 3D Fiber One Half Diameter Below Surface

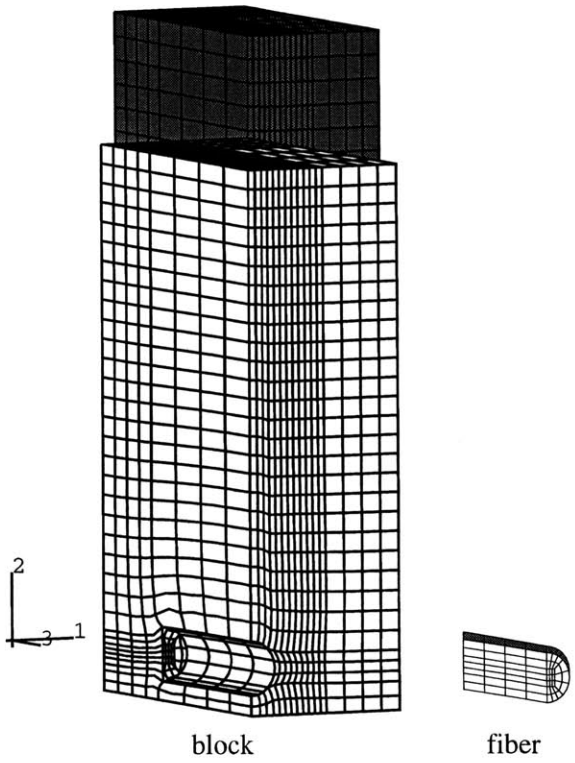

are shown in Figure 6-8. Regions of contact stress in excess of -3.70 MPa exist directly below the fibers in both cases. The contact stress reaches a maximum of -12.7 MPa with the fiber one half diameter from the surface and -8.9 MPa with the fiber a full diameter from the surface. We also observe areas of reduced contact stress adjacent to the fibers particularly at the ends of the fibers. The contact stress reaches a minimum of -0.73 MPa with the fiber one half diameter from the surface and -2.35 MPa with the fiber a full diameter from the surface.

Figure 6-8: Contact Stress: 3D Fibers Below Surface

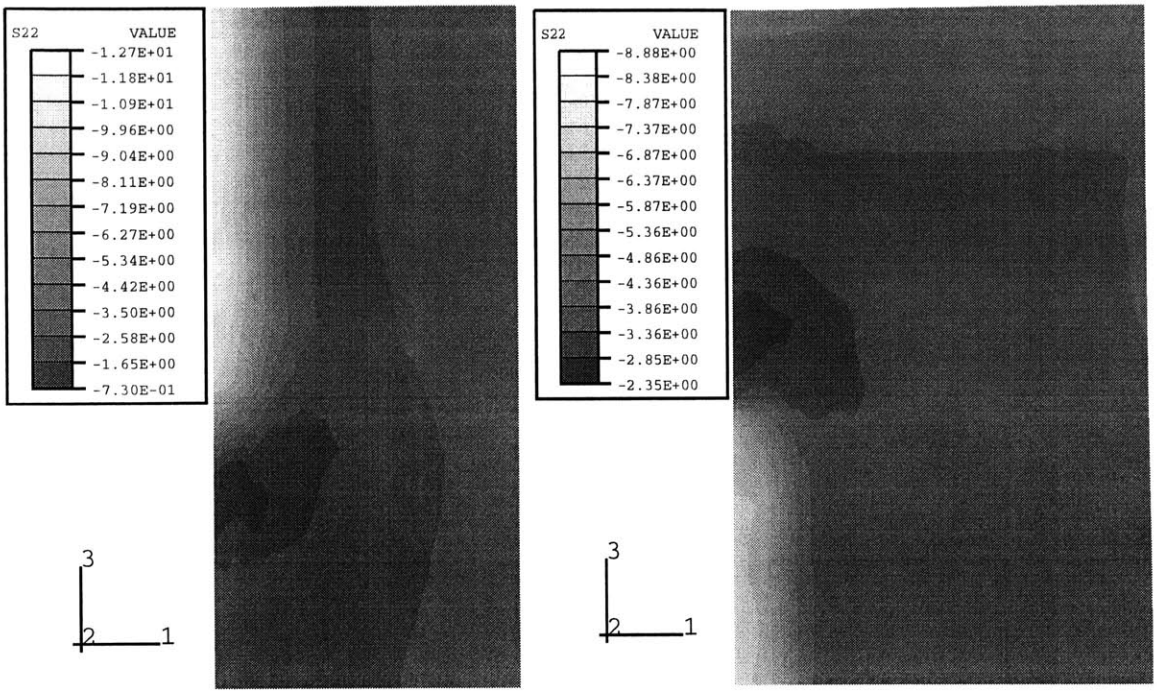

1/2 diameter from surface

one diameter from surface

Plotting the contact stress in two dimensions along lines parallel and perpendicular to the fiber axis enables us to compare the contact stress profiles with those of the two-dimensional simulations. Since only one quarter of the fiber was modeled, the data has been mirrored across its respective symmetry axes to produce plots for an entire fiber.

In Figure 6-9, the contact stress is plotted below the lengthwise center of the fiber along a line perpendicular to the fiber's axis (i.e. in the 1-direction). We see distributions very similar in shape to those of the two-dimensional longitudinal fiber simulations in Figure 6-5. A sharp peak exists below the fiber, and regions of reduced contact stress appear on either side of the fiber. As in the two-dimensional simulations, the fiber closer to the surface produces the more severe peak and the greater reduction in contact stress. Relative to the constant contact stress of the appropriate unfilled simulation, the magnitudes of the peaks in the contact stress of the three-dimensional simulations are very similar to those of the two-dimensional

Figure 6-9: Contact Stress: Perpendicular to Fiber Axis

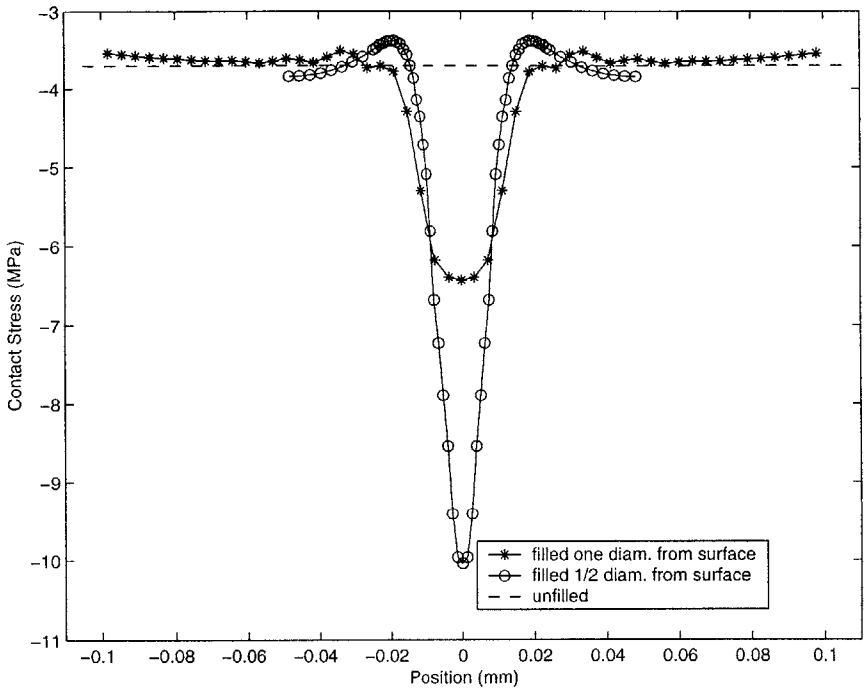

simulations. We see a 73.8% and 171% increase in the contact stress with the three-dimensional fibers one diameter and one half diameter, respectively, below the surface compared with a 56.8% and 101% increase with the two-dimensional longitudinal fibers the same distances below the surface. The relative magnitude of the reduction in contact stress, however, is somewhat less in the three-dimensional simulations than in the two-dimensional simulations.

In Figure 6-10, the contact stress is plotted along a line directly below and parallel to the centerline axis of the fiber. We see peaks below the fibers and areas of reduced contact stress at the fibers' ends similar to those observed in the two-dimensional tangential fiber simulations. With the fibers one half diameter from the surface, the peaks in the contact stress exceed the unfilled values by 185% in both the two and three-dimensional simulations. The peaks of the three-dimensional simulations, however, have broad, plateau-like shapes compared with the rather sharp peaks of the two-dimensional simulations. Furthermore, while moving the fiber another half diameter from the surface decreases the peak contact stress from -10.55 MPa to -6.85

Figure 6-10: Contact Stress: Parallel to Fiber Axis

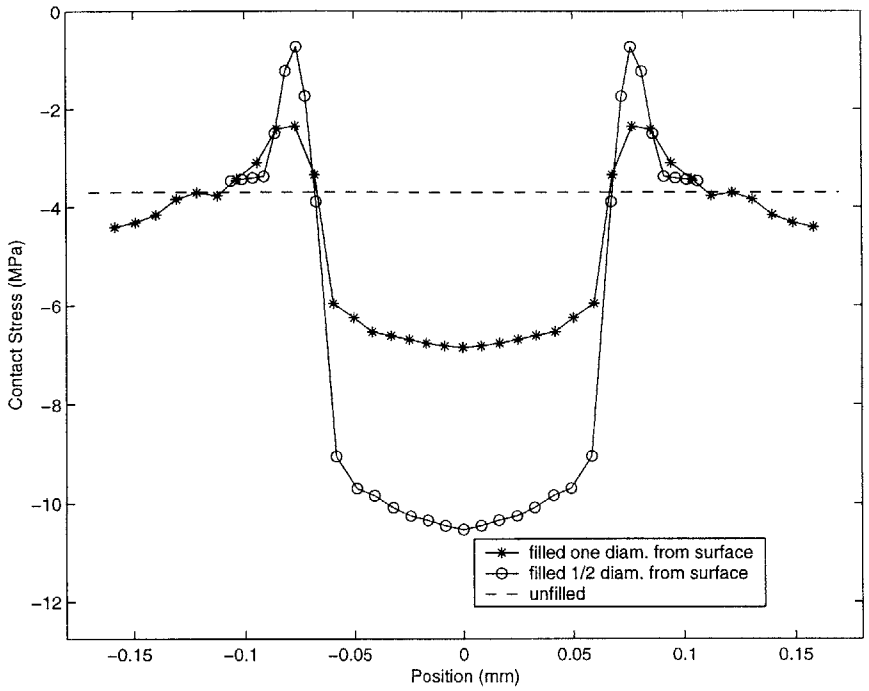

MPa in the three-dimensional case, it only decreases the contact stress from -16.2 MPa to -14.9 MPa in the two-dimensional case. Similarly, with the fibers one half diameter from the surface, the contact stress approaches zero at the fibers' ends in both simulations. With the fibers a whole diameter from the surface, however, the contact stress decreases to only -2.35 MPa in the three-dimensional simulation while still approaching zero in the two-dimensional simulation.

These discrepancies are due to the limitations of the plane strain model. Material flows much more uniformly and freely from under a finite cylindrical fiber than from under an infinite sheet. It escapes, not just at the ends, but also around the circumference of the fiber. In the three-dimensional case, increasing the distance between the fiber and the elastomer surface provides a much greater cross sectional area for material to flow through and away from the region under the fiber. The peak in the contact stress in this vicinity therefore decreases significantly since the material is compressed to a lesser degree. Balance of forces requires a correspondingly smaller decrease in the contact stress at the fiber's ends. In the two-dimensional

case, however, moving the fiber further from the surface does little to enhance the flow of material from under the fiber. The fiber effectively extends infinitely allowing material to escape only at its ends. Material remains essentially trapped between the fiber and the rigid surface and is compressed to a stress level approaching that of the simulation with the fibers one half diameter from the surface.

At the same time, the three-dimensional simulations expose the limitations of and verify the two-dimensional models. Both types of simulations obviously indicate that the fibers have a substantial effect on the contact stress distribution. The two-dimensional simulations, however, predict the fibers' effect on the contact stress profile perpendicular to the fiber axis extremely well but, particularly as the fibers move further from the surface of the elastomer, tend to overpredict their effect on the contact stress profile parallel to the fiber axis.

6.3.2 Fibers Further From the Surface

Fibers are certainly not always parallel to and within one fiber diameter of the surface of an elastomer. A three-dimensional cubic mesh was therefore created with a fiber at its center aligned along the cube diagonal. The size of the cube is such that the shortest distance between the fiber and the elastomer surface is 100 μm. In this case, eight node hybrid linear brick elements (C3D8H) were used with the Arruda-Boyce Eight Chain model again representing the material behavior of the elastomer. As shown in Figure 6-11, the cube was compressed by 20%.

The contour plot in Figure 6-12 shows the contact stress distribution for the simulation. With a maximum and minimum of -3.90 MPa and -3.66 MPa respectively, the contact stress hardly varies from the unfilled value of -3.70 MPa. Fibers a substantial distance from the elastomer surface clearly do not have a significant effect on the nature of the contact stress distribution.

Figure 6-11: Diagonal Fiber 100 μm from Surface

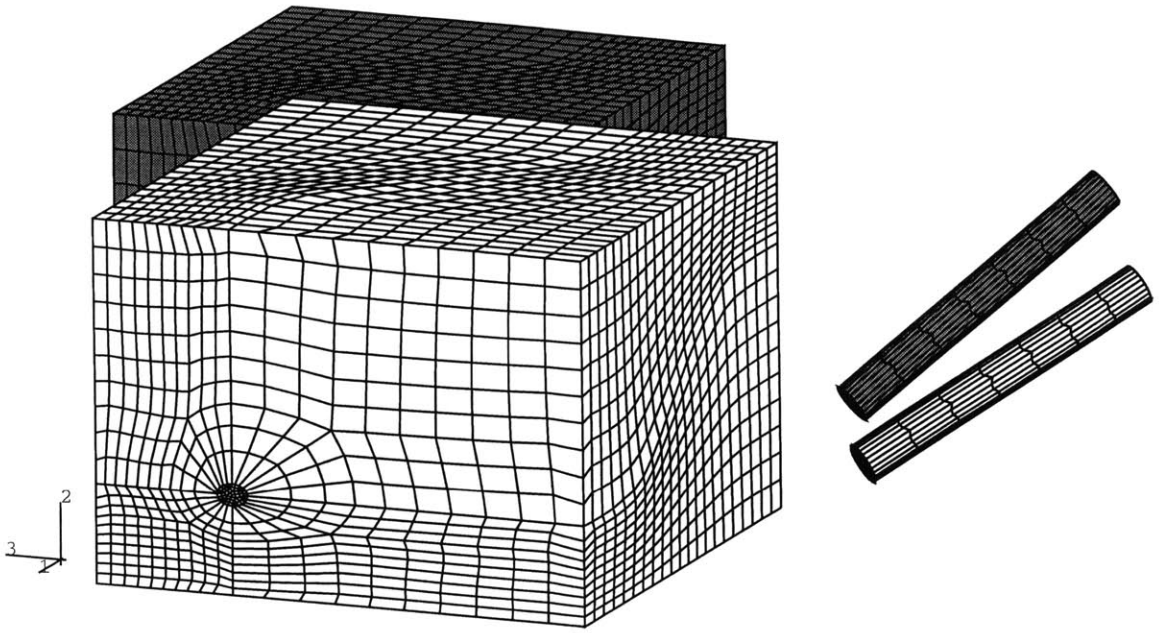

Figure 6-12: Contact Stress: Diagonal Fiber 100 μm from Surface

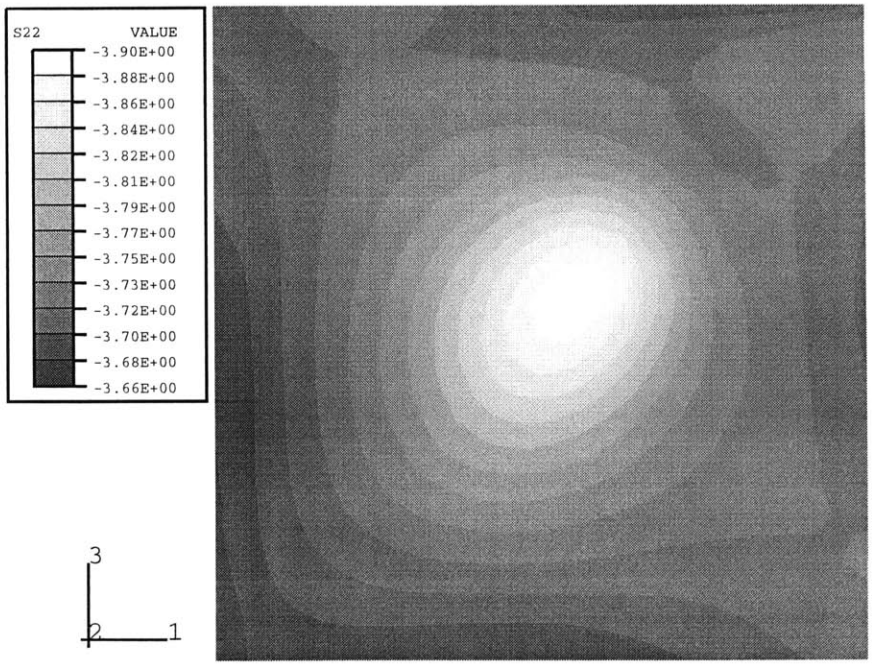

6.4 Conclusions

The simulations in this section prove that fibers near or at the surface of the elastomer significantly alter the nature of the contact stress distribution between the elastomer and the rigid surface. Compared to the constant value obtained when an unfilled elastomer is compressed by an equal amount, the contact stress increases in areas directly underneath the fiber and decreases in regions near the edges of the fiber. From these results, we propose several possible mechanisms by which fibers may improve the wear resistance of the elastomer.

The experimental results show that adding fibers to the track seal lip extends the life of the seal, not by changing the aggressive wear rate or mechanism, but by extending the break-in period. The end of the break-in period is marked by the formation of critical size clusters. It follows that the fibers must prevent particles from entering the contact band and/or prevent particles in the contact band from clustering.

By reducing wear due to small particles, the fibers may prevent larger particles and more small particles from entering the contact band. We showed, particularly in Section 6.1, that the fibers act as load bearers and reduce the force on the surrounding elastomer. Small, micron size particles are able to enter the contact band long before any wear is apparent. The load bearing capability of the fibers reduces the normal force and, thus, the frictional force on the elastomer as it shears back and forth over these small particles. Lowering the frictional force should decrease the wear rate. A second possible mechanism is that fibers reduce the frictional force and, in turn the wear, by increasing the lubrication of the seal lip/bushing interface. The lower contact pressure adjacent to the fibers should allow more lubricant to accumulate in these areas. As discussed in chapter 3, CCD pictures of unworn seal lip contact bands show many more air bubbles with filled elastomer seal lips than with unfilled elastomer seal lips. It is presumed that, if more air is able to exist in the contact band, then more lubricant should also be present. Furthermore, Ayala's laser-induced fluorescence studies have quantitatively shown that the oil layer thickness is roughly

50% greater with the filled elastomer seal lips than with the unfilled elastomer seal lips [6]. If we assume a certain concentration of particles is required in the contact band for clustering to begin, these two mechanisms would extend the break-in period by slowing the rate of particle ingestion.

A third possible mechanism is that, as proposed in chapter 5, the fibers do not necessarily reduce wear at all but increase the time required for particles to form the critical size clusters which initiate aggressive wear. In this case, however, the mechanism could work without the particles actually contacting the fibers. The uneven contact stress distribution produced by the fibers at or near the surface of the elastomer would seem to impede particle motion between the seal lip and bushing. The contact pressure spikes sweeping back and forth as the seal oscillates may prevent particles from congregating into clusters and break up small clusters before they reach the critical size. The areas of high contact pressure might also slow the ingestion of particles temporarily keeping them on the outer fringes of the contact band. Eventually, however, the concentration of particles in the contact band becomes so high that clustering is inevitable. Aggressive wear then begins.

After presenting more experimental results in chapter 7, we will speculate further on the mechanisms at work.

Chapter 7

Track Seal Experiments with Well-Characterized Dirt

In all experiments described in chapter 2, the abrasive slurry was mixed according to the Caterpillar recipe of equal parts by volume of fire clay and bank sand. In this chapter, we show the results of experiments performed with a "well-defined" slurry. Tests were run with clay alone, sand alone, and three sizes of Arizona test dust (A.T.D.). Analyses were conducted to determine the size distribution of particles in each of the slurries. Conclusions are drawn about the seal lip wear mechanism from the wear results as a function of particle size.

7.1 Dirt Particle Size Analysis

Tests were performed with sand, clay, and Arizona test dust in 0-3 μm, 5-10 μm, and 10-20 μm particle size ranges. The Arizona test dust was procured from Powder Technology Inc. (PTI). PTI guaranteed that, by volume, 96% of the 0-3 μm test dust and 90% of the 5-10 μm and 10-20 μm test dust fell within the stated size ranges. PTI conducted particle size analyses on all three samples before shipping. Samples of the mud mix, sand, and clay were sent to PTI for particle size analysis.

PTI used two different techniques to determine the distribution of particle sizes in the samples. With both methods, the sample is first put into solution in order to

prevent particle clustering. The Coulter multisizer analyzer optically measures each individual particle's volume and reports an equivalent spherical diameter. The Coulter method only detects particles with equivalent diameters in the 0.7-100 μm range. The Microtrac analyzer uses laser diffraction to determine an equivalent spherical diameter for each particle. It has the capability to measure particles with equivalent diameters ranging from 0.1 μm to 1000 μm. Both techniques calculate and report as a distribution the volume fraction in the entire sample of particles in very small size ranges.

Figure 7-1 shows the particle size distribution for the standard mud mix (less the water) devised by Caterpillar and used in all experiments in chapter 2. The Microtrac method was the only feasible method of measurement due to the wide range of particle sizes in the sample. By weight, the sample was approximately 56.9% sand, 42.7% fireclay, 0.3% Cabosyl, and 0.1% salt. We see particles ranging in size from 0.6 μm to 500 μm. There are two peaks in the distribution. The first represents the clay particles, and the second represents the sand particles. The mean value is 88.9 μm, and the median value is 29.5 μm.

Figure 7-1: Mud Particle Size Distribution

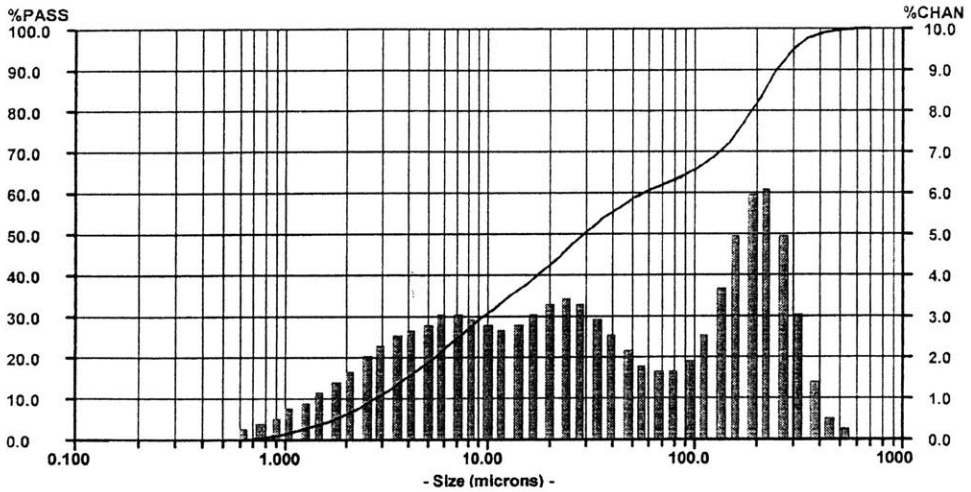

The standard mud mix constituents arrived at MIT in one container but separated – the sand on the top and the clay on the bottom. The Cabosyl and salt were sprinkled

on top of the sand but will be neglected due to their small mass fractions. Separate samples of sand and clay were also sent to PTI for particle size analysis.

The sand particle size distribution is displayed in Figure 7-2. The vast majority of the sand lies in the 40- 500 μm range. The mean value is 197.5 μm, and the median value is 197.2 μm.

Figure 7-2: Sand Particle Size Distribution

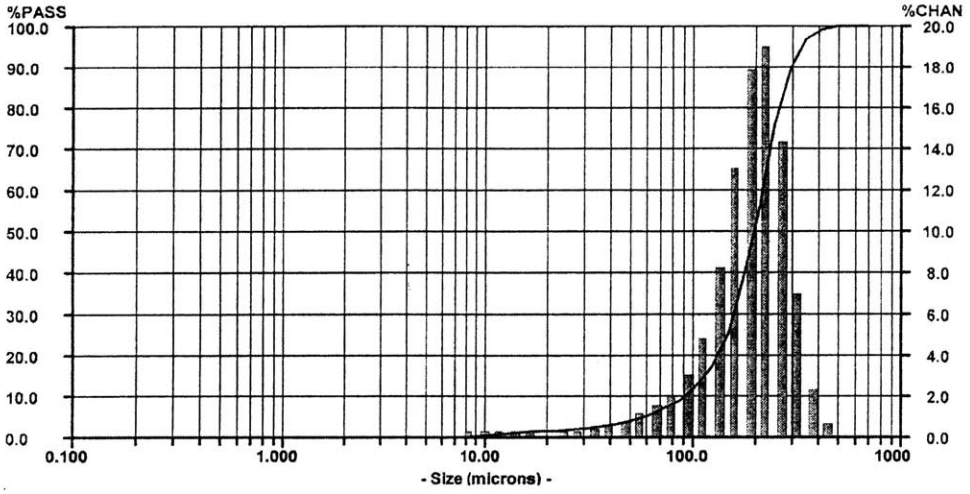

A Microtrac analysis of the clay sample is shown in Figure 7-3. The clay consists

Figure 7-3: Microtrac Analysis of Clay Particle Size Distribution

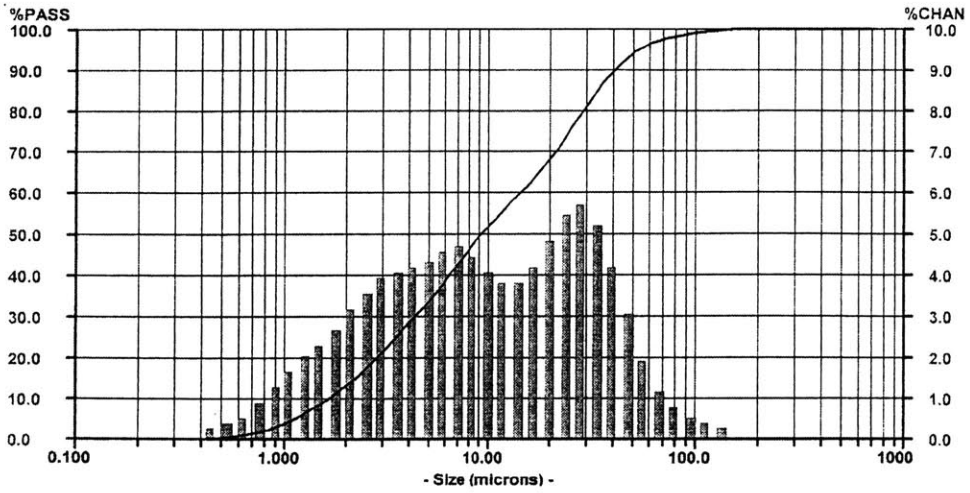

of particles from 0.4 to 100 μm in effective diameter – a much larger range than

Figure 7-4: Coulter Analysis Clay Particle Size Distribution

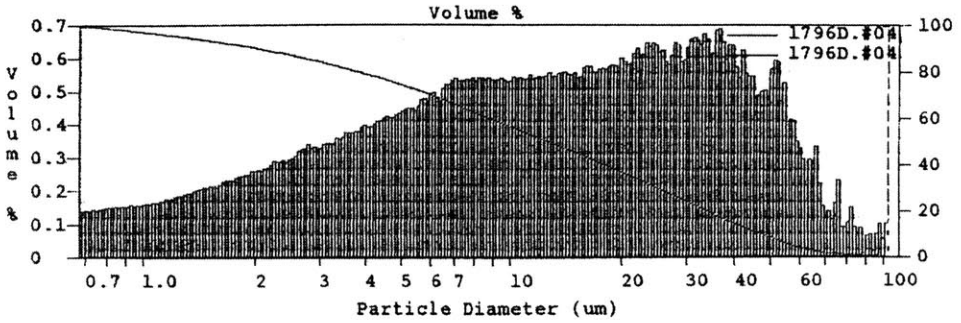

Figure 7-5: 10-20 μm A.T.D. Particle Size Distribution

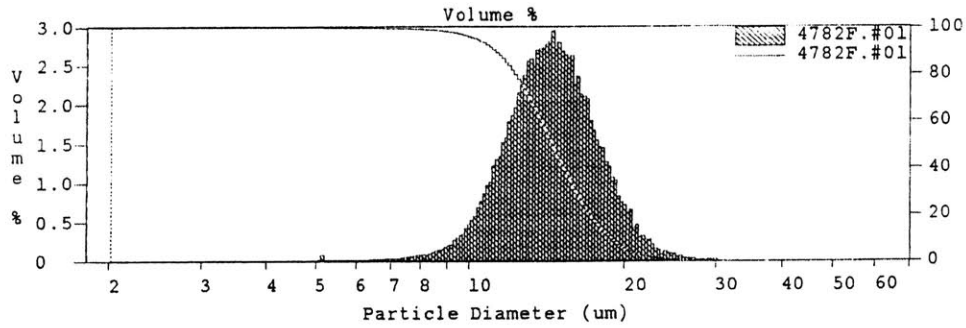

expected. The mean value is 17.1 μm, and the median value is 9.3 μm. In order to validate this surprising result, and for comparison with the Arizona test dust, a Coulter analysis was also performed on the clay sample. The particle size distribution measured with the Coulter technique in Figure 7-4 agrees relatively well the Microtrac result. The mean value is 11.0 μm and the median value is 12.5 μm.

PTI provided Coulter analyses of the three sizes of Arizona test dust. Figure 7-5 shows the particle size distribution of the 10-20 μm dirt. The mean and median values of 14.3 μm and 14.4 μm, respectively, are close to the center of the size range. The particle size distribution for the 5-10 μm dirt is displayed in Figure 7-6. Again the mean and median values, identically 7.2 μm, are right around the center of the advertised size range. Figure 7-7 shows the results of the Coulter analysis for the 0-3 μm dirt. In contrast to the particles in the 10-20 μm and 5-10 μm dirt, the particles in the 0-3 μm dirt are biased towards the small end of the size range. The mean and

Figure 7-6: 5-10 μm A.T.D. Particle Size Distribution

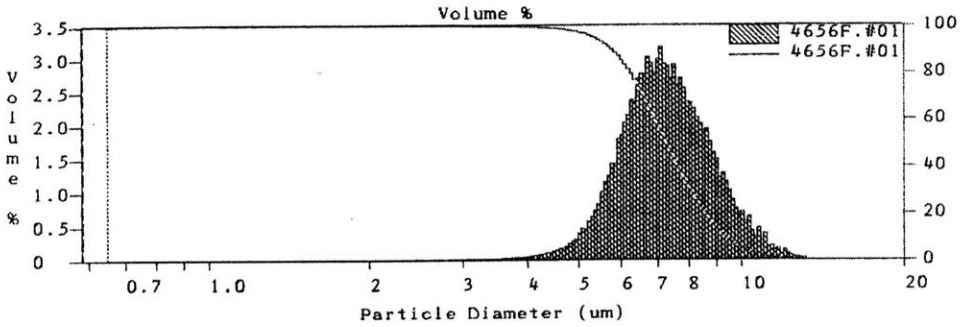

Figure 7-7: Coulter Analysis of 0-3 μm A.T.D. Particle Size Distribution

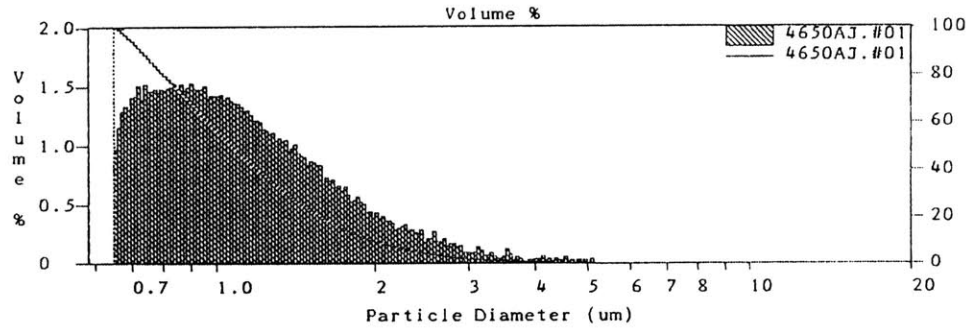

Figure 7-8: Microtrac Analysis of 0-3 μm A.T.D. Particle Size Distribution

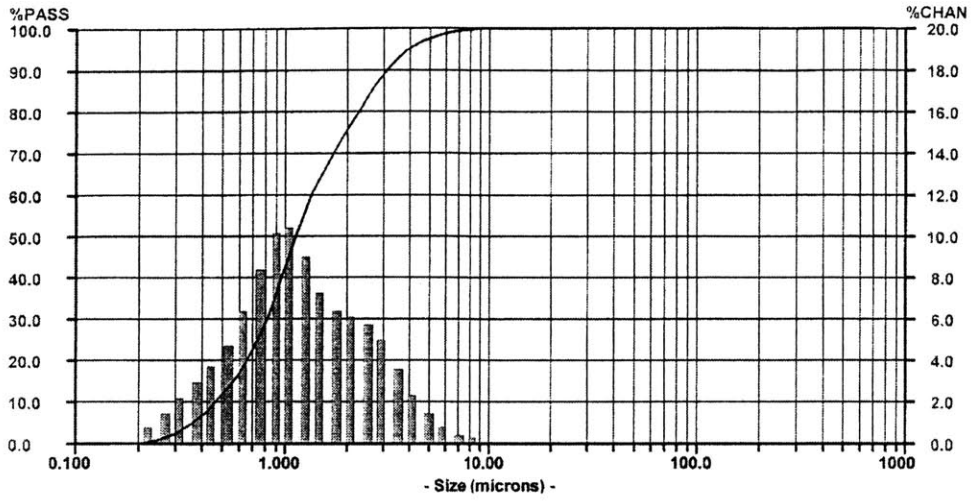

median values are both 1.1 μm. One limitation of the Coulter analysis, however, is that it cannot detect particles less than 0.7 μm in size. A Microtrac analysis of the 0-3 μm dirt was therefore also performed to see just how small the particles could be. Figure 7-8 indicates that the Microtrac analyzer detected particles as small as 0.2 μm in equivalent diameter. The median value, however, was still 1.1 μm.

7.2 Experimental Results

The five different sizes of dirt described in section 7.1 were separately mixed with water to create the abrasive slurries used in the track seal experiments. For each dirt size, water was added while stirring the mixture until the slurry's consistency was similar to that of the standard mud mix. Since, for each dirt type, all particles were similar in size, the water percolated through the dirt very quickly. The slurries therefore required constant mixing in order to maintain their consistency. For this reason, the slurries were applied with a scoop rather than a squeeze bottle. In every other way, the experiments were identical to experiments described in chapter 2.

Figure 7-9: Seal Wear Data: Unfilled Elastomer Seal with Sand

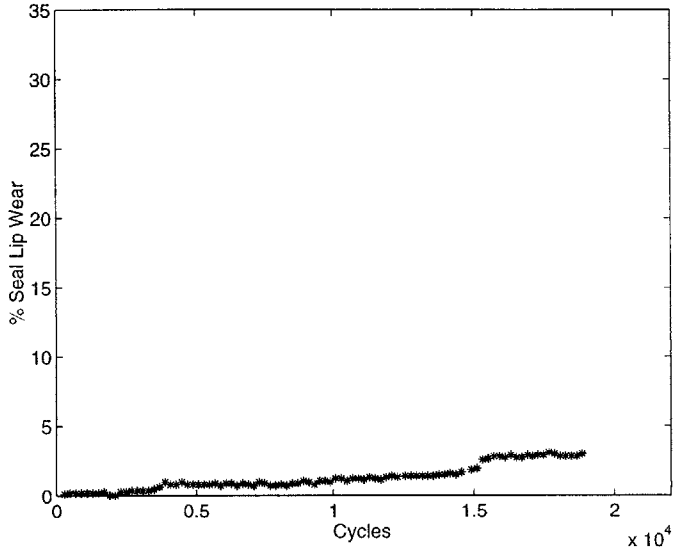

7.2.1 Experiments with Caterpillar Dirt

As mentioned in section 7.1, Caterpillar provided MIT with dirt separated into sand particles and clay particles. Samples of sand and clay were mixed separately with water to form well-defined slurries.

Sand

One test was run with an unfilled elastomer seal and an abrasive slurry composed of only sand particles. The wear curve in Figure 7-9 indicates that very little wear had occurred when the test was terminated after over 18,500 cycles of operation. For the most part larger than 100 μm, the sand particles are virtually unable to penetrate the seal lip contact band.

The wear sequence in Figure 7-10 demonstrates that the sand particles do wear the outer edge of the seal lip slightly. The slurry is first added at 410 cycles. The white indentations at the edge of the seal lip are particles entering the contact band. At 4202 cycles, a dark band forms at the outer edge of the seal lip. The dark band indicates that the seal has been roughened in this area. The rough surface reflects less light than the smooth unworn seal lip surface further inward and therefore appears

Figure 7-10: Seal Wear Sequence: Unfilled Elastomer Seal with Sand

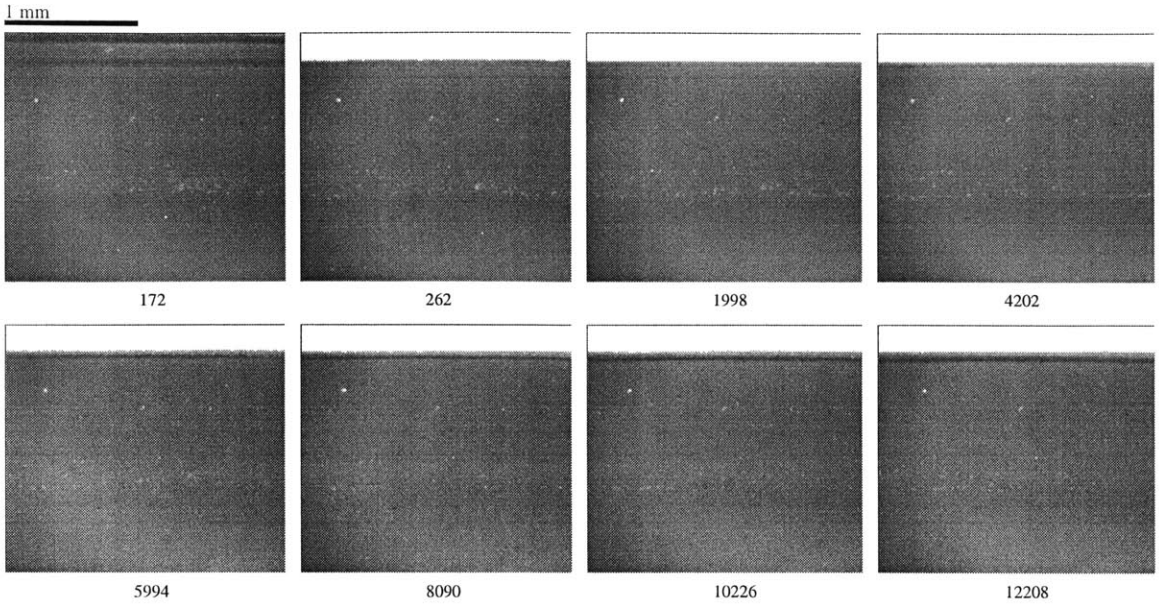

darker. A thin, cloudy stream of particles or small clusters overlaps the outer portion of this dark band. The band advances very slowly, yet noticeably, between 4202 and 12,208 cycles.

Figure 7-11 shows an SEM picture of the outside edge of the seal lip after 18,500 cycles of operation. Wear has clearly occurred over the outer 50 μm of the contact band. The wear pattern is, however, much different than that observed in chapter 2. We see narrow tracks or microcuts parallel to the sliding direction rather than periodic ridges at right angles to the sliding direction. It appears that hard, sharp sand particles stick to the seal's running surface and plow these tracks in the seal lip.

Clay

Two tests were run with both filled and unfilled elastomer seals and an abrasive slurry of just clay particles. Failure did finally occur with both type seals, but the break-in periods were much longer than the break-in periods with the standard mud mix slurry. The wear curves are shown in Figures 7-12 and 7-13.

The relevant data is summarized in Table 7.1 The filled elastomer seals exhibit,

Figure 7-11: SEM of Edge of Seal Lip Worn by Sand Slurry

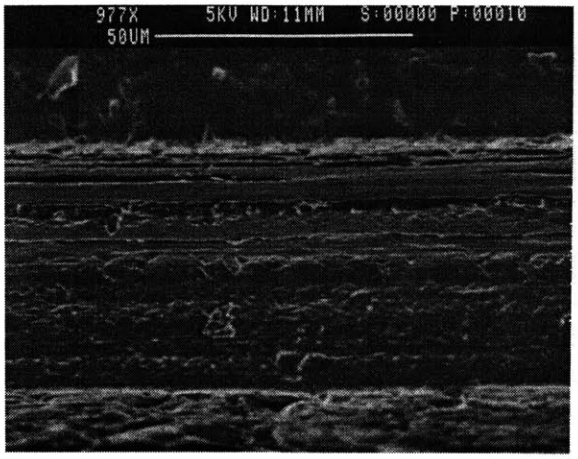

Figure 7-12: Seal Wear Data: Unfilled Elastomer Seal with Clay

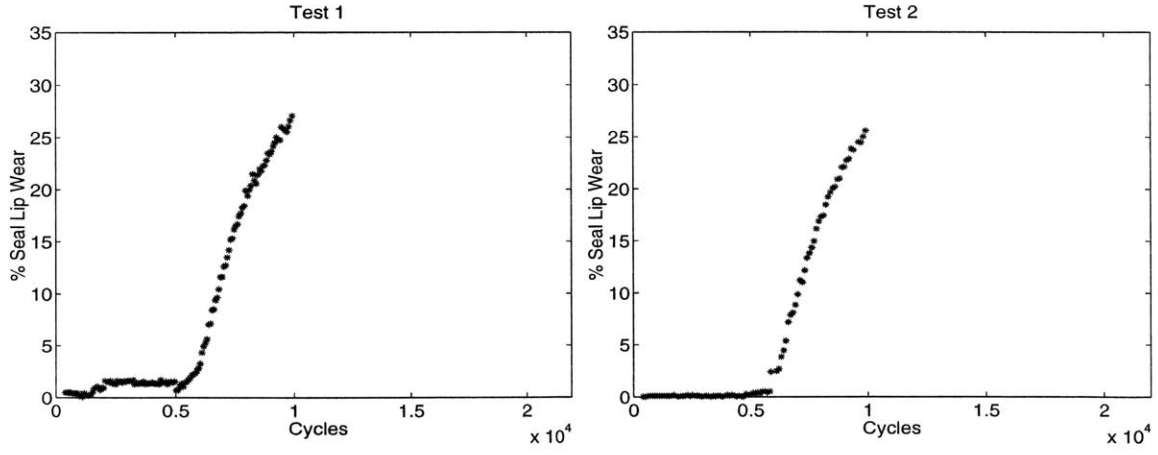

Figure 7-13: Seal Wear Data: Filled Elastomer Seal with Clay

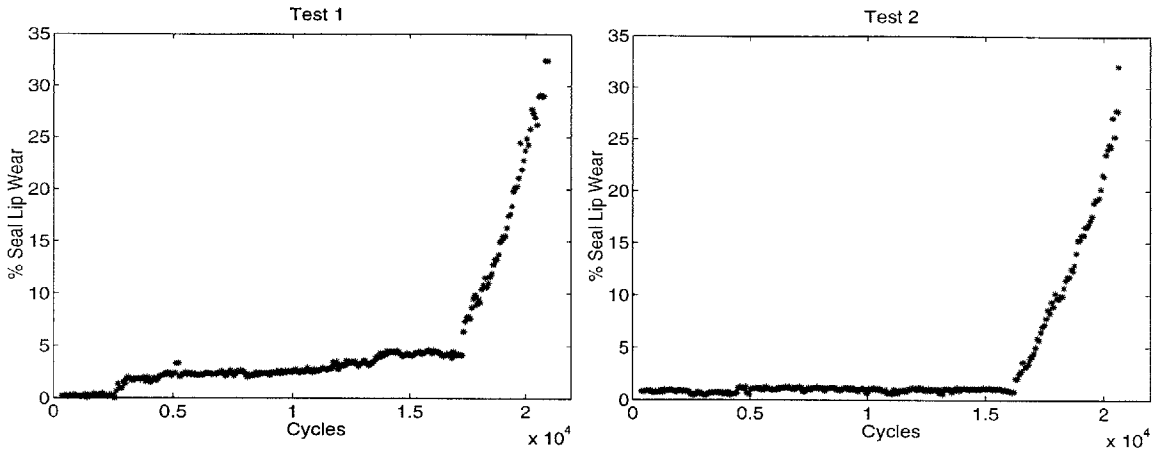

Table 7.1: Summary of Seal Wear Tests with Clay

	Break-In Period (cycles)	Aggressive Wear Rate (mm/cycle $\times 10^{-4}$)
Unfilled Test 1	4968	3.54
Unfilled Test 2	5400	3.65
Unfilled average	5184	3.60
Filled Test 1	16850	3.55
Filled Test 2	15816	3.63
Filled average	16333	3.59

on average, a break-in period three times that of the unfilled elastomer seals. Once wear begins, however, the aggressive wear rates of the filled and unfilled elastomer seals are virtually identical.

Figure 7-14 shows the wear sequence for the unfilled elastomer seal (test 1). The slurry is added after 410 cycles. No wear is visible until approximately 5785 cycles when a small cluster develops in the upper right hand corner of the frame. Less than 300 cycles later, at 6010 cycles, debris and vague clusters are everywhere in the outer 20% of the contact band. Distinct, sizeable tear-shaped clusters form at 6220 cycles, but a cloudy mass of particles and small clusters still exists in the background. The clusters increase in size and penetrate further into the contact band at a linear rate

Figure 7-14: Seal Wear Sequence: Unfilled Elastomer Seal with Clay (Test 1)

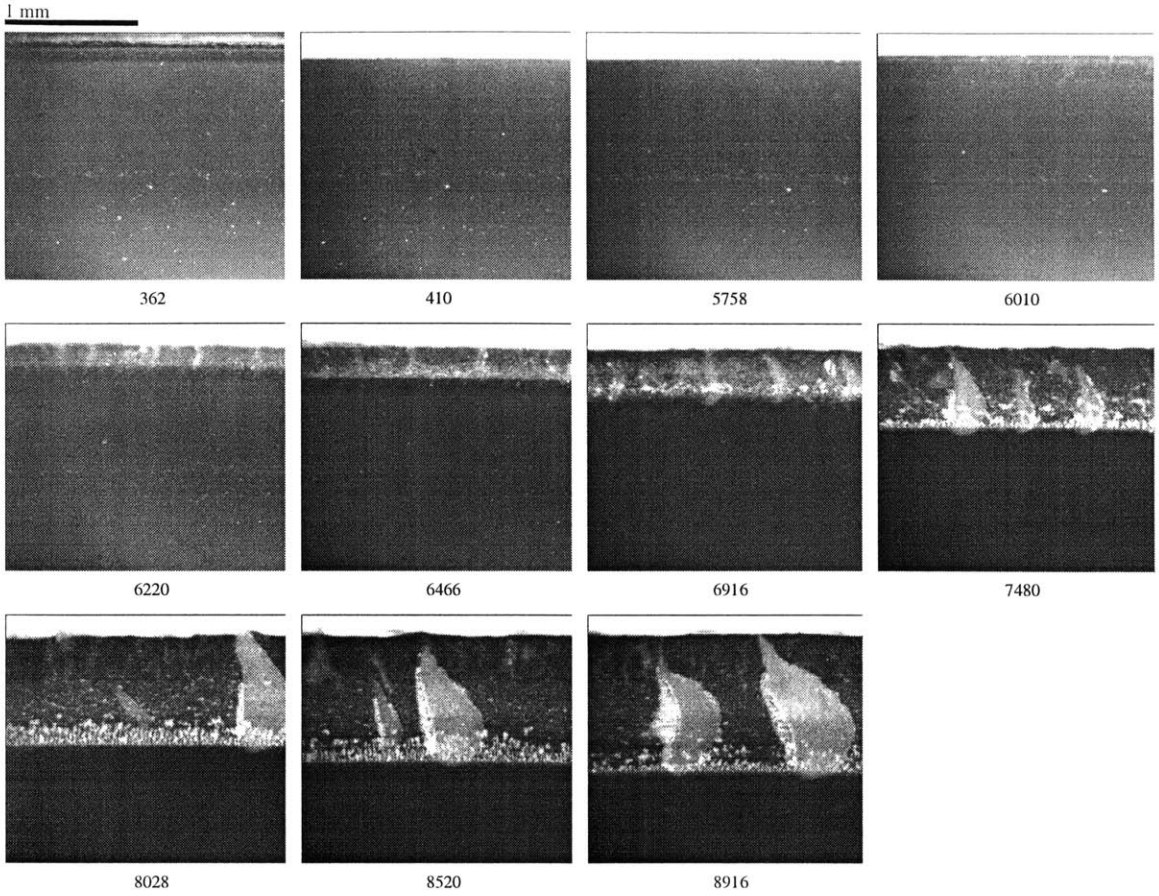

from 6220 through 8916 cycles. By 7480 cycles, most of the particles and smaller clusters have been swallowed up by the largest clusters.

Particularly noticeable in this sequence in cycles 6220 through 6916 are the three different regions of the contact band. The outermost region includes the area covered by the cloudy, gray mass of particles which have not yet clustered. The edge of this mass forms a nearly straight line. Overlapping and extending slightly further into the contact band is a region darker than the third region, the rest of the seal lip. The clusters extend to the edge of this second region, but the mass of particles does not. The clusters are pushing further into and wearing the contact band, opening it up for the mass of loose particles.

The wear sequence for the filled elastomer seal (test 1) is displayed in Figure 7-15

The slurry is added after 416 cycles. At 2446 cycles, a thin layer of debris penetrates

Figure 7-15: Seal Wear Sequence: Filled Elastomer Seal with Clay (Test 1)

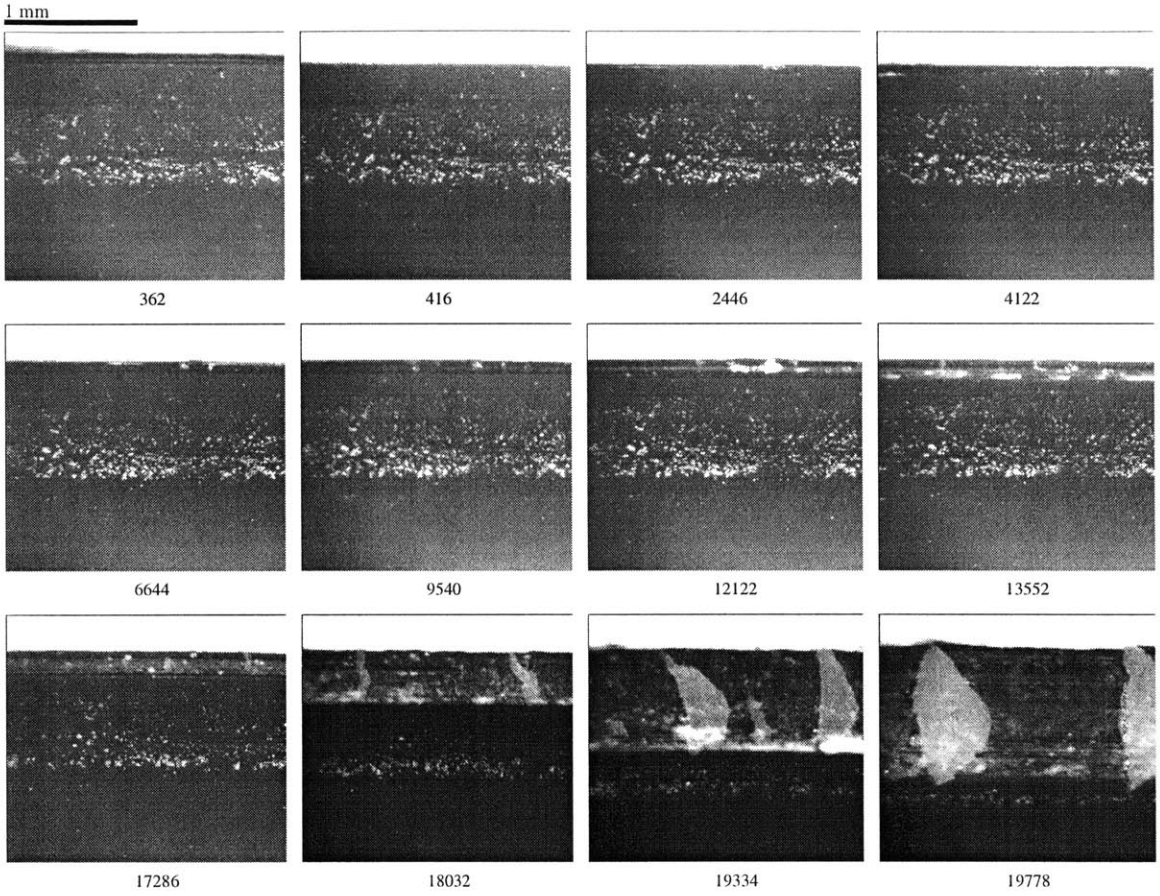

the contact band. From cycles 4122 through 17286, clusters form, break up, and re-form but do not advance or grow in size significantly. At 17,286 cycles, the first sizeable tear-shaped clusters form and aggressive wear begins. These clusters advance and rapidly grow in size until they span the entire width of the contact band.

The clustering behavior with the filled and unfilled elastomer seal lips is identical. Note the similarities between the clusters in frames 6916 through 8916 in Figure 7-14 and frames 18,032 and 19,778 in Figure 7-15. As with the standard mud mix, the difference is in the break-in period. With the unfilled elastomer seal, aggressive wear occurs immediately after noticeable particle ingestion. With the filled elastomer seal, however, the break-in period extends long past the first visible particle intrusion.

Summary

Separating the standard mud mix revealed two important features of the seal lip wear process. First, wear is caused by clay particles. The majority of sand particles are too large to penetrate the contact band. Furthermore, the clusters in the tests with the clay slurry are identical to the clusters in the tests with the standard mud mix slurry. We therefore conclude that, even in tests with the standard mud mix, clusters are primarily composed of clay particles. Second, there is a synergistic phenomenon at work which causes aggressive wear to occur much more quickly when both sand and clay particles are present than when either are present alone.

7.2.2 Experiments with Arizona Test Dust

Slurries were prepared from three sizes of Arizona test dust in order to determine how small particles have to be to initiate significant wear. The results are presented in order of decreasing particle size.

10-20 μm Arizona Test Dust

Figure 7-16 shows that aggressive wear does not occur in a test with an unfilled elastomer seal and a slurry mixed from 10-20 μm Arizona test dust. After almost 21,500 cycles of operation, no significant cluster formation or penetration had occurred.

Figure 7-17 shows the wear sequence for the test with the 10-20 μm dirt. The slurry is applied after 386 cycles. At 1954 cycles, small faint gray oval clusters form at the outside edge of the contact band. These barely visible clusters increase in size and advance slowly until 4078 cycles. From this point on, long thin clusters form in the direction of seal motion. The dark area on the outside edge of the contact band indicates how far particles have penetrated and what part of the seal lip has been worn. The elongated clusters continually break up and re-form but do not advance inwards significantly during the next 17,000 cycles.

Figure 7-16: Seal Wear Data: Filled Elastomer Seal with 10-20 μm A.T.D

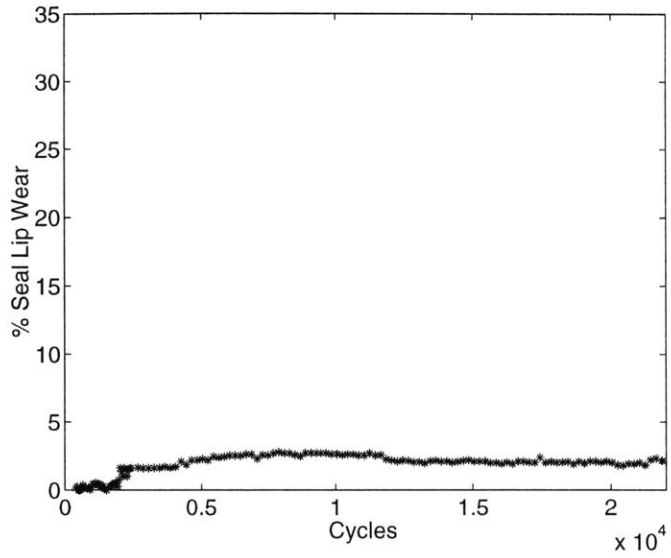

Figure 7-17: Seal Wear Sequence: Unfilled Elastomer Seal with 10-20 μm A.T.D.

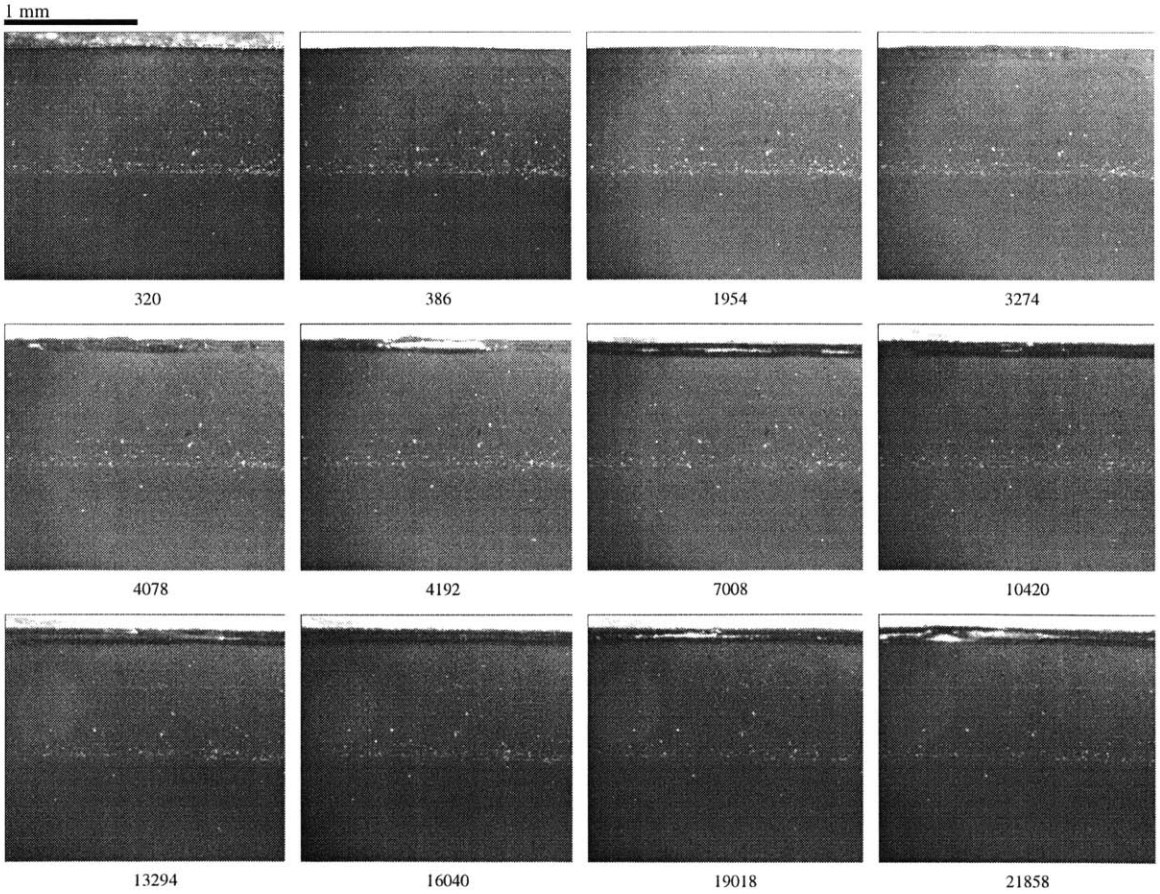

Figure 7-18: Seal Wear Data: Filled Elastomer Seal with 5-10 μm A.T.D.

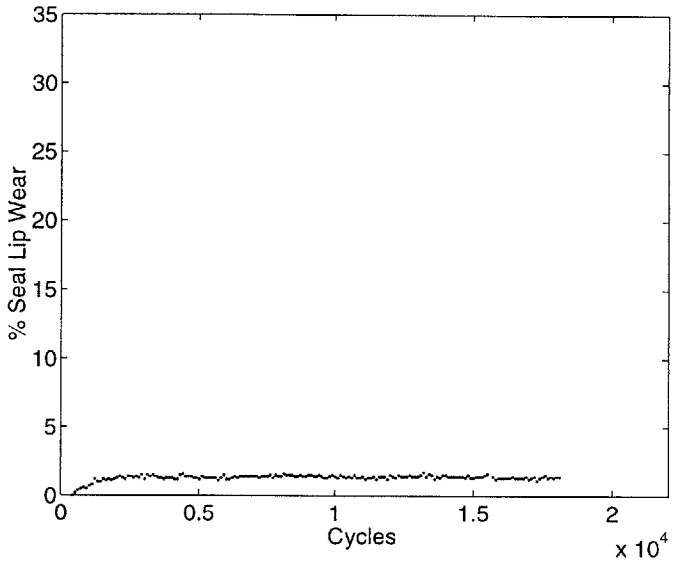

5-10 μm Arizona Test Dust

Figure 7-18 shows the results for the test with an unfilled elastomer seal and a slurry mixed from 5-10 μm Arizona test dust. After a short period of particle ingestion, no wear occurs for roughly 16,000 cycles. Cluster formation and aggressive wear do not occur.

The uneventful wear sequence is displayed in Figure 7-19. The slurry is applied after 382 cycles. Almost immediately, at 576 cycles, small white clusters penetrate the contact band. These clusters and small faint gray clusters exist at the outer edge of the contact band until approximately 1200 cycles. At this point, apparently sufficient seal lip wear has occurred to allow the slurry front to advance and entirely cover the affected region. Nothing happens for the next 17,000 cycles.

0-3 μm Arizona Test Dust

Tests were performed with both unfilled and filled elastomer seals operating in the presence of an abrasive slurry mixed from 0-3 μm Arizona test dust. The results are presented in Figures 7-20 and 7-21. In all three tests, aggressive wear occurs almost immediately. The relevant data is summarized in Table 7.2. Neither the unfilled

Figure 7-19: Seal Wear Sequence: Unfilled Elastomer Seal with 5-10 μm A.T.D.

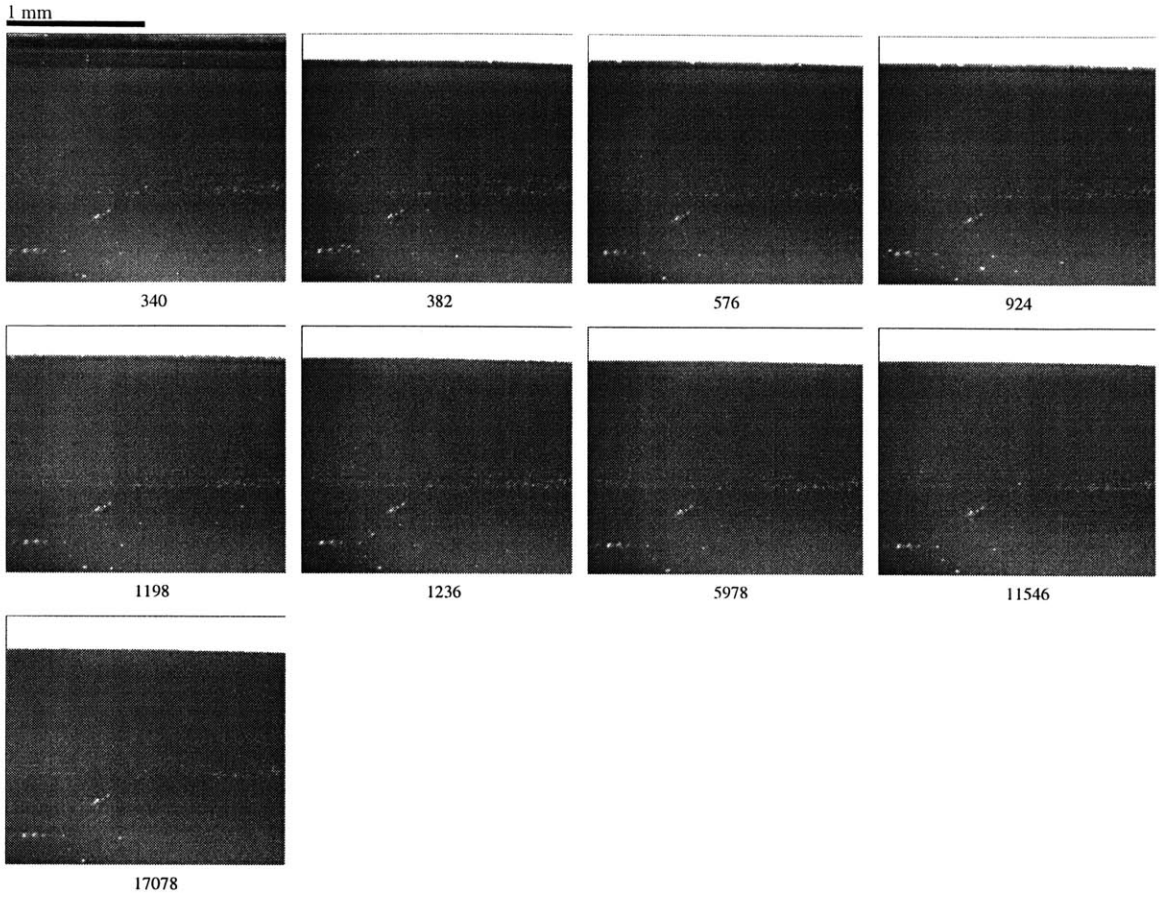

Figure 7-20: Seal Wear Data: Unfilled Elastomer Seal with 0-3 μm A.T.D.

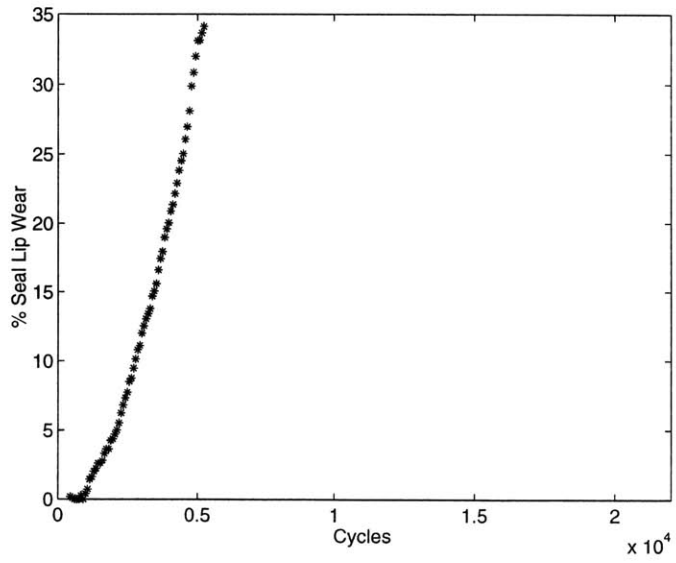

Figure 7-21: Seal Wear Data: Filled Elastomer Seal with 0-3 μm A.T.D.

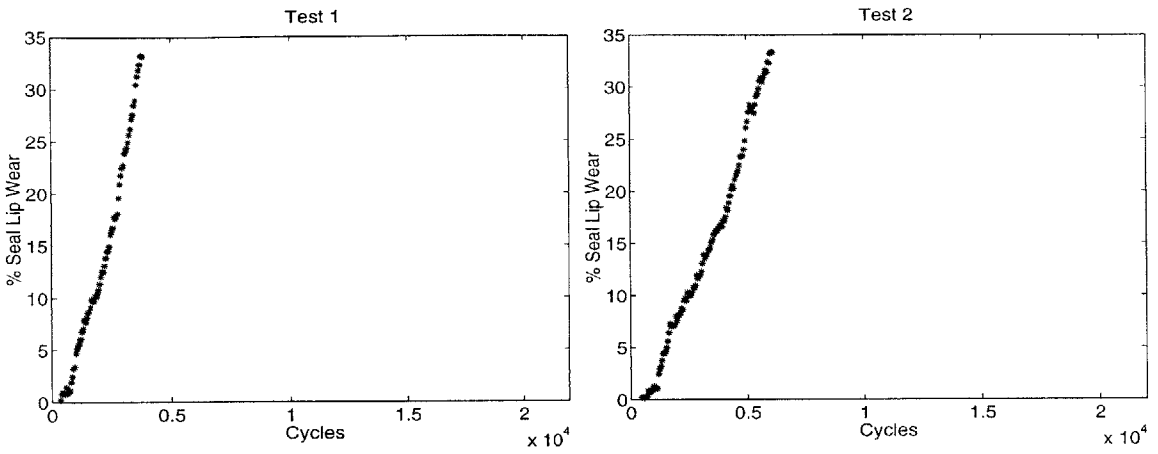

Table 7.2: Summary of Seal Wear Tests with 0-3 μm A.T.D.

	Break-In Period (cycles)	Aggressive Wear Rate (mm/cycle $\times 10^{-4}$)
Unfilled Test	450	3.74
Filled Test 1	672	3.79
Filled Test 2	650	*3.63
Filled average	661	3.71

nor the filled elastomer seals show a significant break-in period. Furthermore, the aggressive wear rates are very similar for all three tests. It should be noted that the aggressive wear rate for the second filled elastomer seal test was calculated excluding cycles 2000 through 4000 when the wear rate slowed noticeably. The slurry was accidentally allowed to dry out during this period causing the wear rate to temporarily decline. Once the slurry was resuscitated by flushing the seal lip with water and applying a fresh layer of slurry, the wear rate increased again.

Figure 7-22 shows the wear sequence for the unfilled elastomer seal. The slurry is added after 436 cycles. Particle ingestion is obvious at 958 cycles. By 1288 cycles, small tear-shaped clusters have formed, and a thick layer of debris has accumulated in the contact band. From this point on, the clusters grown in size and advance at a linear rate until debris begins to fall into the oil.

Figure 7-22: Seal Wear Sequence: Unfilled Elastomer Seal with 0-3 μm A.T.D.

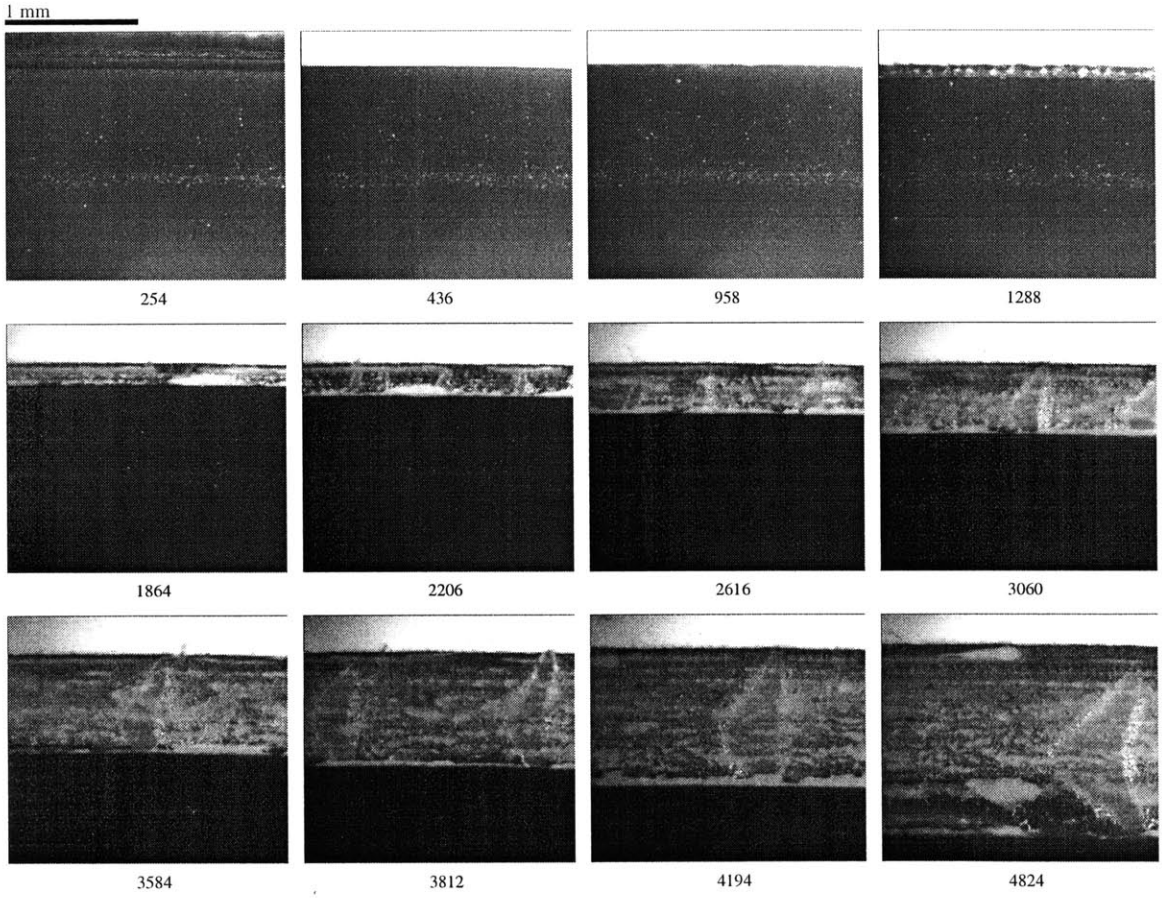

Figure 7-23: Seal Wear Sequence: Filled Elastomer Seal with 0-3 μm A.T.D. (Test 1)

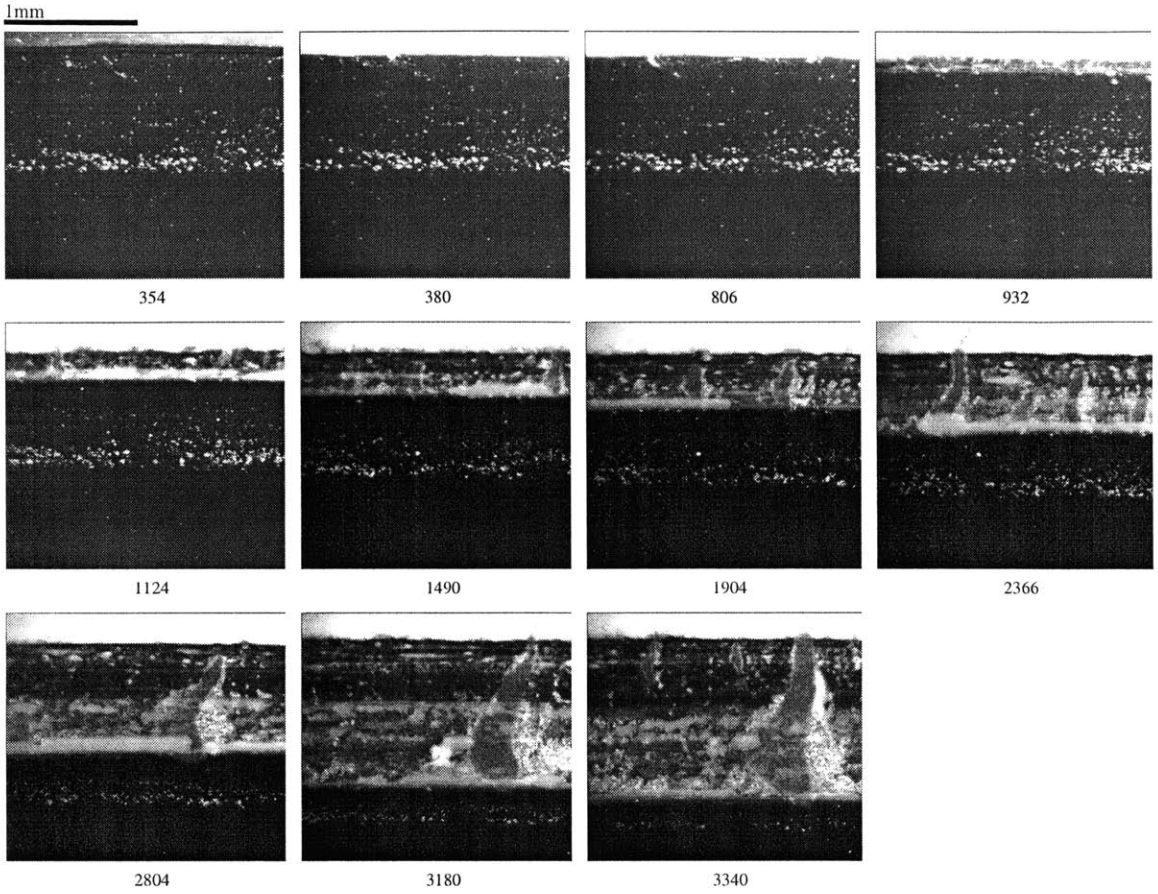

The wear sequence for the filled elastomer seal (test 1), displayed in Figure 7-23, is remarkably similar to the wear sequence for the unfilled elastomer seal. The slurry is applied at 380 cycles. The first significant dirt penetration occurs after 806 cycles. By 932 cycles, small clusters have formed, and a substantial amount of debris has made its way into the contact band. For the next approximately 2500 cycles, the tear-shaped clusters increase in size and advance at a relatively constant rate until they span the entire width of the contact band. The clusters are very similar both in size and shape to the clusters observed in the unfilled elastomer seal test.

Summary

The experiments with the Arizona test dust prove that only particles less than 5 μm in size cause wear. With the 0-3 μm dirt, the presence of fibers affects neither the break-in period nor the aggressive wear rate.

7.3 Conclusions

Several conclusions about the seal lip wear mechanism can be drawn from these experimental results. Table 7.3 summarizes the results of all the seal wear tests. For

Table 7.3: Summary of Seal Wear Tests

Slurry Constituents	Particle Diam. (μm)		Aggressive Wear Rate (mm/cycle $\times 10^{-4}$)		Break-In Period (Cycles)	
	range	median	unfilled	filled	unfilled	filled
0-3 μm A.T.D.	0.2-3	1.1	3.74	3.71	450	661
Mud Mix	0.4-500	29.5	3.90	3.98	550	4900
Clay	0.4-100	12.5	3.60	3.59	5184	16333
Sand	40-500	197.2	–	–	>18,500	>18,500
10-20 μm A.T.D	10-20	14.4	–	–	>21,500	>21,500
5-10 μm A.T.D	5-10	7.2	–	–	>17,500	>17,500

the tests with sand, 10-20 μm dirt, and 5-10 μm dirt, the filled elastomer seals are assumed to have break-in periods at least as long as the unfilled elastomer seals.

First, only particles smaller than 5 μm are able to penetrate the contact far enough and with a high enough frequency to initiate aggressive wear. We have shown that sand, 10-20 μm dirt, and 5-10 μm dirt alone do not cause wear. Therefore, with the standard mud mix slurry, it is only the clay particles that cause the aggressive wear.

Second, for all particle sizes that *do* cause wear, the aggressive wear rates and mechanism of both filled and unfilled elastomer seals are similar. We see in Table 7.3 that the aggressive wear rate is virtually the same in every case. Furthermore, the seal wear sequences in this chapter and chapter 2 show that the the cluster formation and growth processes are all similar. Sometime after particles penetrate the contact

band, they aggregate into clusters. Once clustering begins, the size, shape, and rate of growth of the clusters are remarkably similar for all types of slurries with both filled and unfilled seal lip materials. The well-defined particle size tests are further proof that the fibers in the seal lip do not affect the aggressive wear rate or mechanism.

Third, the break-in period with a slurry of sand and clay is much shorter than the break-in period with a slurry of just clay. Although the sand by itself does not cause aggressive wear, it does play a role in the wear process when paired with the clay. We saw in section 7.2.1 and Figure 7-11 that the sand particles penetrate and roughen the outermost portion of the seal lip. By removing material from and simply lifting up the edge of the seal lip, the sand particles facilitate the ingestion of clay into the contact band. With more clay particles present, clustering and aggressive wear occur much sooner.

Finally, the size of the abrasive particles relative to the size of the fiber fillers determines whether or not the filled elastomer seal outlasts the unfilled elastomer seal. The experiments with the standard mud mix slurry indicate that on average the addition of fibers extends the break-in period from a nearly negligible 550 cycles to 4900 cycles. The experiments with the clay slurry show that on average the fibers extend the break-in period from 5184 cycles to to 16,333 cycles. With the 0-3 μm test dust slurry, however, the break-in periods of the unfilled and filled elastomer seals, 450 and 661 cycles respectively, do not differ significantly.

Adding fibers to the seal lip extends the break-in period of the seal only when the abrasive slurry is composed largely of particles of a size on the same order of magnitude as the size of the fibers. We have shown that it is only the clay particles that cause aggressive wear even when the slurry is composed of a mixture of clay and sand. The median clay particle diameter of 12.5 μm is very close to the fiber diameter of 16 μm. The median particle diameter of the 0-3 μm test dust, however, is a miniscule 1.1 μm – a whole order of magnitude less than the fiber diameter. While both the clay and 0-3 μm test dust particle size distributions show particle sizes in the sub-micron range, the concentration of sub-micron particles is much higher in the test dust. In fact, by volume, 90% of the test dust, but only 10% of the clay,

is less than 2 μm in diameter. The fibers do not extend the break-in period of the seals operating in the presence of the 0-3 μm test dust slurry because most of the test dust is significantly smaller than the fiber diameter. Furthermore, the prolonged break-in period cannot be due to the fibers' effect on the order of magnitude *larger* sand particles since the break-in period is extended whether or not the sand is mixed with the clay.

These results shed some light on the viability of the potential mechanisms proposed at the end of chapters 5 and 6. In chapter 6, it was speculated that the fibers in the seal lip might reduce wear due to micron size particles by either bearing a higher proportion of the load than the elastomer matrix or increasing the lubrication layer thickness. The 0-3 μm test dust experiments, however, show no evidence that the fibers reduce wear due to small particles. The results of the 0-3 μm test dust and standard mud mix experiments with the unfilled elastomer seals indicate that the particle ingestion process is similar for these two types of slurries. The longer break-in period of the filled elastomer seal operating in the presence of the standard mud mix slurry, therefore, must be attributed to the fibers preventing particles from entering the contact band and/or congregating into clusters. While it has a significantly longer break-in period, the filled elastomer seal operating in the presence of the clay slurry in Figure 7-15, however, shows significant particle ingestion and small cluster formation much sooner than the unfilled elastomer seal in Figure 7-14. The rougher surface and uneven contact stress distribution of the filled elastomer seal lip actually appear to make it easier for particles to enter the contact band.

Thus, it seems likely that the fibers' physical presence and effect on the contact stress distribution inhibit the clustering process. The fibers, themselves, or the spikes in the contact pressure that they produce, deter particle migration and coalescence into clusters. In addition, when smaller than critical size clusters form, the fibers may break them apart or at least inhibit them from growing larger and pushing further into the contact band. As Yang observed, once the clusters reach a size similar to that of the fibers, they produce deformations large enough to pull some of the fibers out of the matrix [4] and effectively increase the fiber spacing. We recall that fiber pull-out

was in fact apparent in Figures 2-8 (b) and 2-9 (b). The critical size clusters likely form in the spaces between fibers and may initially be composed primarily of the very small particles that are able to move freely within the contact band as discussed below. Areas of high contact pressure similar in size to the fibers will not slow the growth and advance of much larger clusters. Furthermore, as discussed in section 5.3, large clusters will lift up and pass underneath fibers near or at the surface quite easily. Powerless to act against significantly larger clusters, the fibers that remain do not alter the aggressive wear of the seal lip.

This mechanism does not work with the 0-3 μm test dust slurry because the majority of the particles are much smaller than the fibers. By volume, 54% of the particles are less than 1 μm in diameter. These sub-micron size particles are able to move freely within the contact band and quickly form clusters. The fibers are typically at least a few microns from and skew to the seal surface. The micron size and smaller particles are able to move underneath the seal lip without ever making contact with the fibers. In section 6.1, we observed gaps between the elastomer and the rigid surface adjacent to fibers at the surface of the elastomer. In sections 6.2 and 6.3, we saw regions of low pressure around fibers just below the surface. Furthermore, the surface irregularities of the seal lip in combination with the surface roughness of the bushing surface produce additional regions of low pressure and perhaps even micron size gaps between the seal and its running surface. When a sub-micron size particle encounters a fiber or region of high contact pressure beneath a fiber, it is easily able to find a path of lower resistance. With essentially unrestricted particle mobility, the only limiting factor is the ingestion of a large enough volume of particles to form the critical size clusters.

Chapter 8

Seal Microtexturing

We have definitively established that adding fibers to the elastomer seal lip extends the break-in period of the seal when the majority of the abrasive particles are similar in size to the fibers. Finite element modeling and well-characterized dirt experiments indicate that this phenomenon is largely due to the fibers' effect on cluster formation. The fibers alter the contact stress distribution between the seal and its running surface and provide physical barriers to particle movement. In this chapter, we propose a change in seal lip surface geometry that would imitate the effect of the fibers. We suggest adding a "microtexture" to the currently smooth seal lip surface.

Accomplishing an improvement in seal life similar to that observed with the fiber-filled elastomer seal lip with a change in seal lip surface geometry is highly desirable. The glass fibers not only are expensive but also complicate the processing of the polyurethane. Furthermore, a similar geometry could be designed for many different sealing applications – including those where fibers are not an attractive option. In applications other than the track seal, adding a filler may change the mechanical properties of the seal material enough to affect the function of the seal. Furthermore, the fibers are much harder than the elastomer and, in some applications, may cause abrasive wear of the seal's running surface. Finally, as we have shown in chapter 7, the effectiveness of a particular size fiber is strongly related to the size of the offending abrasive particles. The size of the abrasive particles varies depending on the operating conditions of the seal. Scaling the geometry of the seal surface for differ-

ent applications would be simpler and cheaper than using different sized fibers. In addition, some fibers smaller than those currently used in the track seals are considered carcinogenic and are not manufactured. Perhaps several different microtextures could be used on the track seals alone depending on where the tractors are operated. A simple swap of a mold insert is all that would be required to change the seal lip surface geometry.

8.1 Microtexture Feature Geometry Design Process

The approach to designing the prototype microtexture was to duplicate the effect of the fibers on the contact stress distribution between the seal lip and the bearing surface. While it may prove possible to improve the design, the success of the initial design would validate the mechanisms proposed in chapter 7.

The fibers delay the formation of the critical size clusters but do not affect the aggressive wear of the seal. The initial cluster formation process occurs only at the very outside of the seal lip. It is therefore necessary to determine the effect on the contact stress distribution of a fiber at the outer portion of the seal lip contact band. A three-dimensional finite element model [8] of a slice of an unfilled elastomer seal lip was compressed by 0.7 mm, a displacement equivalent to that in the actual application. Figure 8-1 shows the undeformed mesh and a contour plot of the stress in the 2-direction. The contact stress profile is plotted along a line in the 1-direction (the radial direction) in Figure 8-2. Moving in the positive 1-direction, we see that the contact stress steadily increases from where the seal lip first contacts the bushing surface until less than 0.2 mm from the lip's outside edge where it reaches a maximum of -10.1 MPa before decreasing slightly. The contact stress at the very outside edge of the seal lip is -8.3 MPa. A value of -9.0 MPa was chosen as representative of the contact stress in the vicinity of the seal lip outside edge.

The three-dimensional finite element simulation, described previously in section

Figure 8-1: 3D Finite Element Model of Smooth Seal Lip [8]

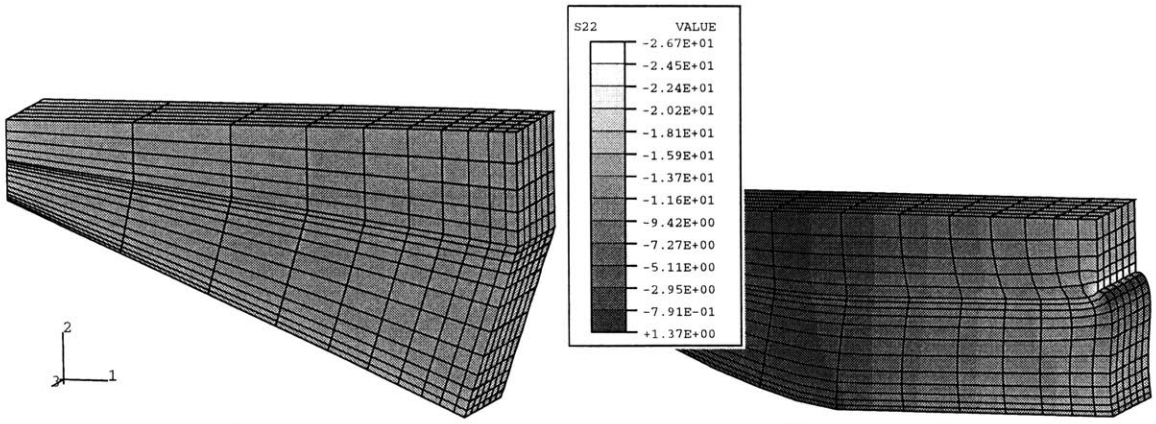

Figure 8-2: Smooth Seal Lip Contact Stress Profile

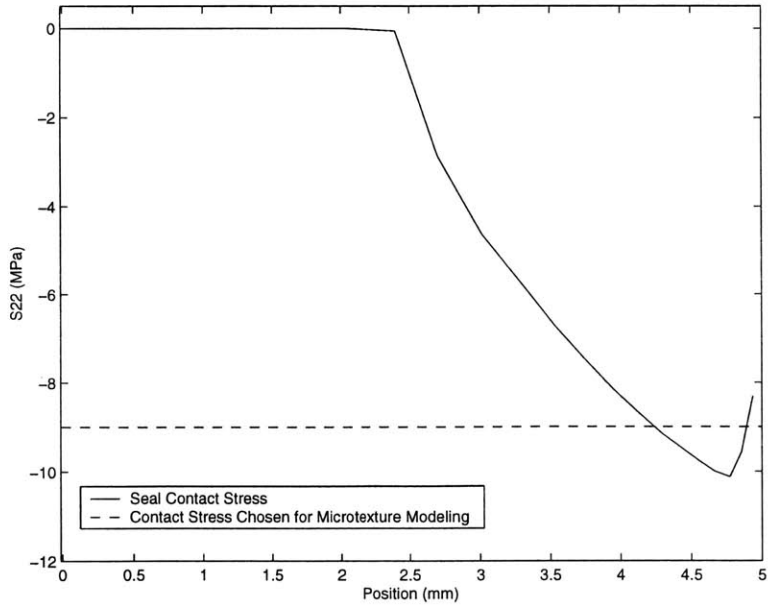

Figure 8-3: 3D Fiber One Half Diameter Below Surface

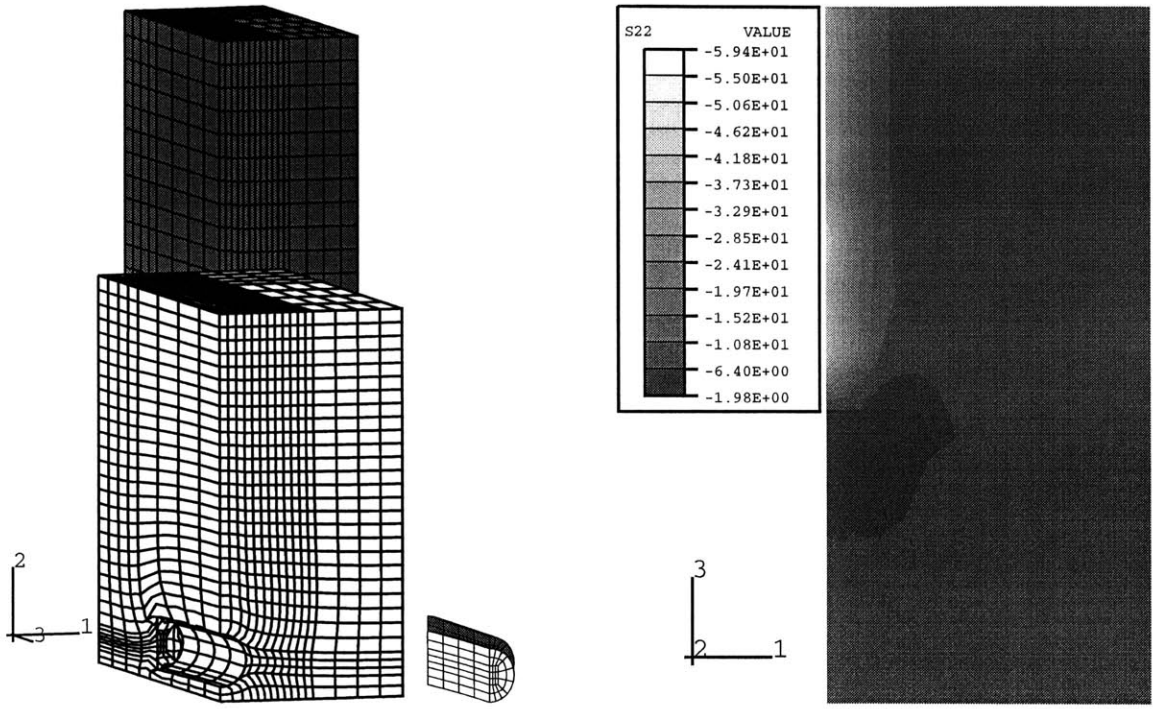

Mesh Contact Stress Contour Plot

6.3, of one quarter of a fiber one half fiber diameter from the surface of a polyurethane block was used to model the effect of the fibers near the outside edge of the seal lip. With the Arruda-Boyce Eight Chain model representing the material behavior, uniaxially compressing a block of unfilled polyurethane to a true strain of -.532 produces a contact stress of -9.0 MPa. The mesh shown in Figure 8-3 was therefore compressed by the same amount in order to simulate the state of stress at the outer portion of the seal lip. Figure 8-4 shows the contact stress profile underneath the center of the fiber along a line perpendicular to the fiber's axis. The contact stress reaches a maximum of -31.6 MPa directly underneath the center of the fiber. Adjacent to the fiber, the contact stress decreases to as little as -8.1 MPa

The goal was to design a microtexture geometry which yields a contact stress profile similar to that in Figure 8-4. The contact stress contour plot in Figure 8-3 indicates that the contact stress profile is approximately constant along most of the length of the fiber. There is also, in Figure 8-3, a region at the end of the fiber where

Figure 8-4: Contact Stress Profile Normal to Fiber Axis

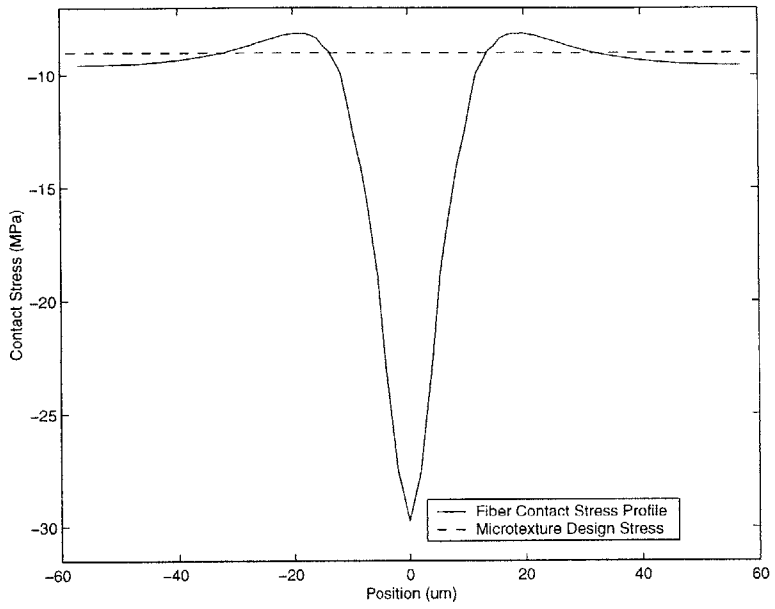

the contact stress decreases to as little as -1.98 MPa. Since it is the peaks in the contact stress at the fibers that are thought to prevent cluster formation and extend the break-in period of the seal, only this facet of the contact stress distribution will be replicated by the microtexture. If a microtexture feature shape with a length to width ratio similar to that of a fiber is assumed, then the end effects may be neglected and two-dimensional plane strain models may be used to investigate potential designs.

8.2 Finite Element Modeling of Potential Microtexture Feature Geometries

Several different feature geometries were modeled using two-dimensional plane strain elements. The Arruda-Boyce Eight Chain model was once again used to represent the material behavior. The features were added to a mesh 200 μm tall by 50 μm wide. Compressing the smooth mesh against a rigid surface by 56.1 μm, equivalent to a true strain of 0.247, produces the required contact stress of -9.0 MPa. All meshes were therefore compressed by 56.1 μm plus the height of the feature.

Figure 8-5: Microtexture Design 1 Mesh

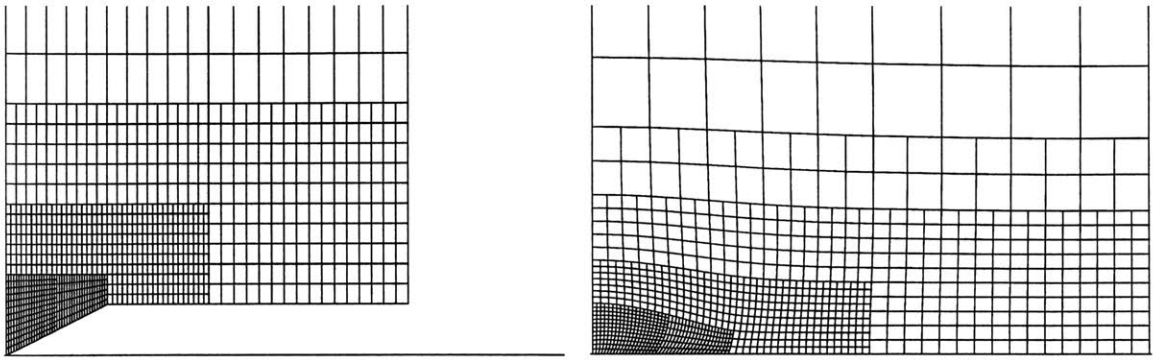

Design 1 is shown in Figure 8-5. The symmetry of the geometry requires just one half of the feature to be modeled. The feature is a sharp bump measuring (including the half not modeled) 20 μm wide by 5 μm tall. The sides of the bump meet at a point. Figure 8-6 shows the contact stress profile for the pointed bump geometry.

Figure 8-6: Microtexture Design 1 Contact Stress Profile

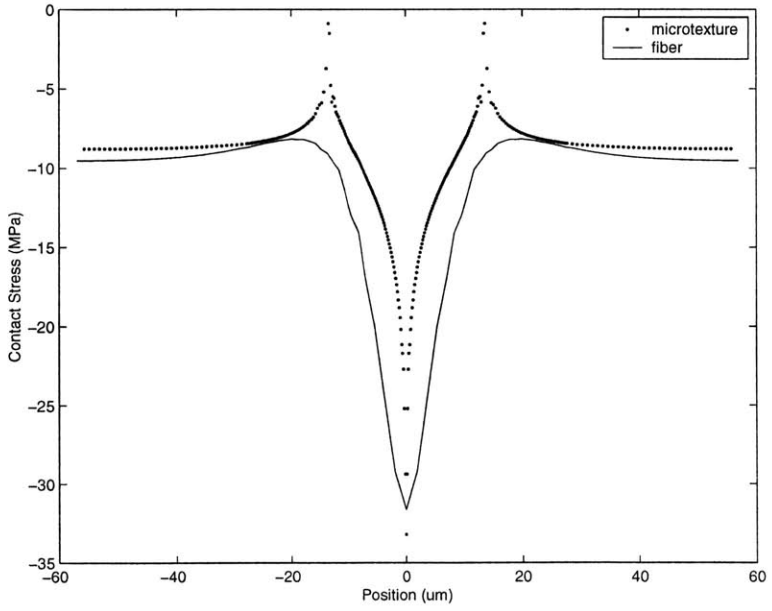

With a maximum of -39.2 MPa, the profile matches the fiber's contact stress profile relatively well but needs to have a somewhat wider peak. Furthermore, a feature

Figure 8-7: Microtexture Design 2 Mesh

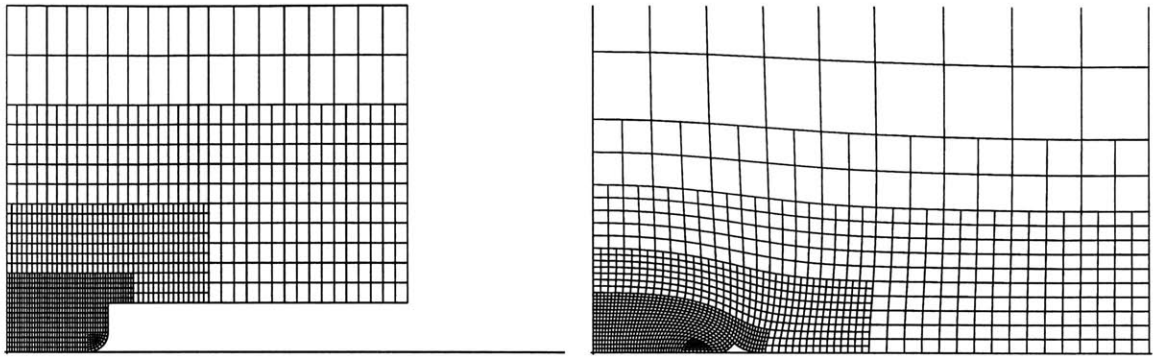

with such as sharp edge would be impossible to manufacture. It is valuable to model, however, as a limiting case.

At the other extreme is the 20 μm wide by 5 μm tall flat bump of Design 2 shown in 8-7. A 2 μm radius chamfer is put on the corner of the bump. As shown in Figure 8-8, the larger surface area immediately in contact with the rigid surface produces a

Figure 8-8: Microtexture Design 2 Contact Stress Profile

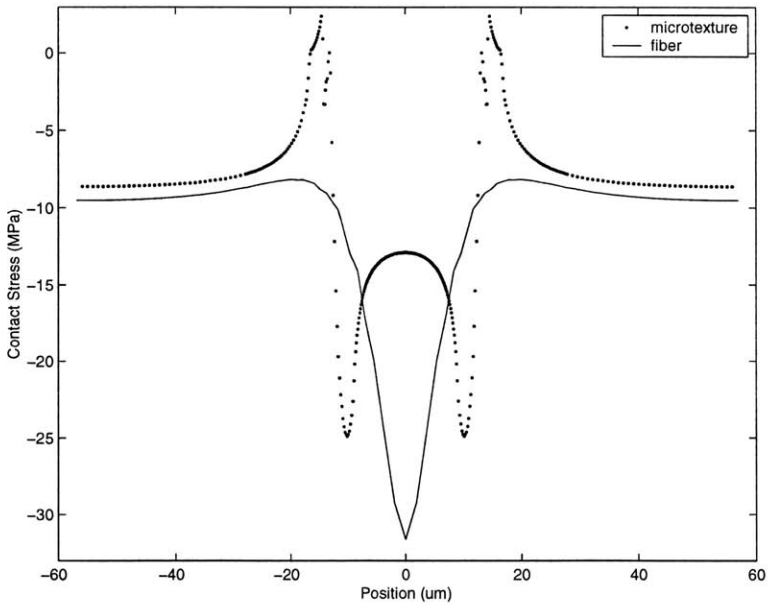

much wider but shallower contact profile. The maximum contact stress is only -24.9

Figure 8-9: Microtexture Design 3 Mesh

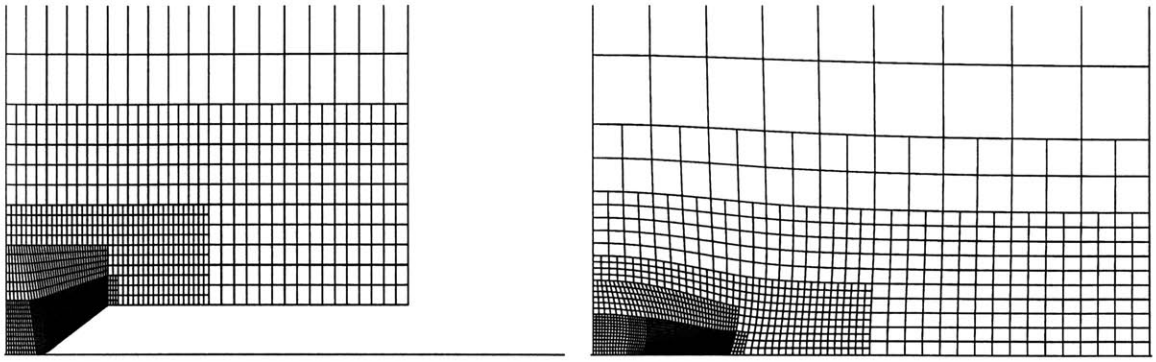

MPa.

Design 3, displayed in Figure 8-9, is similar to the sharp bump of Design 1 but adds a 6 μm wide flat to the top of the bump. The overall bump dimensions remain 20 μm wide by 5 μm tall. A chamfer with a 2 μm radius is put on the end of the flat. Figure 8-10 shows the contact stress profile for this geometry. Having a substantial

Figure 8-10: Microtexture Design 3 Contact Stress Profile

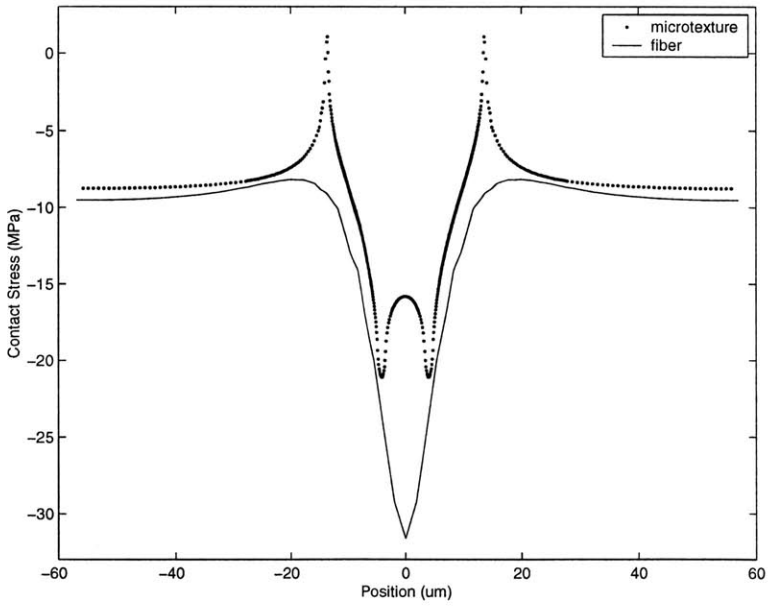

surface area immediately in contact with the rigid surface, similar to Design 2, the

Figure 8-11: Microtexture Design 4 Mesh

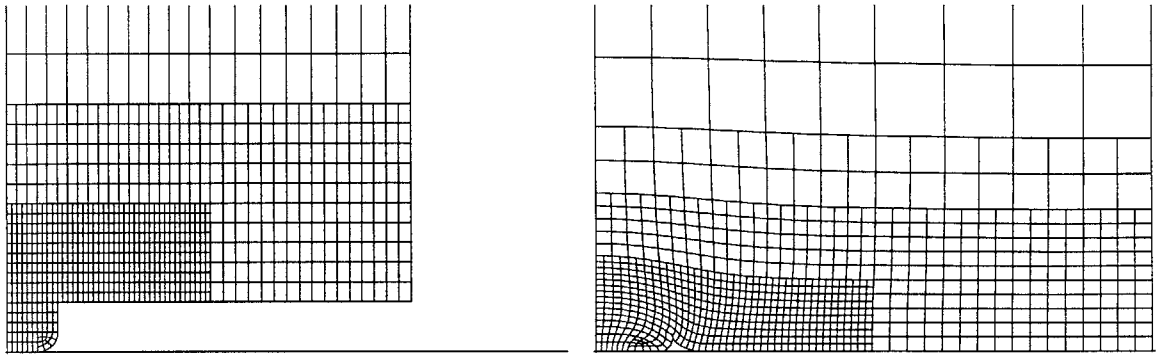

flat-topped bump exhibits a contact stress peak which matches the width of the fiber's peak fairly closely. As a result, however, the peak contact stress is still only -21.1 MPa.

Figure 8-11 shows the next design iteration. In Design 4, the height of the bump is kept at 5 μm but the width is reduced to 10 μm. A 2 μm radius chamfer is put on the corner of the bump. The corresponding contact stress profile in Figure 8-12 shows a narrower yet larger amplitude contact stress peak. The maximum contact stress of Design 4 is -28.8 MPa.

In order to attain a slightly wider and larger amplitude contact stress peak, in the final iteration, Design 5, the width of the bump is increased by 20% to 12 μm and the height is increased by 60% to 8 μm. A 2 μm radius chamfer is again put on the corner of the bump. An effectively infinite corner radius is also added at the base of the bump in order to avoid severe element distortions at the sharp corner. Figure 8-13 shows the resulting deformed and undeformed meshes. Figure 8-14 indicates that this design produces a wider contact stress peak which also has a maximum value, -31.4 MPa, very close to that below the fiber.

The bump design in Figure 8-13 was chosen for prototype production. The geometry produces a contact stress profile very similar in width and amplitude to that of the simulation with a fiber one half diameter below the surface of the elastomer. Furthermore, it is a simple shape that should be feasible to actually manufacture.

Figure 8-12: Microtexture Design 4 Contact Stress Profile

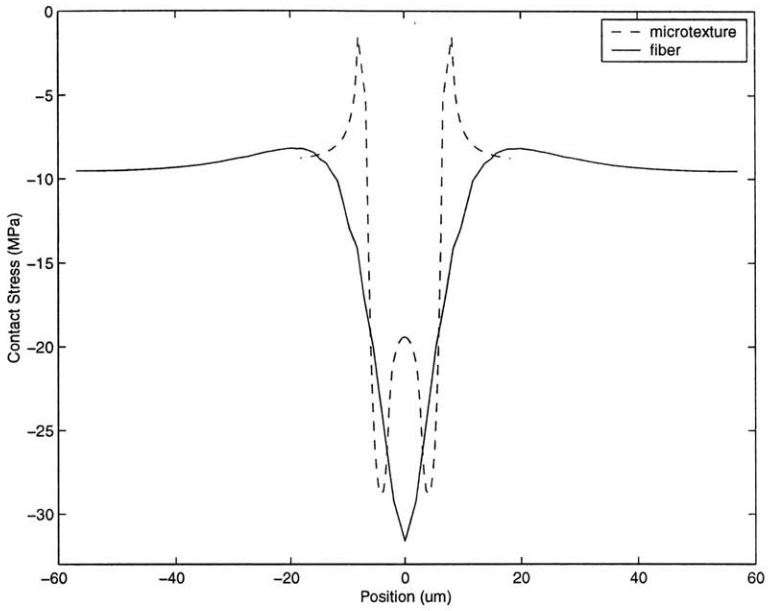

Figure 8-13: Microtexture Final Design Mesh

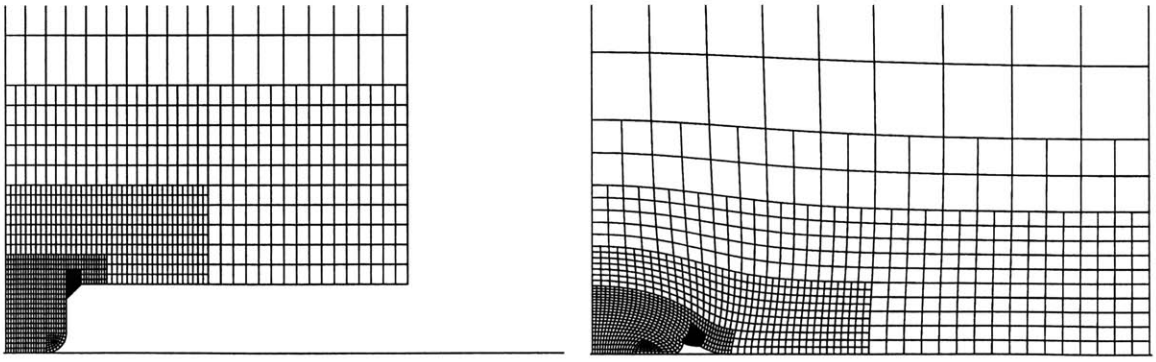

Figure 8-14: Microtexture Final Design Contact Stress Profile

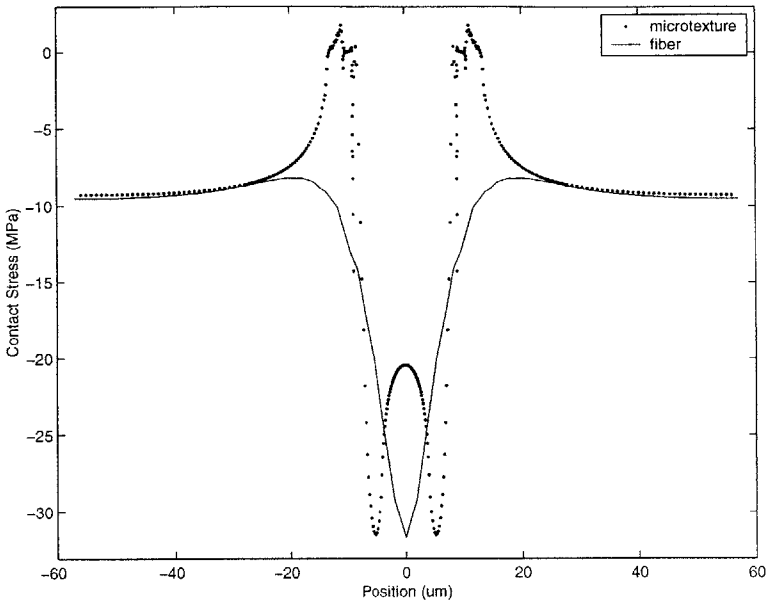

Based on the fibers' typical length to diameter ratio of 8, the length in the third dimension was chosen to be 96 μm.

8.3 Spacing and Orientation of Microtexture Features

The next step was to determine how the features should be mapped out on the seal lip. The feature orientation pattern and a characteristic spacing distance between features were defined. These parameters were chosen based on the orientation and spacing of the fibers in the filled elastomer seal lips.

The characteristic spacing length was calculated largely from experimental observations. As indicated in chapter 2, in the seal wear experiments, the fibers near the surface of the seal show up as dark spots in the CCD camera images. The average distance between the centers of adjacent fibers was therefore calculated in pictures of four different seals. The images used for the calculation are shown in Figure 8-15. The average value of the four pictures is approximately 200 μm.

Figure 8-15: CCD Images Used to Calculate Feature Spacing

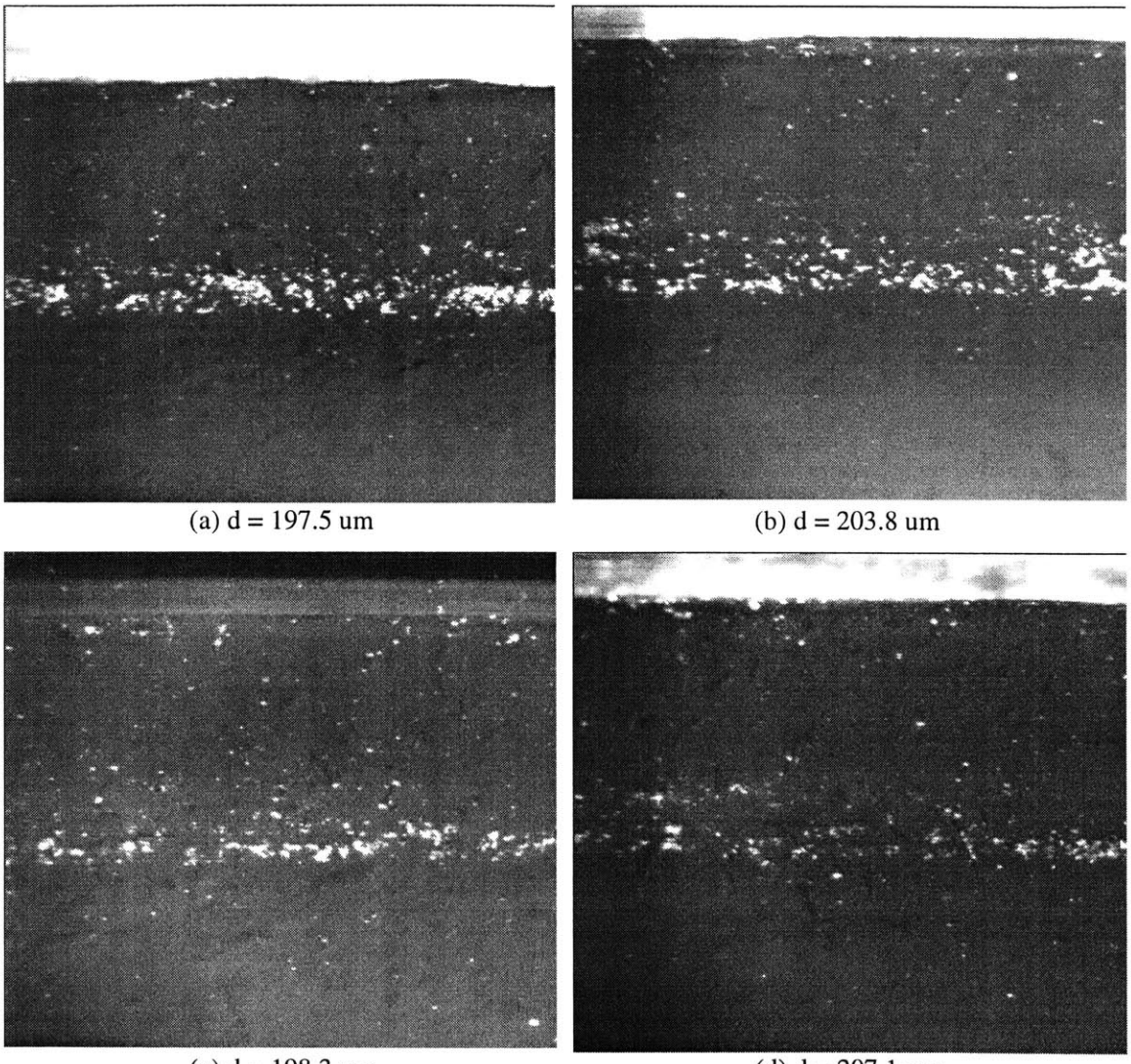

(a) d = 197.5 um

(b) d = 203.8 um

(c) d = 198.3 um

(d) d = 207.1 um

Figure 8-16: SEM Observations of Fiber Spacing and Orientation

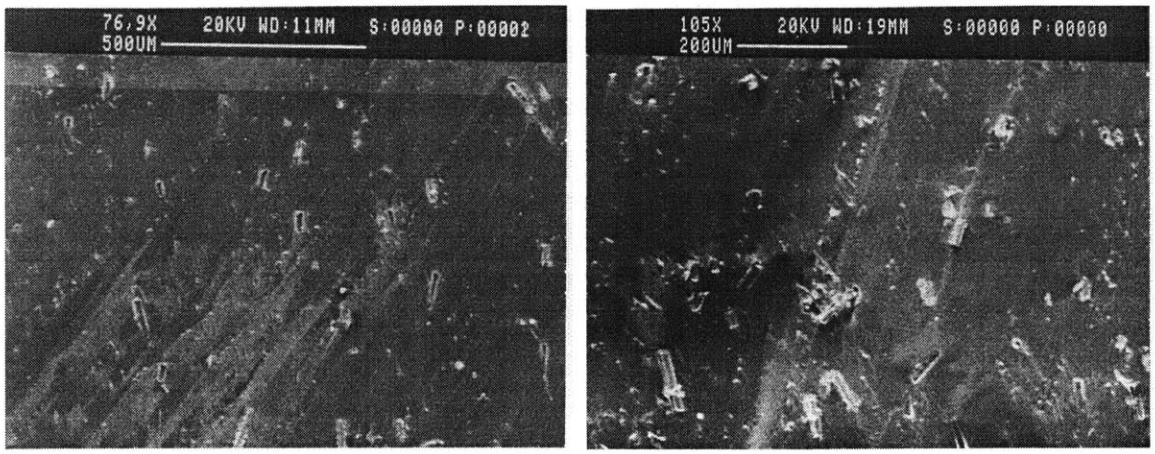

SEM observations of a filled elastomer seal lip were used to verify the calculated spacing value. Since fibers are rarely seen right at the surface of the seal lip, a thin layer of polyurethane was sliced off the seal surface to uncover the fibers immediately below the surface. Once the "skin" of the seal had been removed, actual fibers or cavities where the fibers had been pulled out were readily apparent. Two such observations are shown in Figure 8-16. While statistical analysis was not performed on these images, they indicate that a spacing of 200 μm seems reasonable. Furthermore, a rough theoretical calculation, based on the filler fraction and the densities of the glass fibers and polyurethane, also resulted in a similar spacing value. 200 μm was therefore chosen as the characteristic spacing length.

The CCD camera images in Figure 8-15 and the SEM observations in Figure 8-16 also show the randomness of the fibers' orientations. The placement of the microtexture features reflects this randomness. Figure 8-17 shows a plan view of how the features are arranged in unit cells of four features in an "X" pattern. The center-to-center distance between fibers within the unit cell is 200 μm. Figure 8-18 shows how the unit cells, aligned always with the radial direction, are placed over the entire surface of the seal lip. The center-to-center horizontal distance between fibers in adjacent unit cells is also approximately 200 μm. This dimension is held at the outside of the seal lip but becomes slightly smaller as the radial distance from the

Figure 8-17: Microtexture Unit Cell Dimensions (Plan View)

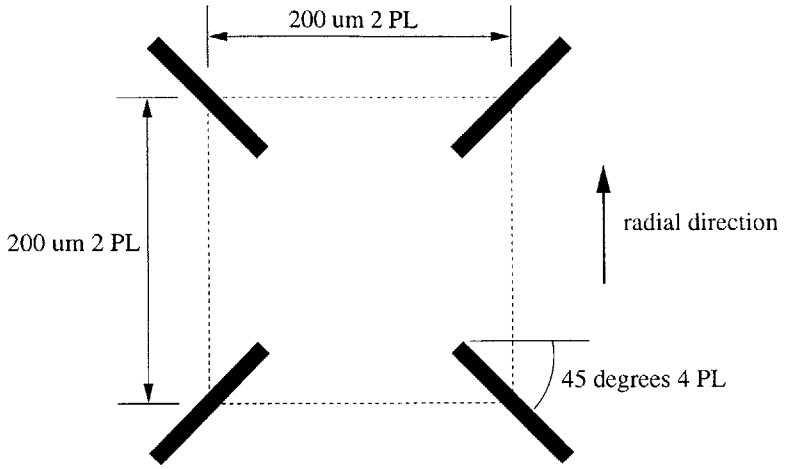

Figure 8-18: Microtexture Unit Cell Placement (Plan View)

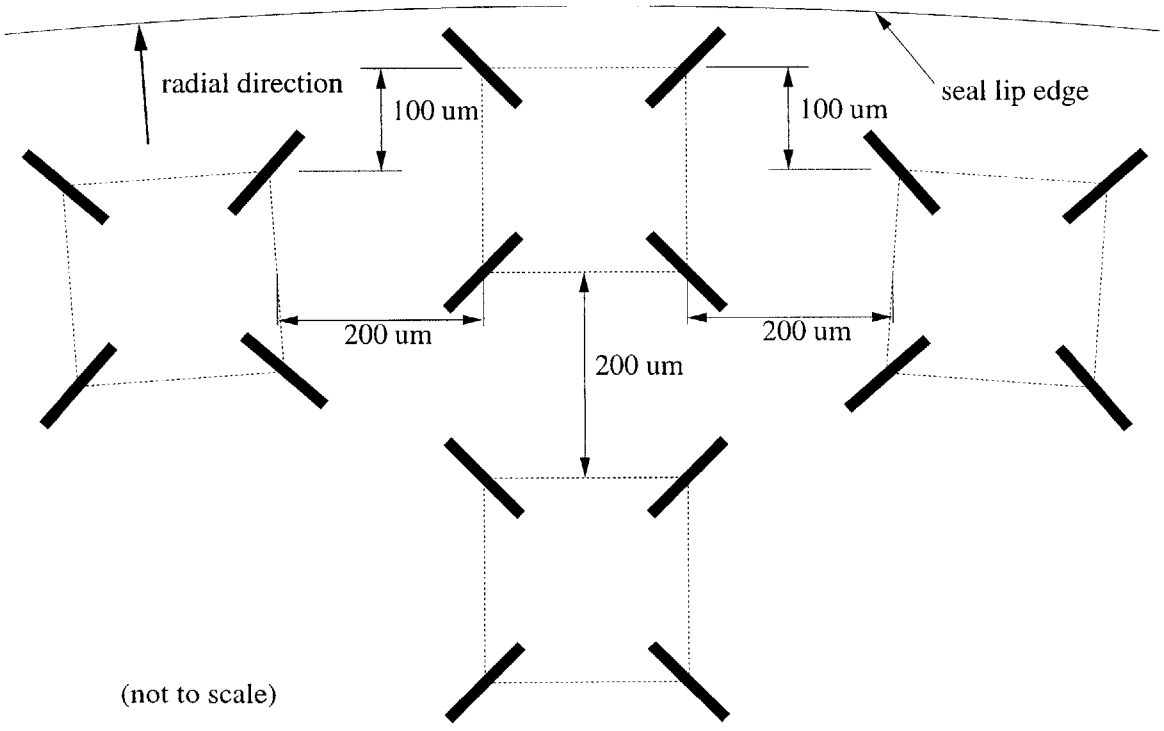

seal's center decreases. The curvature of the seal is so large compared to the width of the unit cell, however, that the variation is negligible. In the vertical direction, the unit cells are offset by 100 μm.

Two additional designs will also be manufactured. One will be a scaled up version of the original design with all dimensions doubled. The other will be identical to the original design but with the fiber orientations determined randomly.

8.4 Microtexture Manufacturing

The seals lips are injection molded. Creating protrusions on the seal lip necessitates putting depressions or "slots" in the steel mold insert used to manufacture the seal lip. Excimer laser microprocessing will be used to machine the the required features into the mold insert. During the laser processing, the mold insert will be clamped to a sine plate mounted on a rotary stage such that the insert surface will always be normal to the laser.

A feasibility study was performed on a test piece made from the same tool steel as the mold insert. Figure 8-19 shows a three by three array of slots and a close-up

Figure 8-19: SEM of Slot Laser Machining

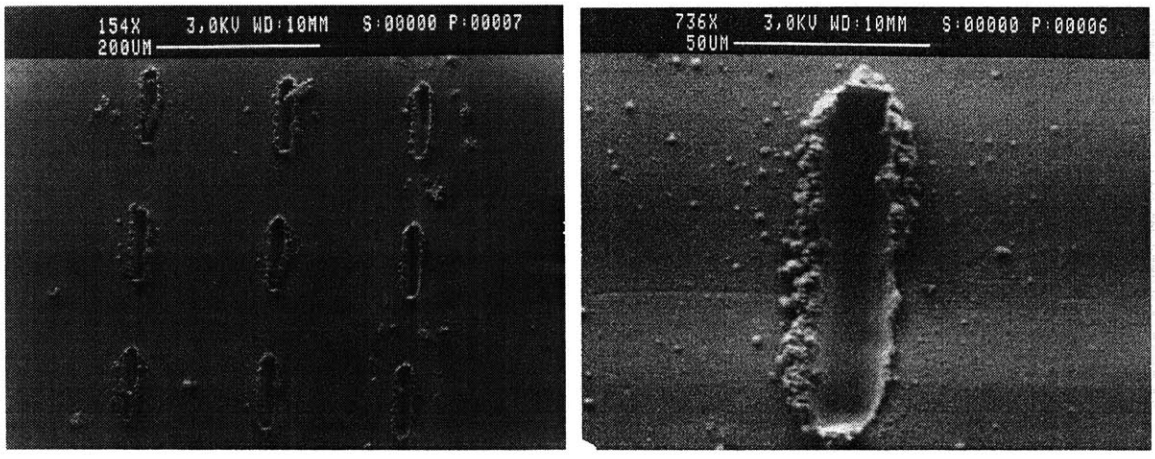

array of slots one slot

of one slot. The slot length and width appear within acceptable tolerances of the

specified dimensions. Around each slot entrance is a "volcano" of ejected material. Similar to a burr in conventional machining, this result is typical of laser processing. Post-processing will be required to remove this unwanted material. Several techniques are available including electro-polishing and chemical polishing.

Caterpillar will provide actual seal inserts for seal prototype production. Once manufactured, the microtextured unfilled elastomer seals will be tested to see how their wear characteristics compare with those of the smooth filled elastomer seals. Similar wear characteristics would be concrete proof that the fibers' effect on the contact stress distribution between the seal lip and the bushing surface extends the break-in period of the seal.

Chapter 9

Conclusions and Future Work

The goal of this project was to understand how fibers affect the abrasive wear of fiber-filled elastomers. The approach was to use a combination of experiments and finite element analysis. The track seal application was used as motivation and a source of experimental data. With a better understanding of the role of the fibers, one would have the ability to choose the optimum filler package for a particular abrasive wear application. While much was discovered about the track seal application and the abrasive wear of fiber-filled elastomers in general, there is still room for future work.

9.1 Summary of Conclusions

A series of experiments with filled and unfilled elastomer track seals operating in the presence of a mixed particle size abrasive slurry were performed. The filled elastomer seals exhibited a break-in period almost 10 times longer than that of the unfilled elastomer seals. The aggressive wear rate of the two materials, however, was nearly identical. It was observed with both seal types that the aggressive wear period began once critical size clusters, approximately 100 μm in size, of abrasive particles had formed. The clusters that formed during the aggressive wear period of both seal materials were similar in size and shape. Furthermore, SEM observations of worn seal lips revealed that both the filled and unfilled materials showed similar abrasion patterns. The abraded surfaces exhibited the classic ridge pattern observed by many

investigators for the abrasive wear of elastomers. The fact that the ridge spacing was much smaller than the fiber spacing was further evidence that the fibers did not influence the aggressive wear process. There were some indications in the size and spacing of the abrasion patterns on the worn seal lips that, once the clusters had penetrated a portion of the seal lip, more material may actually have been removed from the unfilled elastomer seal lips than from the filled elastomer seal lips by the abrasive action of the large clusters. Any decrease in material removal behind the advancing cluster fronts did not, however, affect the aggressive wear rate as it was defined. These experiments provided irrefutable proof that the addition of fibers increases the life of the seal lip elastomer solely by extending the break-in period.

Micromechanical modeling of the abrasive wear of unfilled elastomers revealed much about the nature of the abrasive wear process. Compression of an elastomer block over a rigid particle produced a concentration of stress and strain in the elastomer around the particle. Depending on the friction coefficient, the level of compression, and the material model used, the maximum tensile stress in the elastomer occurred at distance never greater than 1/4 particle diameter from the elastomer surface either directly over the particle or where the elastomer lifted off of the particle. Shearing the elastomer over the particle with a non-zero coefficient of friction produced deformation patterns consistent with the observations of Schallamach, Barquins, Fukahori, and others for the abrasive wear of elastomers.

Surface analyses of filled and unfilled elastomer seals lips indicated that fibers are present at or near the surface of the filled elastomer seals. Micromechanical modeling was therefore performed with fibers at and near the surface of the elastomer.

The abrasive wear of elastomers can be considered a fatigue fracture process caused by the high tensile stresses created in the elastomer by the abrasive particles. Microcracks form and then propagate until sizeable chunks of material are removed producing the ridge pattern. Compression simulations were therefore performed in order to investigate the fibers' effect on the maximum tensile stress in the elastomer due to the presence of the particles. It was shown, for three different particle sizes, fiber orientations, and fiber spacings, that, in all but one rather unlikely case, the

fibers actually increased the maximum tensile stress in the elastomer. This result verified the experimental observations that the fibers did not significantly affect the aggressive wear rate or abraded surface characteristics of the seal lip.

Shearing simulations with several particle sizes and fiber orientations showed the large force required to move a particle past a fiber at the surface of the elastomer. It was concluded that a likely mechanism by which the fibers extend the break-in period of the seal is by preventing particles in a certain size range from entering the contact band and, once they *are* in the contact band, preventing the particles from aggregating into critical size clusters. Although not explicitly shown, it was inferred from the simulation results that the fibers are less effective at impeding the motion of particles much smaller ($\sim$1 μm or less) and much larger ($\sim$100 μm or greater) than their own size. This supported the experimental observation that the fibers did not affect the cluster formation and aggressive wear rate once clusters larger than the approximate critical size of 100 μm had formed.

Additional finite element simulations examined the effect of fibers near or at the surface of the elastomer on the contact stress profile between the elastomer and the rigid surface. Sharp peaks in the contact stress were seen underneath the fibers while areas of significantly reduced contact stress were observed adjacent to the fibers. Several mechanisms were proposed based on this result. While later disproven, it was postulated that, by promoting lubrication and shielding the matrix material from a portion of the applied load, the altered contact stress profile might reduce wear due to small particles and, hence, prevent larger particles and more small particles from entering the contact band. It was also proposed that the contact stress peaks could function similarly to the fibers in the shearing simulations. In other words, the regions of high contact stress might prevent particles from advancing past the outermost portion of the contact band, interfere with their coalescence into clusters, and break up clusters still in the formative stages.

Experiments with slurries composed of specific particle sizes provided valuable insight into the seal lip wear mechanism. Slurries of sand, clay, and Arizona test dust in 0-3 μm, 5-10 μm, and 10-20 μm size ranges were used. Particle size analyses were

performed on all dirt samples. The clay particles were determined to be in the 0.4-100 μm range with a median particle size of 12.5 μm. The sand particles fell in the 40-500 μm range with a median of close to 200 μm. It was discovered that only particles smaller than 5 μm were able to penetrate the contact band in quantities sufficient to cause wear. It was therefore concluded that, with the standard mud mix of sand and clay, only the clay particles cause wear. It was also observed, however, that aggressive wear occurred much sooner with the standard slurry mix than with a slurry of clay by itself. Large particles evidently roughen the outside edge of the seal lip allowing small particles to enter the contact band more easily and in larger quantities. Furthermore, with both the filled and the unfilled elastomer seals operating in both the clay and the 0-3 μm A.T.D. slurries, the aggressive wear rate and particle clustering behavior were similar. This was simply further evidence in support of what had already been taken for granted – that the fibers do not alter the aggressive wear mechanism.

The well-defined slurry experiments clearly showed that the fibers only extend the break-in period of the seal when the slurry constituents are predominantly similar in size to the fibers. The 0-3 μm A.T.D slurry, with a median particle size of 1.1 μm, caused aggressive wear almost immediately with both filled and unfilled elastomer seals. The clay slurry, with a median particle size of 12.5 μm and 90% of its particles larger than 2 μm, however, initiated aggressive wear much sooner with the unfilled elastomer seal than with the filled elastomer seal. This, in itself, was strong proof that the mechanism by which fibers extend the break-in period of the seal is by, either physically or via their effect on the contact stress distribution, deterring particle ingestion and cluster formation. While the fibers interfered with the particles, mostly several microns in size or larger, found in the clay slurry, they were ineffective against the large quantities of micron size and smaller particles found in the 0-3 μm A.T.D slurry. The micron size and smaller particles are able to move easily under and/or around these obstacles and form clusters. Furthermore, the 0-3 μm A.T.D experiments also refuted the competing theory that the fibers extend the break-in period by reducing wear due to small particles.

Having concluded that it is the fibers' physical presence and effect on the contact

stress distribution that extends the break-in period of the seal, we suggested an alternative, more desirable method to accomplish an equivalent improvement in seal life. A microtexture feature was designed to reproduce the contact stress profile of a fiber near the surface of the seal lip. Feature spacing and orientation was based on simple calculations and direct observations of fibers near or at the surface of the seal lip. A method of manufacturing the design was identified and prototype work has begun.

The abrasive wear mechanisms identified in this work are by no means exclusive to the track seal or to even oscillating face seals in general. The track seal application is representative of many three body abrasion situations where loose abrasive particles tend to cluster. Furthermore, the finite element modeling performed was fundamental in nature and is pertinent to the abrasive wear of *any* elastomer. The mechanisms by which the fibers increase the wear resistance of the seal lip elastomer should therefore be operative in many other applications. Applying the knowledge gained from the track seal experiments and fundamental modeling presented here to new areas is an opportunity with tremendous potential.

9.2 Future Work

An obvious area to continue the work presented in this thesis is microtexturing. Several microtexture designs are currently in production. When complete, the microtextured seals will be tested with at least the standard mud mix slurry. If the microtextured unfilled elastomer seal performs similarly to the filled elastomer seal, there will be not only irrefutable proof that the proper mechanisms have been identified but also a tremendous opportunity to advanced sealing technology.

Additional microtexture designs could be manufactured and tested both to optimize the design and to apply the strategy to different applications. For example, to combat particles such as those found in the 0-3 μm A.T.D slurry, smaller scale and/or more closely spaced microtextures could easily be designed. An alternative approach would be to mold seals with fibers significantly smaller and/or closer together than

the fibers currently used. Both techniques could easily be tested in the laboratory with seal wear experiments.

Another idea for future work is to conduct simple, fundamental experiments. A simple flat specimen oscillating back and forth linearly or in a circular motion in the presence of an abrasive slurry would be sufficient. It would be informative to see under what conditions particles cluster. Furthermore, this would be an excellent way to study the effect of the fibers on the material removal rate – something the track seal experiments were not able to explain entirely. Material removal could be measured by weighing the specimen before and after testing. In addition, filler fraction, fiber orientation and size, contact pressure, lubrication, and abrasive particle size could all be varied in order to develop a more quantitative understanding of how the fibers alter the abrasive wear process. Similarly, the same experiments could be performed with microtextured specimens. This an essential step in the process of applying what was learned from the track seal to applications beyond oscillating face seals.

Lastly, on the modeling side, it would be worthwhile to model the abrasive wear process in more detail. If one were to model the microcrack initiation, crack propagation, and ridge formation processes described by Fukahori, Barquins, and many others, one might be able to design a filler package that would reduce, not just the aggressive wear and material removal rate of the track seals, but also the wear rate of elastomers in general.

Bibliography

[1] Geethama, V.G., Reethamma, J., and Sabu, T. Short coir fiber-reinforced natural rubber composites: effects of fiber length, orientation, and alkali treatment. *J. Appl. Polym. Sci.*, 55: 583–594, 1995.

[2] Moghe, S.R. Short fiber reinforcement of elastomers (featuring a mathematical model). *Rubber World*, 187: 16–21, 1983.

[3] Murty, V.M., De, S.K., Sivaramakrishanan, R. and Athithan, S.K. Viscoelastic properties of short-fiber-reinforced rubber composites and the role of adhesion. *J. Appl. Polym. Sci.*, 28: 3485–3495, 1983.

[4] Yang, A.C.-M., Ayala, J.E., Bell, Adam and Scott, J.C. Effects of filler particles on abrasive wear of elastomer-based composites. *Wear*, 146: 349–366, 1991.

[5] Ayala, H.M. The effects of soil abrasives on rotary seal effectiveness. Master's thesis, Massachusetts Institute of Technology, Cambridge, MA, 1995.

[6] Ayala, H.M. *Soil Ingestion by Elastomeric Seals.* PhD thesis, Massachusetts Institute of Technology, Cambridge, MA, 1999.

[7] Arruda, E.M. and Boyce, M.C. A three-dimensional constitutive model for the large stretch behavior of rubber elastic materials. *J. Mech. Phys. Solids*, 41, No. 2: 389–412, 1993.

[8] Doonan, T. Finite element analysis of an elastomeric seal. Massachusetts Institute of Technology, 1998.

[9] Derringer, D.C. *Rubber World*, 165: 45–56, 1971.

[10] Yang, A.C.-M., Ayala, J.E. and Scott, J.C. Abrasive wear in filled elastomers. *J. Mater. Sci.*, 26: 5823–5837, 1991.

[11] Hamed, G.R. Molecular aspects of the fatigue and fracture of rubber. *Rubber Chem. Technol.*, 67: 529–536, 1994.

[12] Khan, M.B. and Briscoe, B.J. Simulation of the fracture behavior of elastomeric composites: Mechanical interactions at material interfaces. *Polymer Composites*, 15, No. 1: 83–90, 1994.

[13] Wada, N. and Uchiyama, Y. Friction and wear of short-fibre-reinforced rubber composites under various sliding speeds and loads. *Wear*, 162-164: 930–938, 1993.

[14] Swanson, P.A. Comparison of laboratory abrasion tests and field tests of materials used in tillage equipment. *ASTM Special Technical Publication Proceedings of the Symposium on Tribology*, n 1199: 80–99, December 9, 1992.

[15] Mok, S. and Gorman, D.G. Investigation of factors affecting wear characteristics in rubber-metal sliding contact. *J. Eng. Trib.*, 209: 137–143, 1995.

[16] Muhr, A.H. and Roberts, A.D. Rubber abrasion and wear. *Wear*, 158: 213–228, 1992.

[17] Barquins, M. Friction and wear of rubber-like materials. *Wear*, 160: 1–11, 1993.

[18] Mukhopadhyay, D., Tripathy, D.K., and De, S.K. Wear, tear, and tensile failure of silica-filled ethylene vinyl acetate rubber. *Wear*, 152: 111–125, 1991.

[19] Fukahori, Y. and Yamazaki, H. Mechanism of rubber abrasion, Part I: Abrasion pattern formation in natural rubber vulcanizate. *Wear*, 171: 195–202, 1994.

[20] Fukahori, Y. and Yamazaki, H. Mechanism of rubber abrasion, Part 2: General rule in abrasion pattern formation in rubber-like materials. *Wear*, 178: 109–116, 1994.

[21] Schallamach, A. How does rubber slide? *Wear*, 17: 301–312, 1971.

[22] Gent, A.N. A hypothetical mechanism for rubber abrasion. *Rubber Chem. Technol.*, 62: 750–756, 1988.

[23] Boyce, M.C., Parks, D.M., and Argon, A.S. Large Inelastic Deformation of Glassy Polymers, Part I: Rate dependent constitutive model. *Mechanics of Materials*, 7: 15–33, 1988.

[24] Arruda, E.M. and Boyce, M.C. Evolution of plastic anisotropy in amorphous polymers during finite straining. *International Journal of Plasticity*, 9: 697–720, 1993.

[25] Yeh, O.C. Finite element modeling of a textured seal design for reduced wear. Master's thesis, Massachusetts Institute of Technology, Cambridge, MA, 1997.

[26] Ayala, H.M., Yeh, O.C., Hart, D.P., and Boyce, M.C. Seal design for reduced wear in abrasive slurries. *Wear*, 100: 100–200, 1997.

[27] Zhang, S.W. Wet abrasion of polymers. *Wear*, 62: 1–13, 1992.

[28] Kwon, Y.D., Beringer, C.W., Feldstein, M.A. and Prevorsek, D.O. Fatigue endurance and viscoplastic hysteresis of short fiber/rubber composites. *Rubber World*, 202(2): 29–33, 1990.